Comprehensive Study of the Enhancement of Interplate Coupling in Adjacent Segments after Recent Megathrust Earthquakes

By

Mohammad Yuzariyadi

Supervisor: Prof. Kosuke Heki

A dissertation submitted in partial fulfillment
of the requirements for the degree of
Doctor of Philosophy

Department of Natural History Science
Graduate School of Science, Hokkaido University
February 2021

Abstract

In general, the concept of a seismic cycle, especially in subduction zones, consists of three phases: interseismic, coseismic, and postseismic. These three phases can be observed through surface crustal movement observations with Global Navigation Satellite System (GNSS) because these three phases have different directions of velocities. During the interseismic stage, all GNSS stations on an arc move landward; during the coseismic stage, they jump seaward, and during the postseismic stage, they slowly move seaward and eventually return to the interseismic regime. During the postseismic phase, the deformation caused by the viscoelastic relaxation results in prolonged seaward movement.

Apart from such a classical concept of postseismic seaward movement, several previous studies have also found increased landward surface velocities in the early postseismic stages, especially in segments adjacent along-trench to the megathrust ruptures.

Such cases have been found for the 2003 Tokachi-oki and the 2011 Tohoku-oki earthquakes, NE Japan. A similar increase of landward velocities was reported for the segments to the north of the rupture of the 2010 Maule earthquake, Chile. I utilize available GNSS data to find such changes for six megathrust earthquakes in four subduction zones, including NE Japan, central and northern Chile, Sumatra, and Mexico to investigate their common features. My study showed that such increase, ranging from a few mm/yr to ~1 cm/yr, also appeared in adjacent segments of the 2014 Iquique (Chile), the 2007 Bengkulu (Sumatra), and the 2012 Oaxaca (Mexico) earthquakes in addition to the three previously known cases.

The region of the increased landward movements usually extends with spatial decay

and reach the distance comparable to the along-strike fault length. On the other hand, the temporal decay of the increased velocity is not clear at present. The degree of increase seems to depend on the earthquake magnitude, and possibly scales with the average fault slip in the earthquake. This is consistent with the simple two-dimensional model proposed earlier to attribute the phenomenon to the enhanced coupling caused by accelerated slab subduction. However, these data are not strong enough to rule out other possibilities.

In addition to the information above, I also investigated possible increase in background seismicity following the 2011 Tohoku-oki and the 2010 Maule earthquakes in the regions where GNSS stations showed enhanced coupling. Recent studies suggest that relative plate velocity correlates positively with the seismicity and predict that background seismicity increases where plate convergence accelerates. There, I found a moderate but significant increase in seismicity of ~10%, somewhat smaller than the rates of increased landward velocities.

Acknowledgments

لَا حَوْلَ وَلَا قُوَّةَ إِلَّا بِٱللَّهِ ٱلْعَلِيِّ ٱلْعَظِيمِ

I would like to express my special thanks to my supervisor, Prof Kosuke Heki, who patiently encouraged and guided me. This research topic is new for me, yet while I spent four years working with him, Heki-sensei always answered my question without making me feel inferior.

This study was fully financed by the Indonesia Endowment Fund for Education (LPDP) scholarship. I am grateful for the opportunity they gave me to pursue study at Hokkaido University.

I would also thank Dr. Kei Katsumata, whom I visited several times to discuss the ETAS program and its results.

I also would like to thank Prof. Masato Furuya, Dr. Youichiro Takada, and Prof. Takahashi Hiroaki for their constructive comments.

I'd like to express my gratitude to my family, especially My father and mother, who always send their prayers so that this Ph.D.-journey went well. And of course, for my wife and her patience, many thanks for supporting during my study.

Table of Contents

Chapter 1: Introduction

1.1 Backgrounds

1.1.1 Classical Concept of Seismic Cycle

Earthquakes occur due to the presence of locked plates interfaces, resulting in lithospheric stress and strain. Accumulated compressional and extensional strain that exceeds the elasticity limit of rock is released as fault dislocations, which let seismic waves to radiate from the faults.

Earthquakes that occurred at a certain time often recur after a while. Such cycles continue over thousands of years and are called the “earthquake cycle (seismic cycle)” (e.g. see Broerse, 2012). Records of past earthquake cycles can be found from old documents recording them or through geological observations such as stratigraphic studies of rocks, coral reefs, paleo-tsunami, and paleo-seismology (e.g. Natawidjaja et al., 2006).

Advent of space geodetic techniques such as Global Navigation Satellite System (GNSS) since 1990s established the classical concept of crustal movement in an earthquake cycle. According to this concept, forearc movements at convergent plate boundaries over seismic cycle are characterized by the alternation of slow interseismic landward movement and coseismic trenchward jump. The interseismic movements reflect interplate coupling that accumulates strain toward the next interplate earthquakes. The coseismic jumps correspond to the release of such strain.

Following coseismic jumps, we often observe transient postseismic crustal deformation. Its mechanisms can be divided into 3 types, that is:

1. Poroelastic rebound; deformation that occurs due to fluid moving from a place with high pressure to a place with low pressure driven by compression (e.g. Jónsson et al. 2003).
2. Afterslip; the slow displacement that occurs due to slow continuing slips of the fault (e.g. Heki et al., 1997).
3. Viscoelastic relaxation; relaxation of shear stress coming from viscous flow in the asthenosphere (e.g. Wang et al., 2012).

The three mechanisms differ both in space and time domains. Peltzer et al. (1998) showed that poroelastic deformation occurred over a short period of time, usually within a few months after the main earthquake and/or within small distance from the fault, say 10-20 km. In addition to it, crustal deformation due to afterslip and viscoelastic relaxation occur over a larger spatial and temporal scale. Deformation caused by viscoelastic relaxation mechanism may continue for decades after a megathrust earthquake. A typical example can be found in the postseismic deformations of the 1964 Alaska earthquake (M_w 9.2) lasting more than 30 years (Suito and Freymueller, 2009).

1.1.2 Postseismic Deformation Studies

In the 1980s, Thatcher and Rundle (1984) developed a two-dimensional model to explain the long-term deformations recorded in the Nankai subduction zone, southwest Japan. They concluded that three main stages exist in crustal deformation of every major earthquake; interseismic, coseismic, and postseismic. Research in

later years suggested that the asthenospheric viscosity in subduction zones is in the order of 10^{19} Pa·s, lower than the global average of 10^{20}–10^{21} Pa·s (Wang, 2007). Important findings since the 1980s include:

1. The importance of viscosity of the wedge mantle,
2. Viscoelastic effect consists of short- and long-term components,
3. Existence of afterslips,
4. Magnitude-dependent relaxation times.

Another development is that the previously used viscosity value ~10^{19} Pa·s was updated. The viscosity used to explain satellite gravity observations after the 2004 Sumatra earthquake was 10^{18}–10^{19} Pa·s (Panet et al., 2010; Han et al., 2008).

In the 1980s, postseismic relaxation time constant could not be constrained with sufficient accuracy until the development of Global Positioning System (GPS), the first GNSS developed in America. This technology revolutionized the measurement of crustal deformation. Since the early 1990s, GPS measurements, both campaign and continuous observations, have delineated the typical patterns of coseismic, postseismic, and interseismic crustal deformation in many subduction zones with high precision. These studies showed that deformation in subduction zones changes pattern in an earthquake cycle as suggested earlier by Thatcher and Rundle (1984) and Wang et al. (2012).

From these studies, it can be seen that when a large interplate earthquake occurs, all GNSS stations move trenchward. Over time, part of the GNSS stations continues to move trenchward, and some start to move landward. Ultimately, all GNSS stations move landward as they did before the earthquake (Figure 1.1). We now have a better knowledge on the time evolution of two-dimensional crustal

deformation pattern in a subduction zone over an earthquake cycle. Recent advent of sea floor geodesy revealed postseismic landward motion of the oceanic lithosphere near the Japan Trench after the 2011 Tohoku-oki earthquake (M_w 9.0), which is considered a part of the viscous relaxation (Sun et al., 2014).

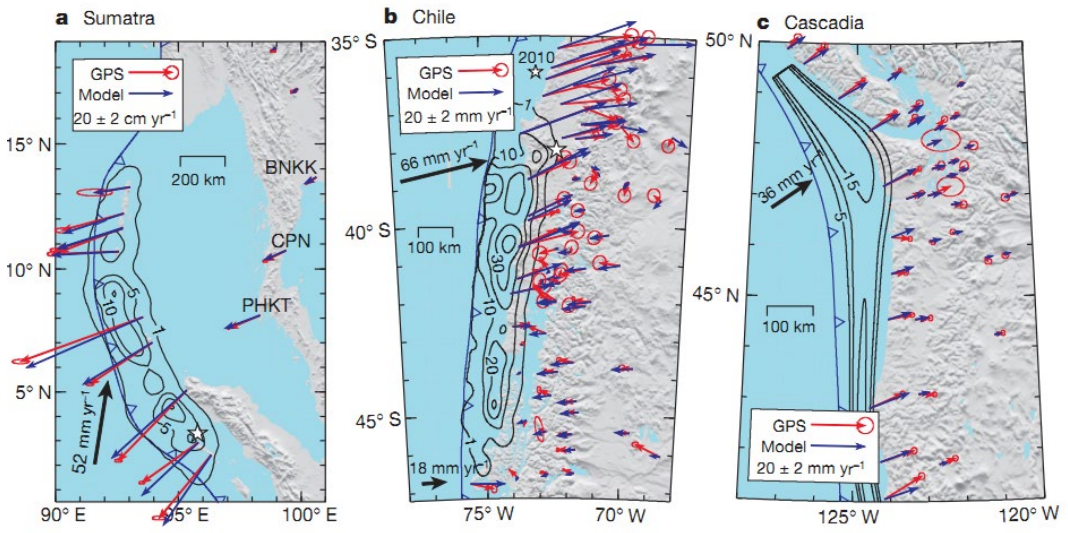

Figure 1.1. Surface velocity vectors in three subduction zones at different stages of the seismic cycle. GNSS velocities are marked in red and predictive models are marked in blue. (a) Velocity vector for postseismic deformation of the 2004 Sumatra-Andaman earthquake, (b) Velocity vector for mixed postseismic and interseismic deformation of the 1960 Valdivia (Chile) earthquake, (c) Interseismic deformation velocity vector ~400 years after the 1600 Cascadia earthquake (Wang, 2012).

1.1.3 Viscoelastic Relaxation

Postseismic stress relaxation realized by viscous flow at the lower crust and/or the upper mantle is one of the mechanisms that gives rise to postseismic deformation. Viscoelastic substances have both elastic and viscous properties. The viscous component makes deformation time dependent. There are several different types of viscoelastic substances, such as Maxwell, Kelvin, and Burgers substances.

Figure 1.2 and Figure 1.3 explain viscoelastic rheology as a combination of springs and dashpots.

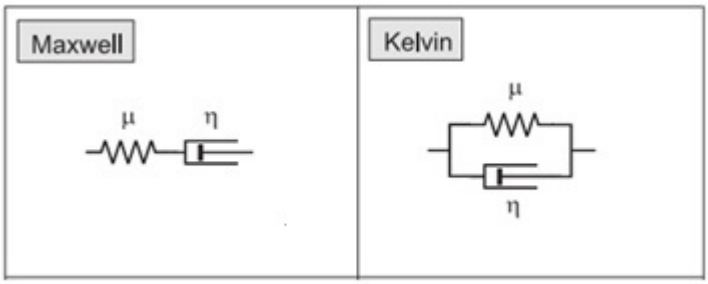

Figure 1.2. Simple mechanical analogy for Maxwell (left) and Kelvin rheology. μ is the shear modulus of the elastic element (spring); η is the viscosity of the viscous element (dashpot) (Ryder, 2006).

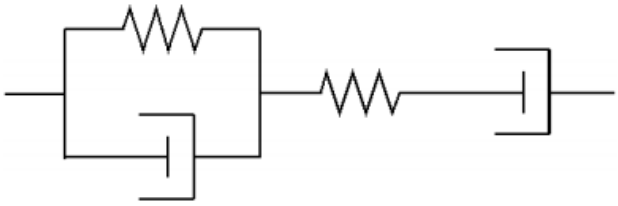

Figure 1.3. Burgers rheology (Gunawan, 2014).

The temporal evolution of the stress is shown in Figure 1.4.

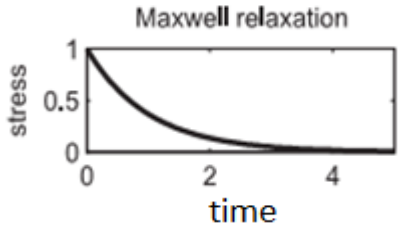

Figure 1.4. Stress relaxation curve for the Maxwell rheology (Ryder, 2006).

Maxwell model of the mantle was first introduced by Nur and Mavko (1970) to model a delayed crustal response to an earthquake (Schubert et al., 2001). The

Maxwell's rheology has been shown to fit various kinds of deformation in subduction zones such as Chile (Moreno et al., 2011; Wang, 2007) and Alaska (Suito and Freymueller, 2009). Pollitz et al. (2006) showed that the Burgers rheology gave better fit to model co- and postseismic crustal deformation of the 2004 Sumatra-Andaman earthquake than the Maxwell model.

1.2 A Brand-New Process in the Earthquake Cycle

Heki and Mitsui (2013) reported unexpected increase of the landward movements of forearc GNSS stations in segments adjacent along-strike to the megathrust rupture after the 2003 Tokachi-oki earthquake (M_w 8.3), and possibly after the 2011 Tohoku-oki earthquake (Figure 1.5).

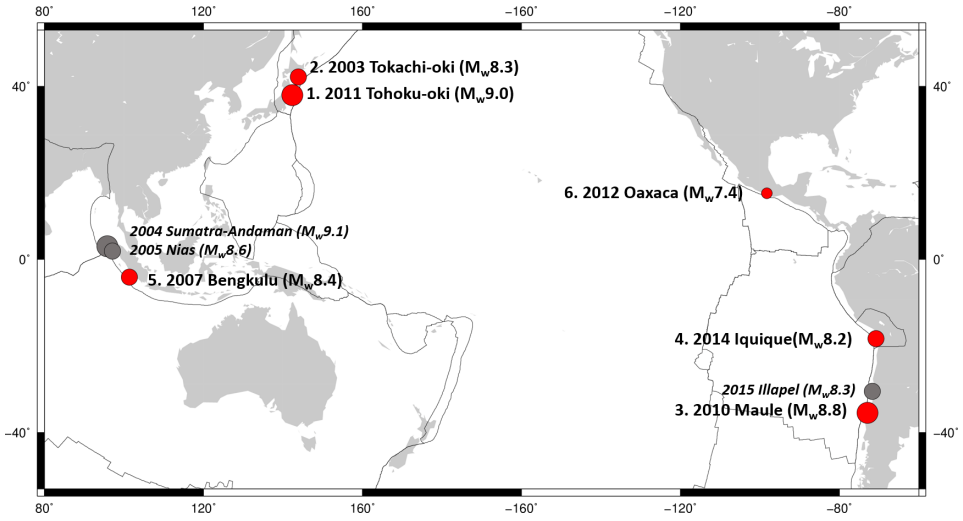

Figure 1.5. The locations of the earthquakes studied here. Red circles represent the six earthquakes that showed postseismic increased landward velocity in segments adjacent to megathrust ruptures. Numbers attached to the earthquakes correspond to those in Table 1. Gray circles represent megathrust earthquakes that may have caused such velocity changes, but I failed to find enough GNSS data from stations in appropriate places with enough time span for pre- and postseismic periods (Section 5.1).

General features of this phenomenon are illustrated in Figure 1.6. After earthquakes, GNSS stations near the ruptured fault would move trenchward due to afterslip and viscous relaxation (Figure 1.6b). In addition to it, Heki and Mitsui (2013) found that stations on segments adjacent to the ruptured fault showed landward increase of movements as illustrated with green arrows in Figure 1.6b. This looks as if interplate coupling in the neighboring segments of the rupture has increased.

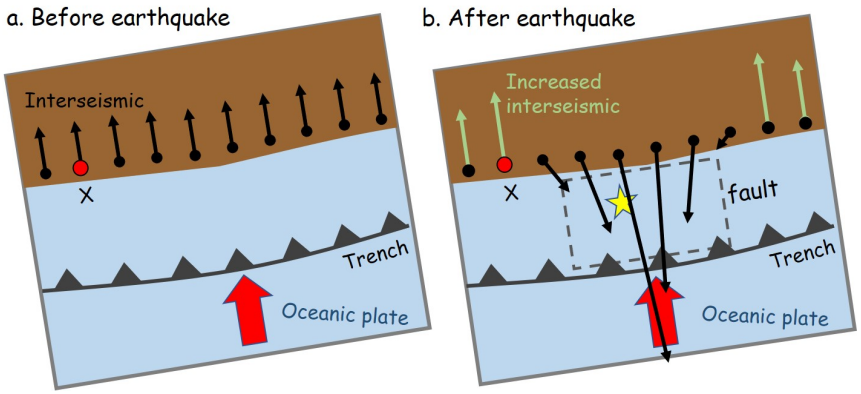

Figure 1.6. Schematic illustration of interseismic movements of GNSS stations (a) and their changes by a large earthquake (b). The trenchward movements in (b) occur driven by afterslip and postseismic relaxation around the ruptured fault. In addition to this, interseismic landward velocities often increase in segments adjacent along-trench to the ruptured segment (station X).

This phenomenon cannot be explained by classical viscoelastic relaxation. Figure 1.7 shows coseismic jump and slow movements caused by postseismic viscous relaxation calculated for a simple thrust earthquake case following Fukahata and Matsu'ura (2005; 2006). Postseismic deformation continues as the shear stress within viscous asthenosphere decays and let the deformation pattern reach the final state realizing the two-dimensional mechanical equilibrium within

150 the lithosphere.

151 Figure 1.7b demonstrates that postseismic viscoelastic relaxation generates
152 only trenchward movement of forearc GNSS stations. In other words, landward
153 increase of velocity as seen for station X in Figure 1.6 does not occur in the adjacent
154 segments. This situation remains similar even with different settings of parameters,
155 e.g. elastic thickness, viscosity of underlying asthenosphere, geometry of the fault.
156 So, the postseismic acceleration of landward velocities as shown in Figure 1.6b
157 would need an explanation with some other mechanisms.

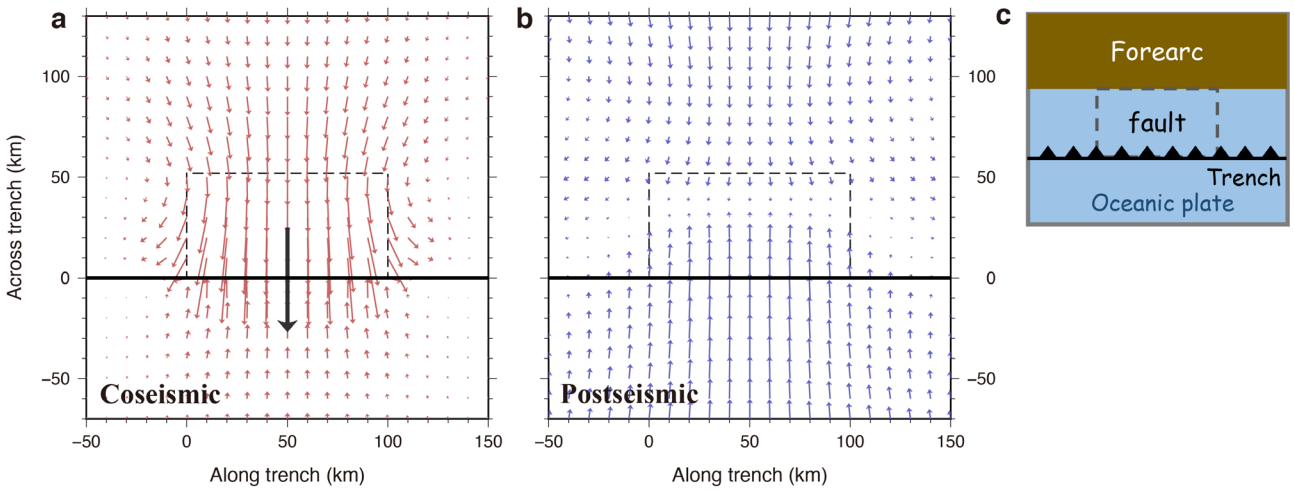

Figure 1.7. Coseismic (a) and postseismic (b) surface displacement by reverse faulting occurring at a fault (dashed rectangle) dipping from the trench (solid line) in a tectonic setting shown in (c), calculated using the software package by Fukahata and Matsu'ura (2005; 2006). I assume a fault 100 × 60 km, with the dip angle 30° and the depth range 0-30 km. I assume lower viscoelastic layer (viscosity 10^{19} Pa·s) beneath the upper elastic layer (thickness 30 km). A thick black arrow in (a) is the surface projection of the coseismic slip vector. (b) indicates the postseismic displacement caused by viscous relaxation of the lower layer after a period 10,000 times as long as the Maxwell time. Here, we can see that the viscoelastic relaxation generates trenchward and landward movements of grid points on land and sea, respectively, but does not make the pattern like Figure 1.6b. The purpose of this figure is just to show patterns of displacements, and scales are not given for the arrows.

Mavrommatis et al. (2014) suggested that the increased coupling in the northernmost Honshu after the 2003 Tokachi-oki earthquake (Segment 3 in Figure 1b of Heki and Mitsui, 2013) reflects the termination of the afterslip of the 1994 M_w 7.6 Sanriku-oki earthquake (Heki et al., 1997). This, however, does not explain the landward velocity increase seen at the neighboring segment on the other side (Segment 1 in Figure 1b of Heki and Mitsui, 2013) of the 2003 Tokachi-oki rupture. Small-scale change of interplate coupling can be explained by the pore fluid pressure changes associated with coseismic fluid migration along the plate interface (Materna et.al., 2019). However, large-scale enhanced coupling that may occur in the adjacent segments cannot be explained by that mechanism.

1.3 Previous works

To explain the postseismic increase of landward velocity in adjacent segments, Heki and Mitsui (2013) hypothesized that the coseismic stress drop modified the force balance acting on the subducting slab around the ruptured segment and induced accelerated subduction of the oceanic plate, a concept similar to the classical idea of Anderson (1975) (Figure 1.4). Uchida et al. (2016) found accelerated interplate creep rates from slip accumulation rates of small repeating earthquakes beneath the Kanto area following the 2011 Tohoku-oki earthquake, which serves as a seismological evidence of the accelerated subduction. Outside NE Japan, Melnick et al. (2017) found the increased landward velocity in central Chile, at GNSS stations located to the north of the 2010 Maule earthquake (M_w 8.8) rupture. Melnick et al. (2017) called it super-interseismic period that occur at the early stage of an earthquake cycle, and Loveless (2017) considered it a common

phenomenon after megathrust earthquakes (Figure 1.9).

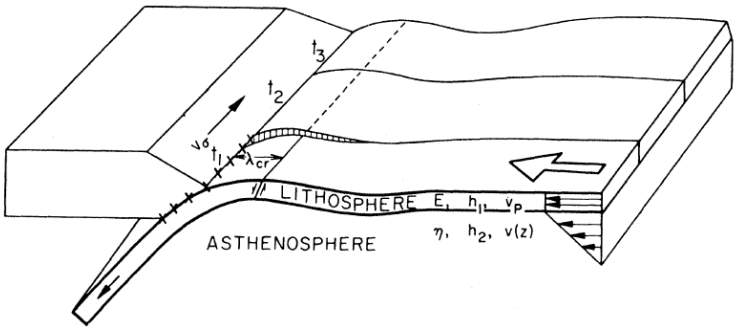

Figure 1.8. Accelerated subduction and enhanced earthquake activity proposed by Anderson (1975). When the decoupling earthquake occurs at time t_1, the stresses of the lithosphere in the segment of t_1 decrease and accelerated subduction starts. This causes the stresses at the segments of t_2 and t_3 of the arc boundary to increase, leading to subsequent earthquakes at times t_2 and t_3.

Melnick et al. (2017) suggested that this enhanced landward velocity might have triggered the 2015 Illapel earthquake (M_w 8.3) and the 2016 Chiloé earthquake (M_w 7.6) that occurred to the north and south of the Maule rupture, respectively. Heki and Mitsui (2013) considered the accelerated slab subduction may explain temporary increase of regional seismicity such as the sequences of megathrust earthquakes in 1950s-1960s in Kamchatka-Aleutian subduction zones (Kanamori, 1978). Indeed, in the Kuril-NE Japan subduction zone, the 2003 Tokachi-oki, the 2004 Kushiro-oki (Mw 7.0), the 2006 central Kuril (Mw 8.3), and the 2011 Tohoku-oki earthquakes occurred within 8 years. Considering the large along-trench extent of these earthquakes, it would be difficult to explain it just by static stress perturbations (King et al., 1994).

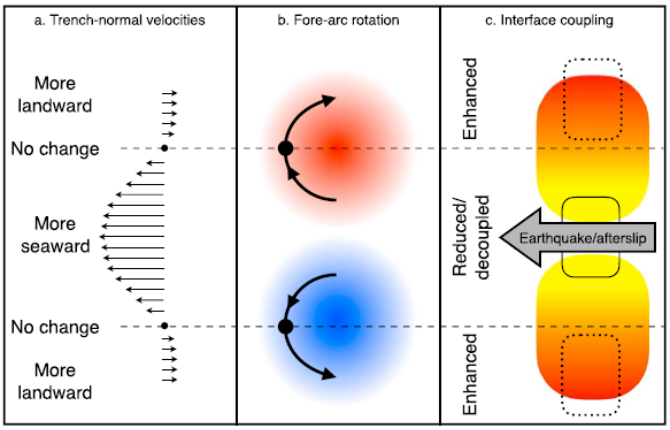

Figure 1.9. Schematic model of postseismic velocity changes according to Loveless (2017). Rotation of the upper plate increases landward velocity adjacent to the rupture zone, consistent with enhanced coupling on the interface beneath these regions. The enhanced coupling may be the site of subsequent earthquakes encouraged by the "super-interseismic" coupling.

The scope of the present study is to explore similar examples worldwide, taking advantage of the rapid expansion of GNSS networks in various subduction zones, using station coordinate data covering periods before and after megathrust earthquakes. I then try to find common features and discuss if the compiled data support a certain model, e.g. the slab acceleration model by Heki and Mitsui (2013).

1.4 Objectives

The purpose of this study is to use the GNSS (Global Navigation Satellite System) measurements to investigate crustal deformation, particularly related to landward increase of surface velocity following six megathrust earthquakes in four subduction zones, including NE Japan, central and northern Chile, Sumatra, and Mexico. I collect as much geodetic information as possible to facilitate the discussion on the model responsible for the postseismic landward change in velocities. I also try to detect increases in seismicity in the segment showing enhanced coupling after the 2011 Tohoku-oki and the 2010 Maule earthquakes.

However, I do not aim at proving particular models including the slab acceleration model by Heki and Mitsui (2013).

1.5 Dissertation outline

This dissertation consists of several Chapters. The brief explanations of the chapters are given below:

Chapter 1 explains the background of this research and the objectives of the research. The last sub-chapter gives the explanation of the outline of this dissertation.

Chapter 2 describes GNSS data in general, those used in individual cases, and time series analysis strategies. Time series analyses are important because the studied cases have different quality and quantity of GNSS data sets. This chapter also describes the method I employed. The first step of the method is to rotate the two horizontal axes (north and east) so that the two components coincide with the direction parallel with or perpendicular to the station's interseismic movement before the earthquakes. Then, trench-normal landward velocity changes are discussed. In this chapter, I also review the slab acceleration model by Heki and Mitsui (2013). Even though the purpose of this study is not to prove the model, their model is important for the exploration of physical mechanisms responsible for the postseismic landward change in velocities.

Chapter 3 describes the landward velocity change that occurred in Japan, Chile, Sumatra-Indonesia, and Mexico. I use the method shown in chapter 4 and give brief description of the tectonic setting of the studied subduction zones. A typical analysis starts with mapping the postseismic crustal movements of the studied earthquake, where one can see distributions of landward and trenchward velocity changes following the earthquake. The stations showing landward velocity changes are selected for further analysis. There, the distances of stations from the fault are considered as an important factor. To present the analysis results, I show the maps and diagrams that show the differences in the velocities following the earthquake relative to the reference velocities before the earthquake.

Chapter 4 contains the overview of the six earthquake cases discussed in the previous chapter. Furthermore, I also discuss the spatial extent of the enhanced coupling, which is closely related to the hypothesis that the enhanced coupling may encourage future failures in the neighboring segments. The next sub-chapter describes the relationship between forearc station velocities and slab velocities. I convert the landward velocity change observed at each station (v'-v) to hypothetical slab acceleration (u'-u). At the end of this chapter, I compare the properties of data with those predicted by the slab acceleration model (Heki and Mitsui, 2013).

In **Chapter 5,** I discuss the change in seismicity following the earthquakes. I expect that the increase of landward velocity is correlated positively with the background

seismicity. To make the analysis more robust, I removed clustered earthquakes such as swarms and aftershocks from the earthquake catalog using a stochastic de-clustering method developed by Ogata (1988).

In **Chapter 6,** I summarize the findings related to the interplate coupling enhancement in adjacent segments following megathrust ruptures.

Chapter 2: Data and Method

2.1 GNSS Data

I analyzed Global Navigation Satellite System (GNSS) data in forearc regions of subduction zones such as the western Sumatra, Northeast Japan, central and northern Chile, and in the Oaxaca region, Mexico.

GNSS is the system that covers the whole earth. The first GNSS is the American system called Global Positioning System (GPS) started full operation in 1990s. Later, three new GNSS have been added, e.g. Russian GNSS called Global Navigation Satellite System (GLONASS), European GNSS called Galileo, Chinese system called Compass/Beidou. There are smaller systems designed as regional satellite positioning systems. They include the Indian Regional Navigation Satellite System (IRNSS), and the Japanese Quasi-Zenith Satellite System (QZSS).

GPS, formally called NAVSTAR GPS (Navigation Satellite Timing and Ranging Global Positioning System), was developed by the Department of Defense of USA in late 1970s and 1980s initially for military purposes. However, it has become a indispensable tool as a versatile geodetic tool for studying various geophysical phenomenon. Over the last three decades, GPS has made a significant impact on a wide range of geophysical disciplines.

By using GPS, Larsen et al. (1992) detected coseismic crustal deformation of the 1987 Superstition Hills earthquake (M_w 6.2), and Lisowski et al. (1990) studied the coseismic deformation of the 1989 Loma Prieta, California, earthquake (M_w 7.1).

These two investigations were among the early utilization of GNSS to understand crustal deformation associated with earthquakes. Then, GNSS can be utilized to understand postseismic deformation behavior as more data recorded year by year. The 1989 Loma Prieta earthquake (M_w 7.1) and the 1992 Landers earthquake (M_w 7.3) were the examples of the first earthquake events whose postseismic signal was well recorded (Savage et al., 1994; Bürgmann et al., 1997; Shen et al., 1994; Savage and Svarc, 1997). The first dense array of GNSS was established in Japan during 1990s. This array first detected coseismic deformation of the 1994 Hokkaido-Toho-Oki earthquake (Tsuji et al., 1995) and postseismic deformation of the 1994 Sanriku-Haruka-Oki earthquake (M_w 7.5) (Heki et al., 1997). After that, they studied crustal deformation related to many earthquakes with magnitudes exceeding 6 in and around Japan (Sagiya, 2004).

The recent advance of space geodetic technology revealed new kinds of crustal deformation related to earthquakes. Sato et al. (2011) detected coseismic sea floor movement associated with the 2011 Tohoku-oki earthquake (M_w 9.0). This was followed by Sun et al. (2014), which revealed the postseismic landward motion of the oceanic lithosphere near the Japan Trench. Heki and Mitsui (2013) found a increase of the landward movements of GNSS stations in segments adjacent along-strike to the megathrust rupture, the 2003 Tokachi-oki earthquake (M_w 8.3) and the 2011 Tohoku-oki earthquake.

Below I give brief descriptions of the GNSS data used in this study. Nowadays, the movements of GNSS stations are described within the International Terrestrial Reference Frame (ITRF). These velocities align with the no-net-rotation plate motion models and were converted to those relative to the landward plate by subtracting velocities calculated using the nnr-MORVEL56 model (Argus et al.,

2011). Because I discuss changes in velocity before and after large earthquakes, common bias to these velocities is canceled. This means that results in the present study are not so sensitive to the selection of the plate motion model.

2.1.1 GNSS Data in Japan

In Japan, we used the F3 solution of the dense continuous GNSS array called GNSS Earth Observation Network System (GEONET). This network is composed of more than 1,300 stations with an average separation of ~20 km and covers the whole Japanese archipelago (Figure 2.1). It is operated by the Geospatial Information Authority (formerly Geographical Survey Institute) (GSI), Japan, and the data are made open to worldwide geodetic communities. The F3 solution is obtained by using the Bernese software fixing a certain station in Tsukuba, near the GSI headquarter, to the coordinates determined daily using stations in the Asia Pacific region (Nakagawa et al., 2009).

For the 2003 earthquake, I followed the procedure by Heki and Mitsui (2013) and fixed the Kamitsushima station, north of Kyushu, and compared the velocity difference before and after the earthquake. For the 2011 earthquake, the Kamitsushima station, ~1,000 km away from the epicenter, exhibited a few mm/yr postseismic movements. Hence, I did not fix any stations and subtracted the movement of the landward plate calculated with the nnr-MORVEL56 plate motion model (Argus et al., 2011) from the coordinate changes in the F3 solution expressed in ITRF.

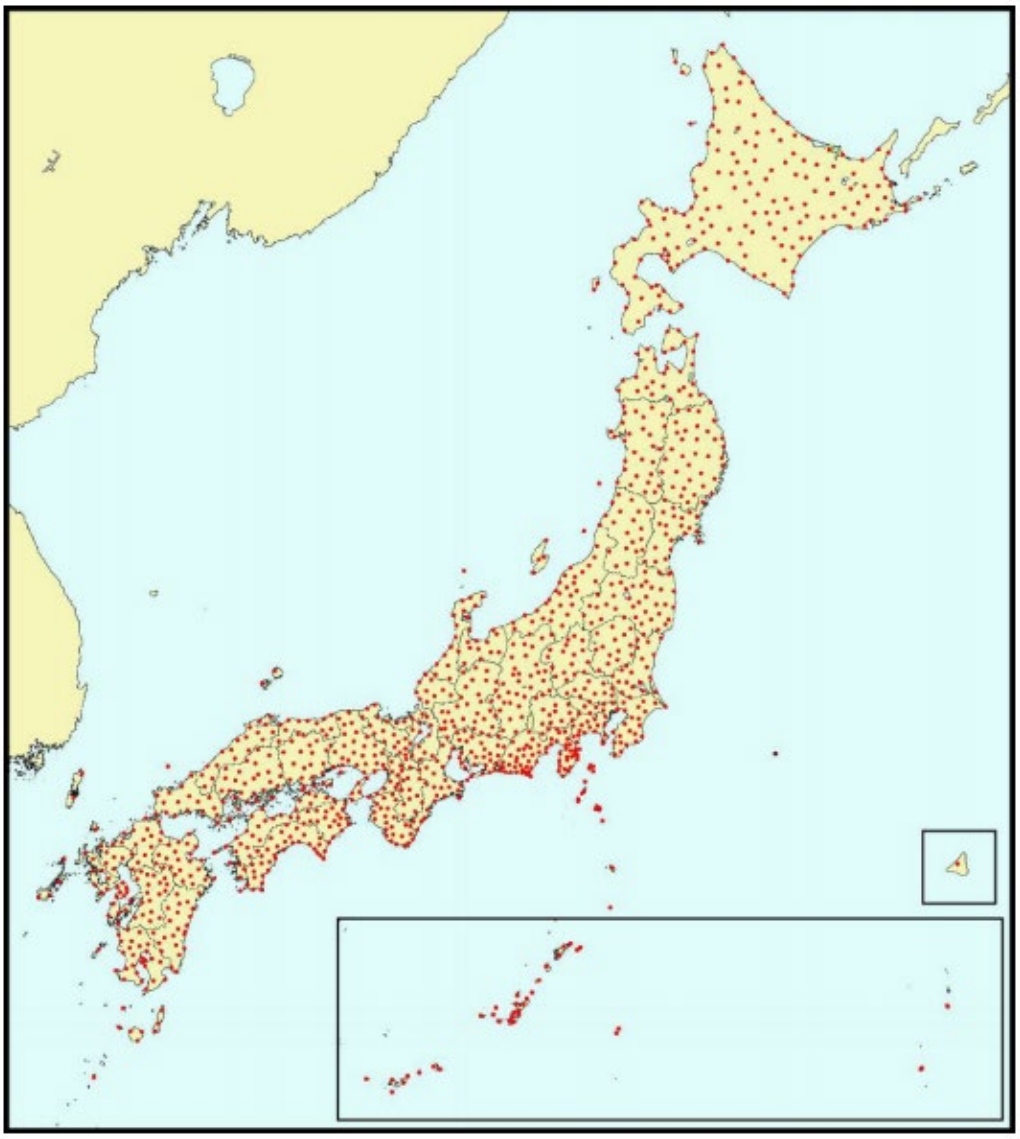

Figure 2.1. Distribution of GEONET stations (https://www.un-ggim-ap.org/meetings/ pm/5th/201607/W020161027635538377589.pdf)

2.1.2 GNSS Data in Sumatra

In Sumatra, there are several GNSS network systems operated by different institutions. The Geospatial Agency of Indonesia (BIG) initiated geodetic networks for geodynamics studies in Sumatra in 1989 (Abidin et al., 2016). A total of 60 GNSS stations on Sumatra and surrounding islands, installed in 1989, 1991, and 1993, were used to detect crustal movements in the Sumatran subduction zone (Prawirodirjo et al., 1997). In 2002, Caltech (California Institute of Technology)

initiated the Sumatran GPS Array (SuGAr), a continuous GNSS network composed of 60 stations designed to monitor tectonic processes along the Sumatra subduction zone. SuGAr stations are mostly installed on the Sumatran forearc islands and west coast of Sumatra. After over a decade of collecting data, SuGAr has detected coseismic jumps and slow postseismic deformation for several large earthquakes (Feng et al., 2015). Figure 2.2 shows the distribution of GNSS stations in Sumatra, Indonesia.

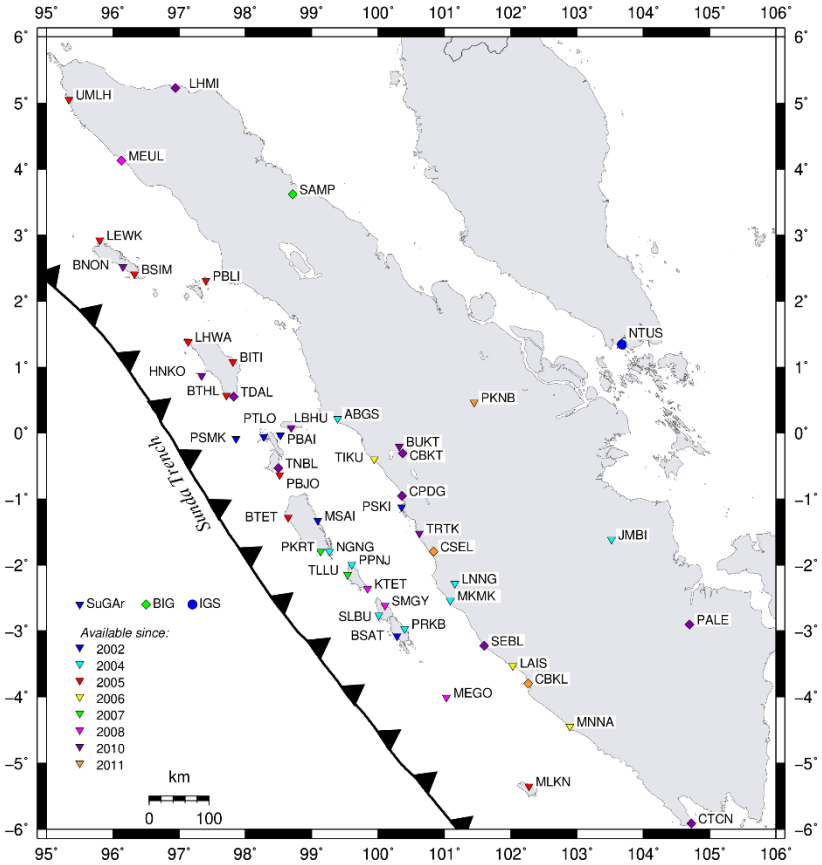

Figure 2.2. GNSS stations that are available in Sumatra and surrounding regions. Colors indicate observation start years.

For the 2007 Bengkulu earthquake (M_w 8.4) case, I analyzed the solutions from SuGAr network provided by Bandung Institute of Technology (Ardika et al., 2015). The data had been processed using the GAMIT 10.5 software package to obtain

daily solutions (Herring et al., 2018). Figure 2.3 shows GNSS data availability near the 2007 Bengkulu earthquake, whose locations are shown in Figure 2.4. For the purpose of the current study, we need stations with long time spans before and after the earthquake. At the same time, the stations should not be too close to the epicenter to avoid the influence of afterslip and viscoelastic relaxation. For the 2007 Bengkulu earthquake, only MLKN satisfies the conditions (shown in green bars in Figure 2.4).

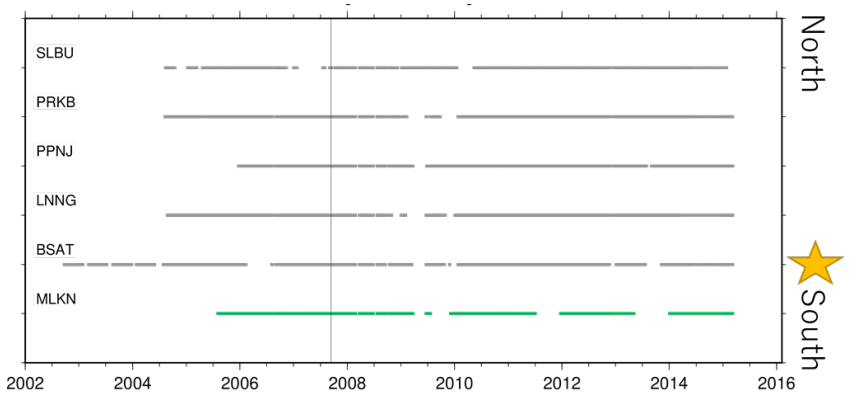

Figure 2.3. Data availability at GNSS station near the 2007 Bengkulu earthquake (M_w 8.4) epicenter. The vertical line denotes the 2007 earthquake. Source: Ardika, et al. (2015). The data from MLKN (shown in green) are used in this study to study postseismic enhanced landward velocity.

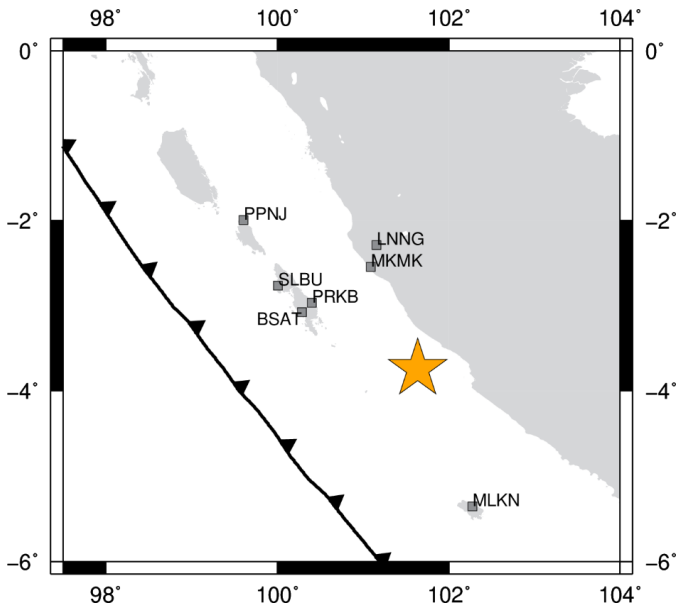

Figure 2.4. Location of GNSS stations near the 2007 Bengkulu earthquake (M_w 8.4) epicenter. Star indicates the location of largest coseismic slip of the earthquake.

2.1.3 GNSS Data in South and Middle America

For the South and Middle American GNSS data, I analyzed the Precise Point Positioning (PPP) solutions available from the Nevada Geodetic Laboratory, University of Nevada, Reno (Blewitt et al., 2018; Figure 2.5) and partly from Jet Propulsion Laboratory at sideshow.jpl.nasa.gov/post/series.html. Data availability at every GNSS station near the earthquake's location can be seen in Figure 2.6, 2.7, 2.8, 2.9, 2.10, and 2.11.

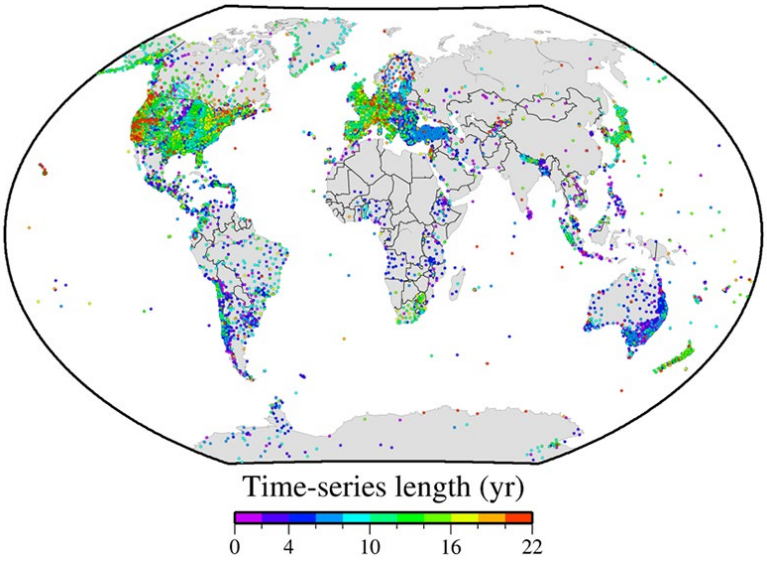

Figure 2.5. Processed data from 17,000 GNSS stations available in the Nevada Geodetic Laboratory website (source: https://eos.org/science-updates/harnessing-the-gps-data-explosion-for-interdisciplinary-science). Colors indicate the time-series lengths.

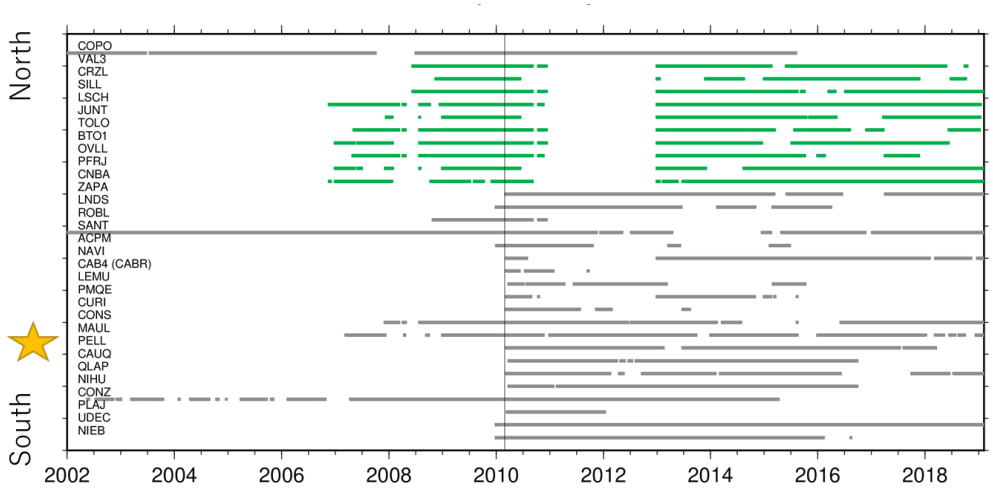

Figure 2.6. Data availability of GNSS stations near the 2010 Maule earthquake (Mw 8.8) epicenter. The vertical line denotes the 2010 earthquake. Source: geodesy.unr.edu, accessed on 2020/04/10. Stations with long time series before the earthquake (shown in green), suitable for this study, are limited to the north of the epicenter.

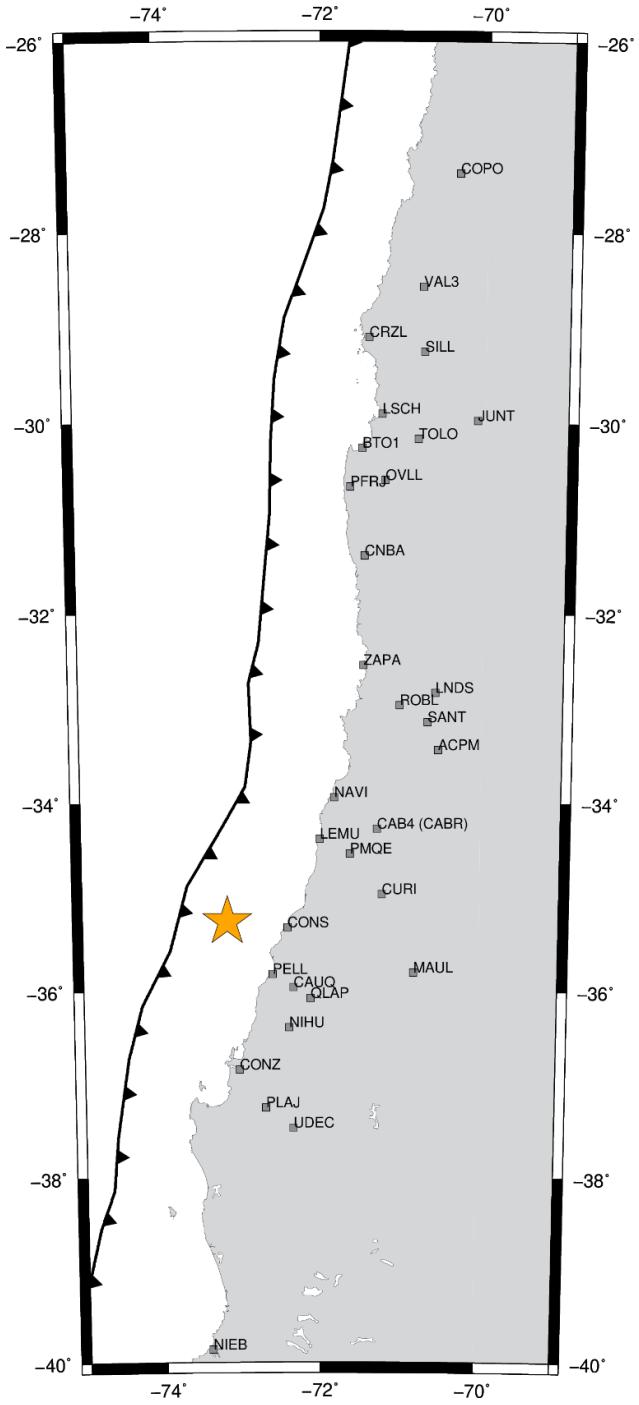

433

434 **Figure 2.7.** Location of GNSS stations near the 2010 Maule earthquake (M_w
435 8.8) epicenter shown in Figure 2.6. Star indicates the location of largest
436 coseismic slip of this earthquake.

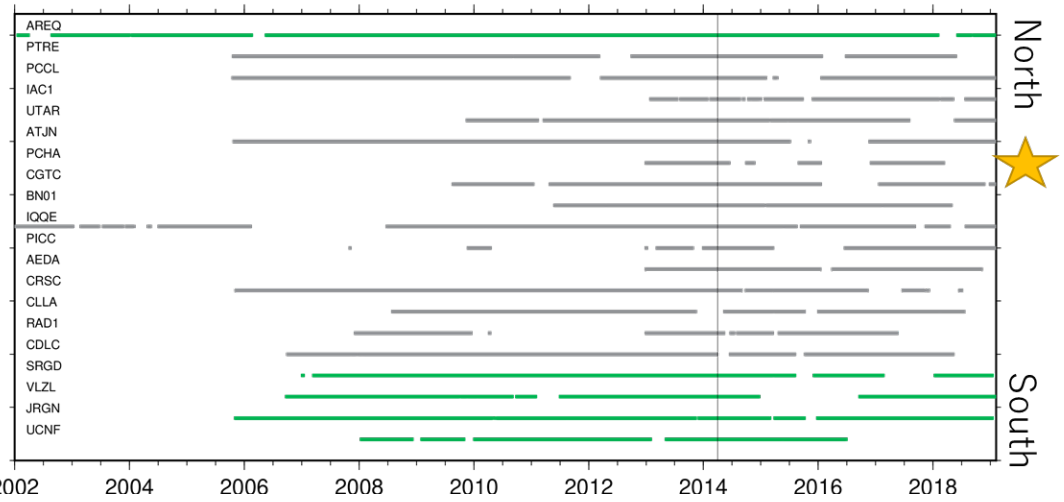

Figure 2.8. Data availability of GNSS stations in northern Chile and Peru for the study of the 2014 Iquique earthquake. The vertical line denotes the 2014 earthquake. Source: geodesy.unr.edu and sideshow.jpl.nasa.gov/post/series (for AREQ station). Accessed on 2020/04/10.

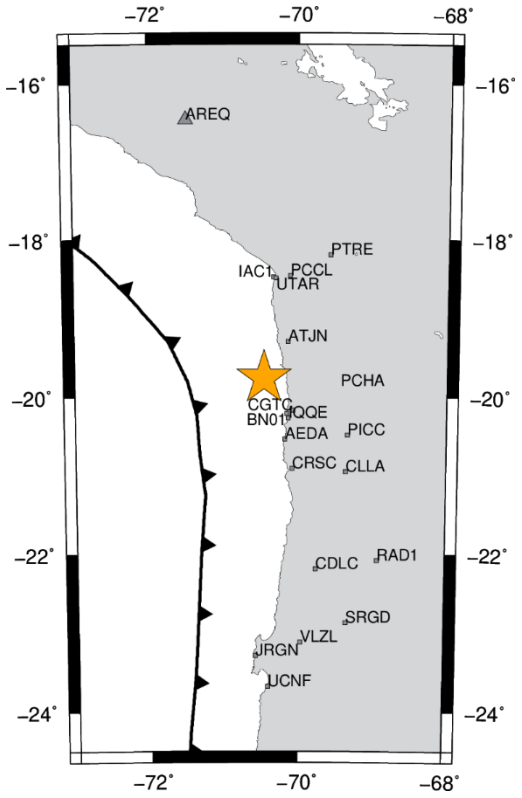

Figure 2.9. Location of GNSS stations near the 2014 Iquique earthquake (M_w 8.2) epicenter shown in Figure 2.8. Star indicates the location of largest coseismic slip of the earthquake.

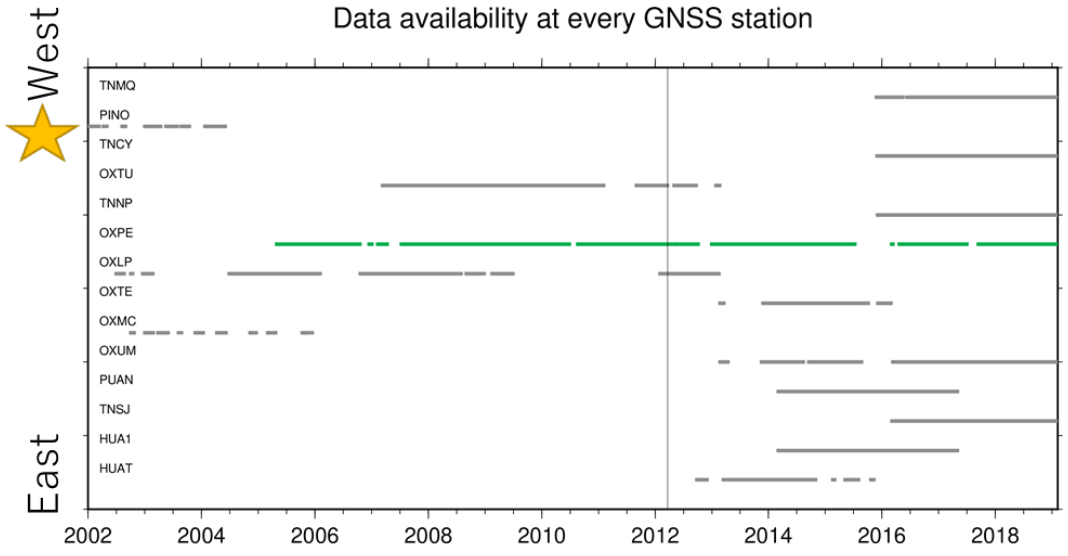

Figure 2.10. Data availability at GNSS station near the 2012 Oaxaca earthquake (M_w 7.4) epicenter. The vertical line denotes the 2012 earthquake. Only one station (OXPE, shown in green) was suitable for the purpose of this study. Source: geodesy.unr.edu. Accessed on 2020/04/10.

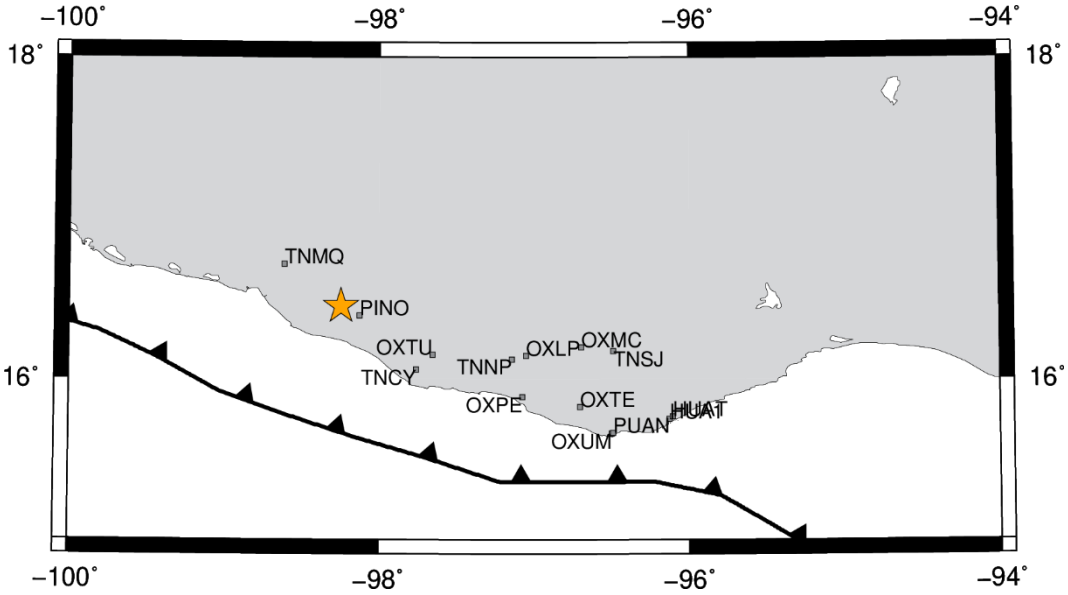

Figure 2.11. Location of GNSS stations near the 2012 Oaxaca earthquake (M_w 7.4) epicenter. Star indicates the location of largest coseismic slip of the earthquake.

2.1.4 Time series analysis strategy

The target of this study is the "landward" velocity changes in the forearc region

461 of the segment adjacent along-trench to the megathrust ruptures. Therefore, I have
462 to avoid GNSS stations suffering from postseismic “trenchward” movements. They
463 are caused by well-known mechanisms such as afterslip and viscous relaxation of
464 asthenosphere. Such movements have already been well documented in literatures
465 for individual earthquakes, such as Yamagiwa et al. (2015) for the 2011 Tohoku-oki
466 earthquake, Miyazaki et al. (2004) for the 2003 Tokachi-oki earthquake, Klein et al.
467 (2016) for the 2010 Maule earthquake, Hoffmann et al. (2018) for the 2014 Iquique
468 earthquake, and Lubis et al. (2012) for the 2007 Bengkulu earthquake.

469 To select stations showing landward velocity changes, I checked not only the
470 polarities of trench-normal velocities but also the distance of stations from the fault
471 edge. This is because the enhanced inter-plate coupling studied here tend to occur
472 in a certain range of distance, i.e. they occur in forearc from the fault edge over a
473 distance comparable to a half of the fault length. This will be discussed later in
474 Chapter 4.2.

475 In calculating the velocity changes of the selected GNSS stations, I compare
476 velocities during the two periods before and after the earthquakes (Table 1). These
477 periods should be long enough to enable estimation of accurate velocities (longer
478 than two years to robustly remove seasonal changes) and hopefully be immediately
479 before and after earthquakes. Actually, I often have to shift or shorten these periods
480 to avoid unwanted transient movements caused by other smaller earthquakes during
481 the studied periods.

482 It should be noted that landward velocity changes depend on the selection of
483 time windows. For example, such velocity changes are often unstable during the
484 first few years while postseismic transient movements continue. I will discuss this
485 problem comparing velocities in different time windows in Chapter 4.3.

I also need to pay attention to past earthquakes in nearby segments. Large interplate earthquakes are followed by trenchward postseismic movements of GNSS stations lasting for years. Their temporal decay might leak into the postseismic landward velocity increases, the target of the present study. For the six earthquakes studied here, I discuss potential influences from such past earthquakes in Chapter 3.

493 Table 1. Two periods used to estimate velocity changes before and after the earthquakes (Figure 1).

No.	Earthquake (M_w)	Before earthquake	After earthquake[3]
1	2011/3/11 Tohoku-oki (9.0)	2008.00-2011.19	2011.19-2015.00
2	2003/9/25 Tokachi-oki (8.3)	1996.00-2003.74[1]	2003.74-2010.10
3	2010/2/28 Maule (8.8)	~2008.00[2]-2010.16	2010.16-2014.70
4	2014/4/1 Iquique (8.2)	~2010.00[2]-2014.25	2014.25-2019.25
5	2007/9/12 Bengkulu (8.4)	2005.50-2007.70	2007.70-2010.81[4]
6	2012/3/20 Oaxaca (7.4)	2010.38-2012.22	2012.22-2017.22

[1]Shifted to 1996.0-2003.0 to avoid influence of the Miyagi-oki earthquake (M_w 7.0) on 2003 May 26 for stations close to its epicenter
[2]Earliest possible starting times are used depending on the availability of the stations
[3]The early non-linear postseismic periods avoided to draw Figures 6a, 7a, and 8a.
[4]Only data until the occurrence of the 2010 Mentawai earthquake are used.

494

2.2 Method for acceleration analysis

I model the time series of the two horizontal components of a GNSS station coordinate considering linear trends, average seasonal (annual and semiannual) changes, jumps associated with antenna replacements (for GEONET stations), and coseismic jumps. In addition to these standard parameters, I estimate the coseismic changes in velocity (v'-v). The velocities are expressed relative to the stable part of the landward plates of the subduction zones (Figure 2.12). I also discuss possible existence of non-linear movements shortly after earthquakes and their influences later in Chapter 4.3.

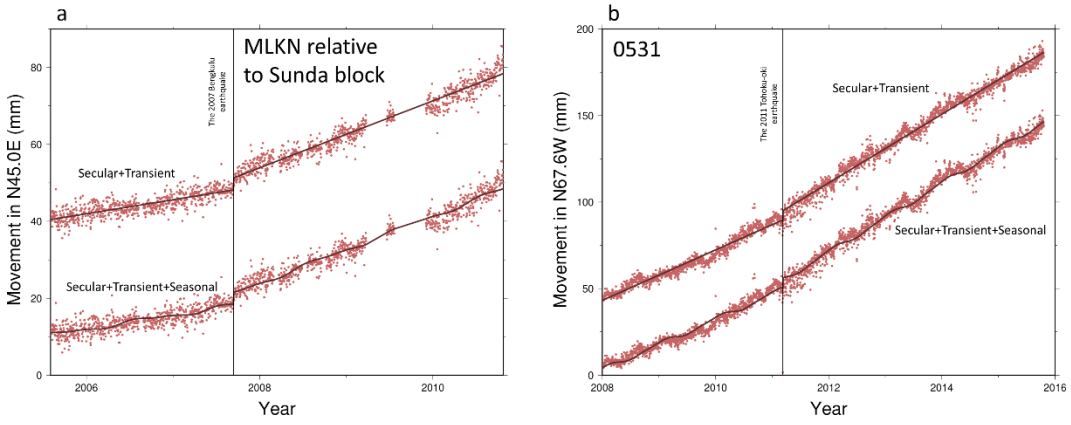

Figure 2.12. Landward movement time series of the stations MLKN (Bengkulu, Indonesia) and 0531 (Hokkaido, Japan). Both two time series are modeled considering linear trends (including changes in trends associated with earthquakes), jumps caused by antenna replacements (for GEONET stations), and average seasonal changes. The average seasonal components are removed in the upper time series.

In Chapter 3, I show a set of figures as shown in Figure 2.13, for each megathrust earthquake. I first rotate the two horizontal axes (north and east) so that the two components coincide with the direction parallel with (red in Figure 2.13a) or perpendicular to (blue in Figure 2.13a) the interseismic movement of the station before the earthquakes (normally in the direction of the subducting oceanic plate). In the plot, I subtract the estimated average seasonal components.

In the diagram, the coseismic increase of the landward velocity of a GNSS station appears as the positive change in the slope of the red time series (Figure 2.13a). The blue (trench-parallel) component represents the change in the direction of the movement by the earthquakes. This is expected to be small. Both components often show coseismic jumps, but they are not the target of the present study.

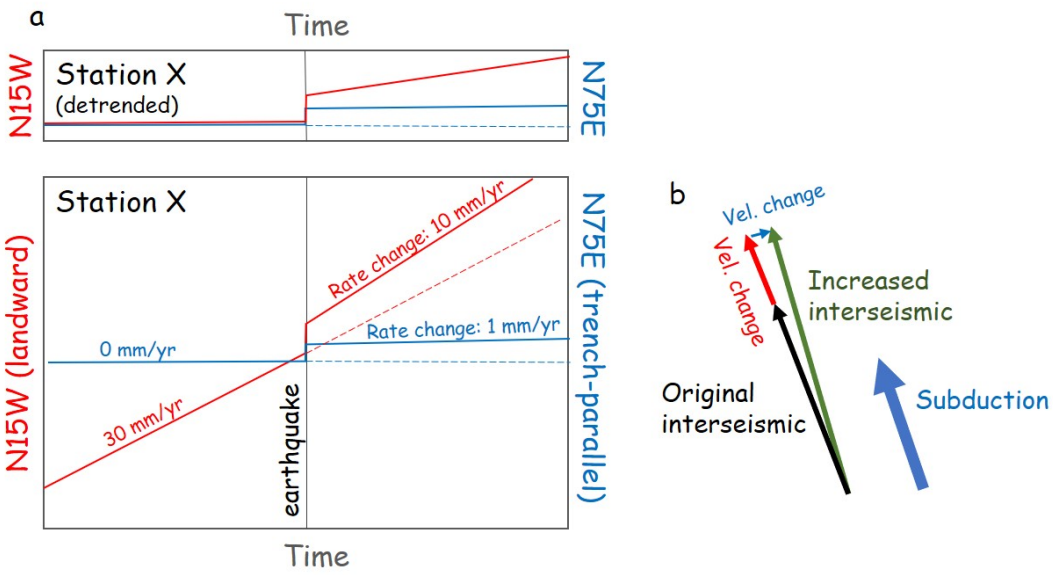

Figure 2.13. An example of the analysis of the velocity change after a large earthquake for the station X shown in Figure 1.6. (a) I rotate the horizontal axes so that one axis coincides with the interseismic movement direction (red) and the other axis is perpendicular to it (blue). Thus, the increase of the landward velocity of a GNSS station can be seen as the increased slope of the red component. In the small panel atop, I remove the pre-earthquake linear trend (dotted line) to isolate postseismic changes in trend. Y-axis represents the movement in the trench-normal (landward) and trench-parallel azimuths. (b) Concept of the increased interseismic velocity which is the sum of the interseismic velocity before the earthquake and the coseismic velocity change.

Here, I do not discuss vertical components. In fact, changes in vertical velocities were not significant for the 2003 case as reported in Heki and Mitsui (2013). This partly comes from intrinsic large uncertainty in determining the vertical positions. Figure 2.14 shows that vertical velocities changes following the 2011 Tohoku-oki

earthquake are insignificant and non-systematic in direction. The figure also shows the vertical coordinate time series of two Chilean stations before and after the 2010 Maule earthquake. These figures suggest it difficult to extract meaningful changes in vertical velocities by this earthquake.

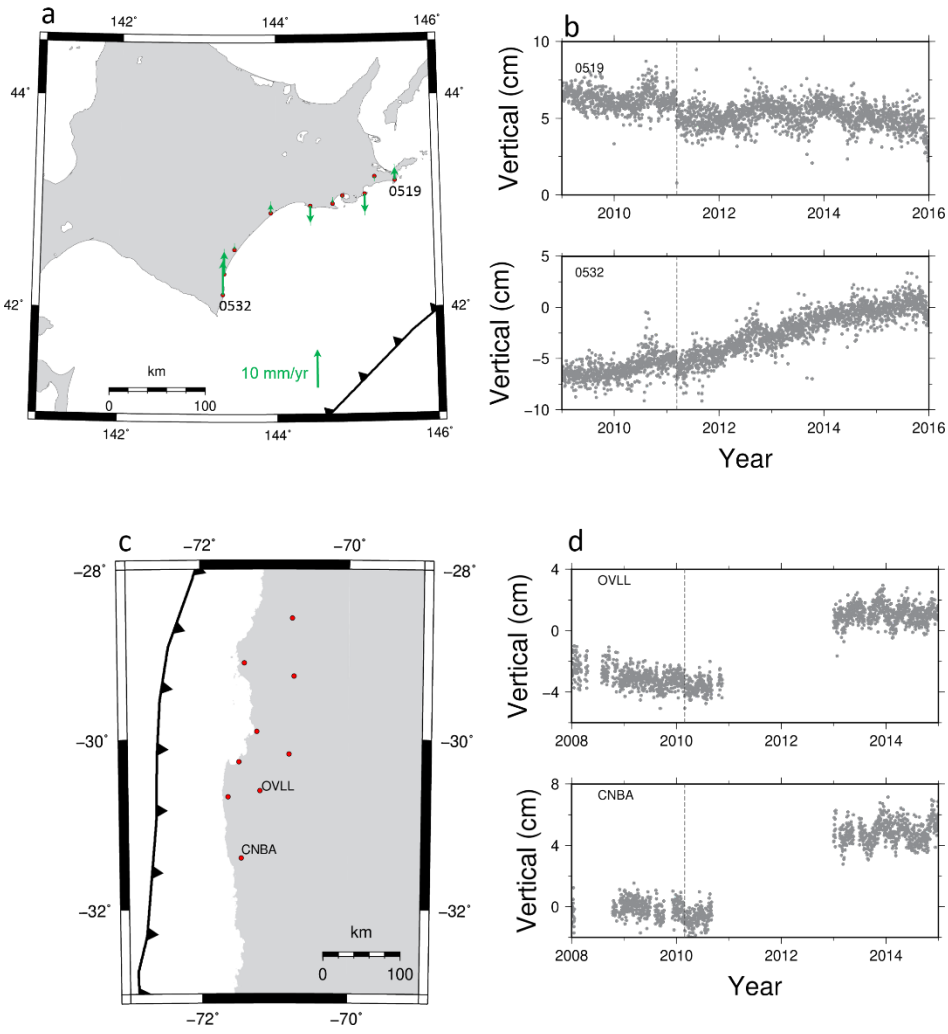

Figure 2.14. (a) Vertical velocity changes of GNSS stations in Hokkaido associated with the 2011 Tohoku-oki earthquake. I selected the same periods as in Figure 3.3. (b) Time series of the vertical position of the stations 0519 and 0532, shown in (a). (c) I selected two Chilean stations, and (d) plot their vertical position time series before and after the 2010 Maule earthquake.

To see the whole picture of the postseismic increase of interplate coupling, we need multiple stations deployed at various distances from the megathrust fault. Typically, postseismic trenchward velocities dominate near the fault. Then,

554 landward increased velocities (enhanced coupling signature) emerge as we go away
555 along trench from the fault (Figure 1.6b). This enhanced coupling would then decay
556 as we go farther away from the fault.

557 It is usually difficult to see them all due to the insufficient availability of GNSS
558 stations along the forearc. In this study, I use multiple stations to represent the
559 landward velocity change whenever possible. Nevertheless, I sometimes have to let
560 just one station represent the increase of the landward velocity for certain
561 earthquakes. In the discussion, I compile all the cases to extract common features
562 so that I can discuss the physical model behind the phenomenon.

563 For very large earthquakes, postseismic velocity changes can occur in a
564 continental scale as shown in Melnick et al. (2017) in South America following the
565 2010 Maule earthquake. It is also likely that a similar situation occurred following
566 the 2011 Tohoku-oki earthquake as seen in GNSS point velocities in China (Shao
567 et al., 2015). In this study, I focus on the velocity changes occurring near the
568 ruptured faults.

569

570 2.3 Slab acceleration model by Heki and Mitsui (2013)

571 The purpose of this study is to collect as much geodetic information as possible
572 to facilitate the discussion on the model responsible for the postseismic landward
573 change in velocities. I do not aim at proving a particular model, including the model
574 by Heki and Mitsui (2013). In fact, there are attempts to explain postseismic
575 landward velocity changes within the framework of viscous relaxation. For example,
576 Melnick et al. (2017) reports results by a three-dimensional thermomechanical
577 model to reproduce continental scale postseismic velocity changes. D'Acquisto et
578 al. (2020) try to explain the observed changes as the elastic bending in a horizontal

plane in response to the postseismic trenchward movement near the rupture area. Other models capable of explaining the observations may also emerge in future. Here, as one of the possibilities, I review the simple slab acceleration model Heki and Mitsui (2013) proposed to explain the landward increased movements in segments adjacent along-strike to a megathrust rupture.

Figure 2.15a indicates the balance of forces acting on a subducting slab during an interseismic period. There, two down-dip forces, slab pull *Fsp* and ridge push *Frp*, are balanced with the two up-dip forces, side (partially bottom) resistance *Fsr* exerted by the surrounding asthenosphere and interplate coupling *Fc* at the plate interface. *Fsr* is proportional to the subduction speed *u* and I assume the resistance occurs in a thin low-viscosity layer at the slab surface. This is a two-dimensional model and the forces represent those working on a thin slice with a unit thickness.

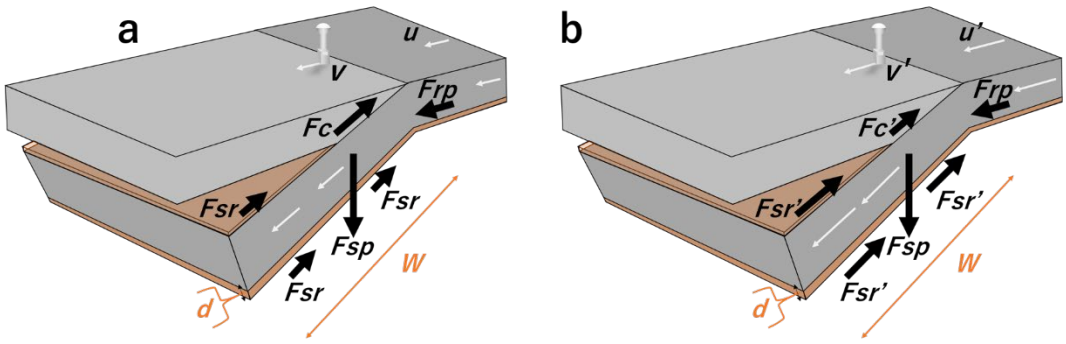

Figure 2.15. Schematic view of the slab acceleration model, redrawn after Heki and Mitsui (2013). (a) and (b) show forces acting on a subducting slab before and after a megathrust earthquake, respectively, with a large stress drop. In (a), downward forces (*Fsp*: slab pull, *Frp*: ridge push) are balanced by upward forces (*Fc*: interplate coupling, *Fsr*: side resistance). In (b), sudden decrease of the coupling *Fc* to *Fc'* is compensated by the increase of *Fsr* to *Fsr'* realized by the slab acceleration from *u* to *u'*. The velocity of GNSS station before and after the earthquake is indicated by *v* and *v'*. *W* is the total trench-normal length of slab surface (both upper and lower surfaces) where viscous braking works, and *d* is the thickness of the thin low viscosity layer at the lithosphere-asthenosphere boundary.

605

606 Occurrence of a megathrust would reduce the coupling from *Fc* to *Fc*', which
607 would be compensated by the increase of the side resistance caused by the
608 acceleration of the subduction speed from *u* to *u*'. Let *Fc-Fc'* be the lost coupling
609 (stress drop integrated along-dip), and it can be related to the slab acceleration *u'-u*
610 as follows.

611

612 $$Fc\text{-}Fc' = Fsr' - Fsr = (u' - u)\,\mu W/d \quad (1)$$

613

614 where μ is the viscosity of the low-viscosity layer with the thickness of *d*, and *W* is
615 the along-dip slab length (both upper and lower surface) where viscous braking
616 works. Then, the acceleration *u'-u* is expressed as

617

618 $$u' - u = (Fc\text{-}Fc')\,d/\mu W \quad (2)$$

619

620 For the same subduction zone with uniform μ, *W* and *d*, the acceleration *u'-u* would
621 be proportional to *Fc-Fc*'. Larger earthquakes would accelerate the slab more
622 strongly with a larger *Fc-Fc'*. It is actually the product of the fault width (along-dip
623 length) *D* and the stress drop $\Delta\sigma$.

624

625 $$Fc - Fc' = \Delta\sigma D \quad (3)$$

626

627 Using the average slip s_{av}, $\Delta\sigma$ can be expressed using the rigidity ν as

628

629 $$\Delta\sigma = \nu s_{av}/D. \quad (4)$$

For the same subduction zone, I assume ν is the same. Then equations (3) and (4) suggest that *Fc*-*Fc*', and hence $u' - u$, scales with the average slip s_{av}, i.e.,

$$u' - u = (d\nu/\mu W)\, s_{av}. \quad (5a)$$

In the present study, I compare cases in different subduction zones. It is generally difficult to infer diversity of parameters ν, d, and μ for different subduction zones. However, we can know W from seismological studies. In other words, by assuming that $\nu d/\mu$ is the same, it may become possible to examine if the observed slab acceleration u'-u is proportional to s_{av}/W,

$$u' - u = (\nu d/\mu)\, s_{av}/W. \quad (5b)$$

In Chapter 4.5, I examine if the observed velocity changes for different megathrust earthquakes in various subduction zones obey equations (5a) and (5b).

2.4 Subduction zones and slab data interpretation

According to the classical continental drift concept, the earth's surface consists of several fragments of the continent that move relatively to each other over a geologic timescale. The establishment of plate tectonic theory evolved from this fundamental concept. Then, we came to recognize the mantle convection and the formation of oceanic lithosphere along mid-oceanic ridges due to seafloor spreading. According to the plate tectonic theory, oceanic lithosphere continuously

subducts into depth along convergent plate boundaries.

Subduction is the descend of a cold oceanic plate beneath a continental plate. The slab of the oceanic lithosphere sinking into the asthenosphere provides most of the force required to move the plates and cause the ocean floor spreading along mid-oceanic ridges. Subduction is also responsible for bringing the surface material such as oceanic crust, deep-sea sediments, and seawater into the depth, and their interaction with surrounding mantle causes magma generation, arc volcanism, and formation of continental crust.

The lengths of the subducting slabs beneath continental plates often reach several hundreds of kilometers from the trench. Subduction zones are composed of island arcs and deep-sea trenches and act as convergent plate boundaries. There are two distinct subduction behaviors based on the age and type of subducting lithosphere (Uyeda, 1982). Subduction zones with relatively steep dip angles of the subduction are usually associated with the subduction of older oceanic lithosphere (the Mariana type). Conversely, relatively shallow angles tend to occur where younger oceanic plates subduct (the Chilean type). This difference controls the seismic coupling in subduction zones. The subduction zones with denser and older lithosphere tend to show weaker seismic coupling. On the other side, stronger seismic coupling often occurs where young oceanic lithosphere subducts. Very large interplate earthquakes are more common in the second type of subduction zones.

The difference of strain regime in the magmatic arc also reflects the type of subduction zones. The steeper dip of the older lithosphere slab allows the flow of the asthenosphere in the mantle wedge. Consequently, back-arc extensions with

678 rifting or even seafloor spreading are often found in the Mariana type subduction
679 zones. In contrast, compression with folding and thrusting behind the arc is
680 common in the Chilean type subduction zones. Such compression stems from the
681 frictional resistance by the subduction of young buoyant lithosphere. The difference
682 of the age is largely responsible for the classification into the Mariana type (>100
683 million-year-old) and the Chilean type (<50 million-year-old) subduction zones
684 (Figure 2.17).

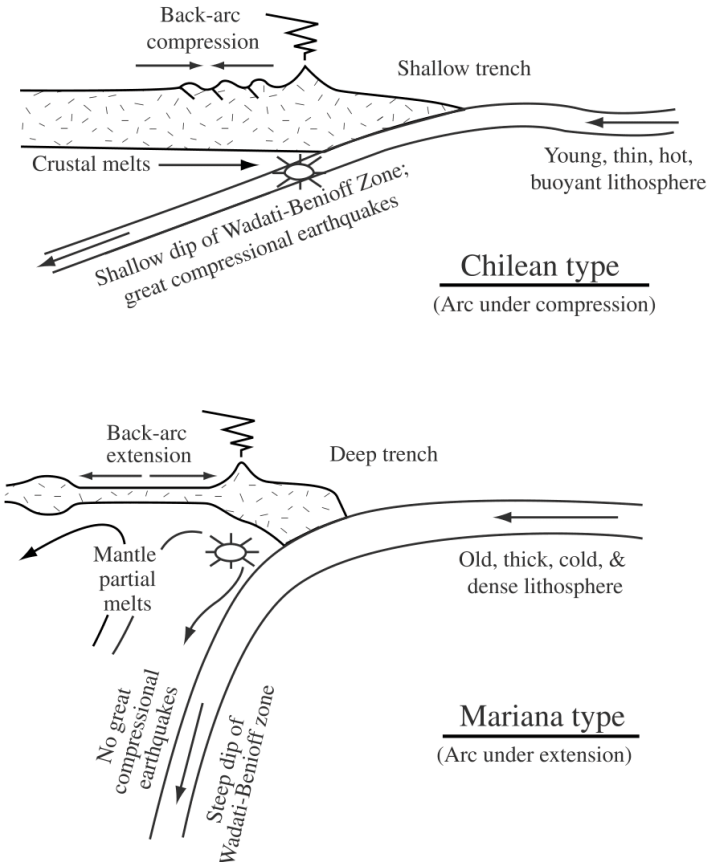

685

686 **Figure 2.17.** Two different types of subduction zones (Uyeda and Kanamori
687 1979).

688

689 Large shallow thrust earthquakes are generated along subduction zones with
690 strong inter-plate locking at the plate interface. The faulting of these earthquakes

occur in a certain depth range called the seismogenic zone. The area of this zone covers 2-5% of the total down-dip length of the Wadati-Benioff Zone. Actual depths of such seismogenic zones are inferred from the rupture areas of interplate earthquakes. In some cases, adjacent segments rupture shortly after a large interplate earthquake. However, mechanisms governing such induced ruptures are not fully understood. The acceleration of the slab subduction, explained in the previous section, would be a candidate mechanism for this phenomenon.

In the slab acceleration model by Heki and Mitsui (2013), the slab length in the subduction zone is one of the factors controlling the amount of the slab acceleration after major earthquakes. Many past studies have revealed the dimension of the slab by seismic tomography, a method that utilizes a lot of ray paths to gain information about seismic velocity structure. The seismic velocity from various points near earth surface propagate into earth interior and reach different depth. Then, by using tomography technique, three-dimensional (3-D) model of velocity anomalies can be obtained (Figure 2.18). I obtained the information on the lengths of worldwide slabs by tomographic studies such as Deal and Nolet (1999), Scire et al. (2017), Hafkenscheid et al. (2001), Husker and Davis (2009).

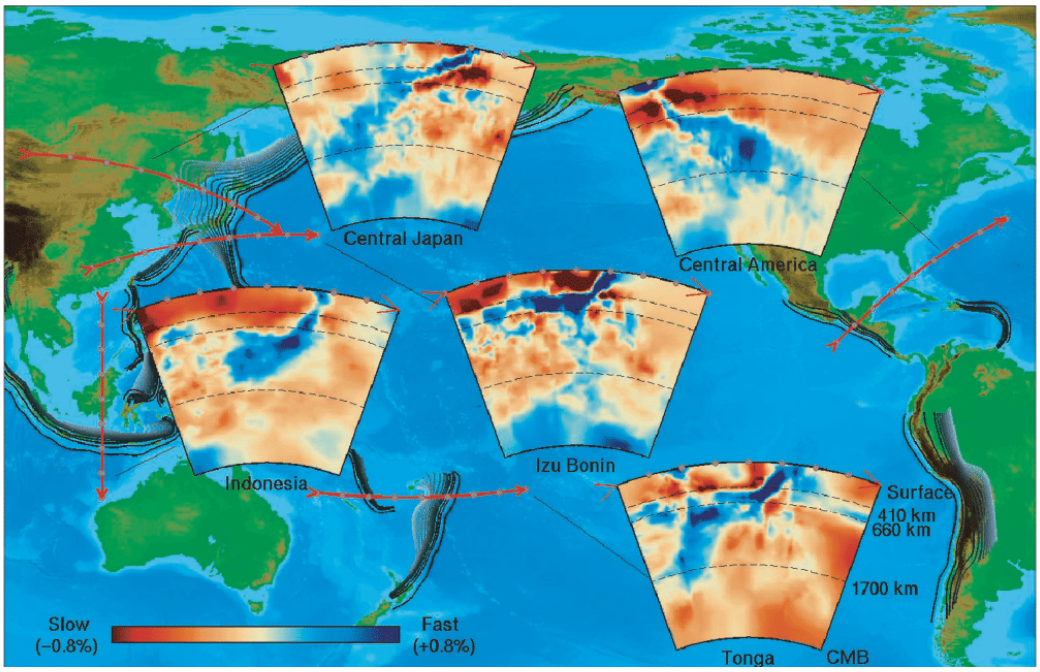

Figure 2.18. Cross section of seismic wave velocity anomalies in various subduction zone inferred from seismic tomography (Stern, 2002).

Chapter 3: Enhanced interplate coupling after various megathrust earthquakes

3.1 The cases in Japan

3.1.1 Tectonic setting in Northeast Japan

The Pacific Plate is a major oceanic plate, covering some of the oldest sections of the oceanic lithosphere. It is also one of the plates that meet, in the Japanese Islands, with other plates such as North American (or Okhotsk), Philippine Sea, and the Eurasian (or Amurian) Plate. The interactions among these tectonic plates cause complicated tectonic evolution, seismicity, volcanism, and crustal deformation in the Japanese Islands, composed of multiple island arcs such as NE Japan Arc SW Japan Arc in the center, Ryukyu Arc to the southwest, Izu-Ogasawara Arc to the south, and the Kuril Arc to the northeast.

The Pacific Plate subducts along the Kuril and Japan Trenches beneath the Okhotsk Plate at a velocity of ~90 mm/yr. The definition of the Okhotsk Plate depends of researchers. Some authors claim existences of microplates along the boundary between the two major plates, the Eurasian and the North American Plates, and these include the Amur and Okhotsk microplates in regions originally considered as parts of the Eurasian and North American Plates, respectively. The Japan Trench has a radius of about 400 km with concave-shaped westward in the southern part, whereas, in the northern part, it is convex-shaped eastward (Niitsuma,

2004). The coast, backbone ranges, intermountain basins, volcanoes, and seismicity run in parallel with the trench axes. The oceanic crust in this region was formed at ca. 125-140 Ma and covered by pelagic sediments 1.6 km thick with a thick and accretionary prism along the Japan trench (Kodaira et al., 2017). Several seamounts and fracture zone were found in the oceanic crust in the northwestern Pacific Plate (Choe and Dyment, 2020). A tomography study by Deal and Nolet (1999) suggests that the length of the subducting slab of the Pacific Plate beneath the Okhotsk Plate is ~1075 km. In the slab length interpretation above, I exclude the stagnant slab of the Pacific Plate, which is deflected and flattened underneath the eastern China (Fukao et al., 2009).

3.1.2 The 2011 Tohoku-oki earthquake (M_w 9.0)

The 2011 Tohoku-oki earthquake occurred off the Pacific coast of the Northeast Honshu (Tohoku District), Japan. It was caused by shallow thrust faulting at the plate boundary between the Pacific Plate and the Okhotsk (North American) Plate. The Pacific Plate moves west-northwestward relative to the Okhotsk Plate with a velocity of ~91 mm/year (Argus et al., 2011) and subducts underneath the NE Japan arc at the Japan Trench. During the one hundred years period prior to the 2011 Tohoku-oki earthquake, fourteen M_w7 class earthquakes and two M_w8 class interplate earthquakes occurred along this plate boundary (Tajima et al., 2013).

Shortly after the 2011 earthquake, the tsunami alert was issued by the Japan Meteorological Agency (JMA) along the Pacific coast of Honshu and Hokkaido with the prediction of maximum potential tsunami run-up height was 6 m. However, the actual tsunami run-up height was up to 40 m, wiped out the coastal towns, and

inundated deeper to the inland area (Ritsema et al., 2012; Takano, 2011).

The epicentral depth of this earthquake was about 20 km, 19.7 km, and 25 km according to the Harvard Centroid Moment Tensor (CMT) solution, International Seismological Centre (ISC), and United States Geological Survey (USGS), respectively. Focal mechanism of this earthquake is consistent with slip on the surface of the subducting Pacific Plate slab. USGS Finite fault modelling (Figure 3.1) indicates that the fault slipped over an area approximately 400 km long (along strike) by 150 km wide (in the down-dip direction). The average slip is estimated to be 50-60 m.

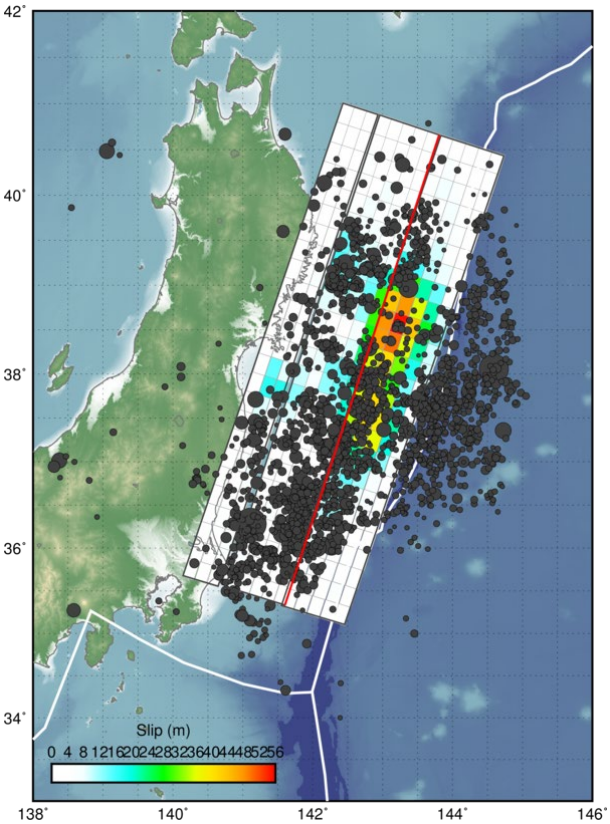

Figure 3.1. Surface projection of the slip distribution of the 2011 Tohoku-oki earthquake (M_w 9.0). Thick white lines indicate major plate boundaries. Dark gray circles are aftershock locations, sized by magnitude (Source: USGS https://earthquake.usgs.gov/earthquakes/eventpage/official20110311054624120_30/finite-fault).

776 This earthquake was accompanied by a foreshock sequence lasting for ~2 days,
777 beginning with a M_w 7.3 event on March 9, at a point ~40 km to the north of the
778 mainshock epicenter. On the following day, additional six earthquakes greater than
779 M_w 6.0 occurred within 24 hours (Kiser and Ishii, 2012; Marsan and Enescu, 2012).
780 Within three months following the mainshock, more than one thousand aftershocks
781 were detected by >100 ocean-bottom seismometers (OBS) deployed off the Pacific
782 coast of the Tohoku District (Shinohara et al., 2012).
783 This earthquake generated large-scale postseismic deformation (e.g. Yamagiwa
784 et al., 2015). Such postseismic deformation, characterized by southeastward
785 velocity, seems to reach the southeastern half of Hokkaido. Beyond these regions
786 with trenchward postseismic movements, Heki and Mitsui (2013) showed that the
787 enhanced interplate coupling signatures are seen in eastern Hokkaido, the segment
788 to the northeast of the Tohoku-oki rupture.
789

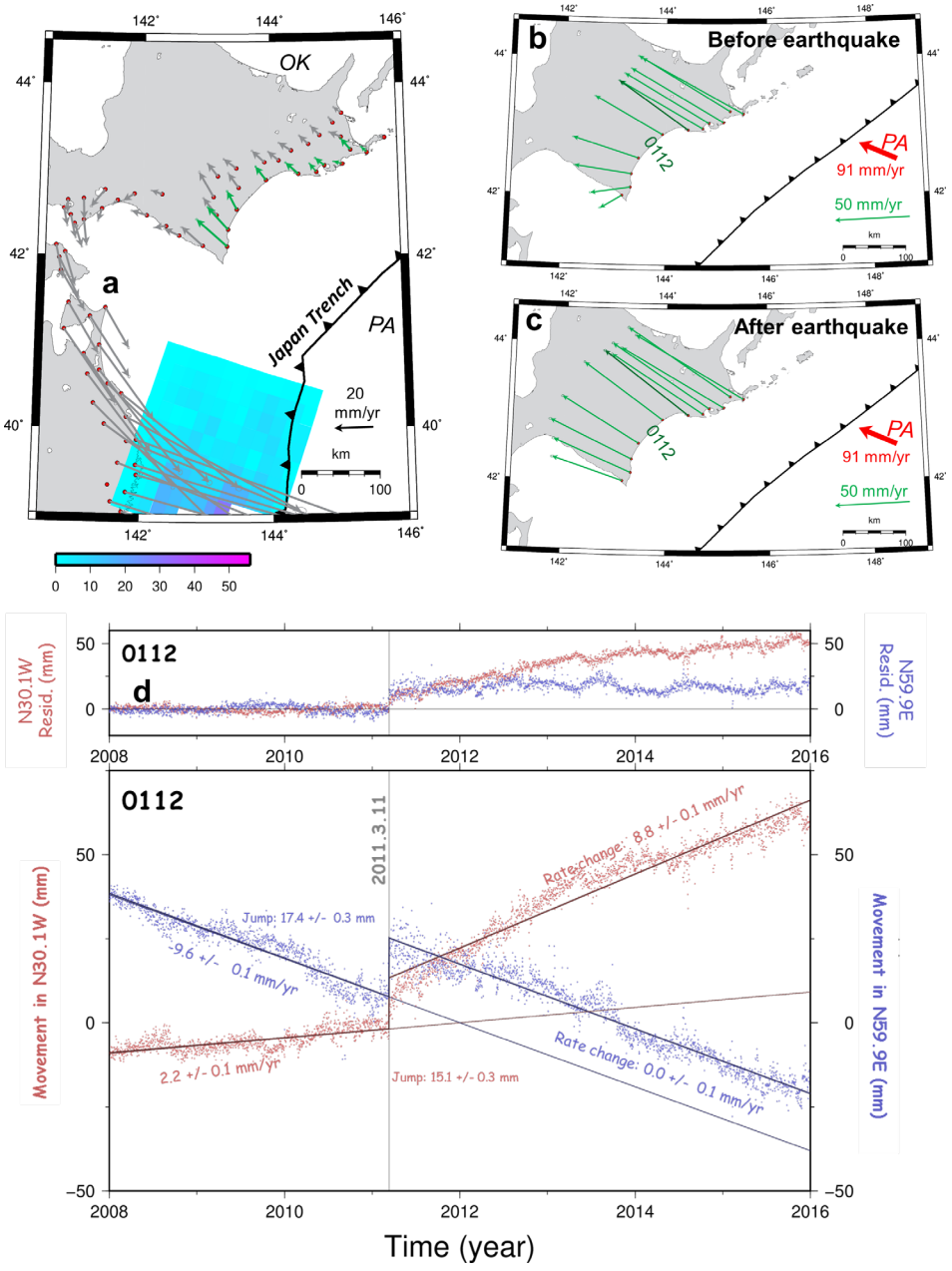

Figure 3.2. (a) Differences of the velocities following the 2011 Tohoku-oki earthquake (during 2012.00-2015.00) relative to the reference velocities before the earthquake. GNSS stations with green arrows in (a) are free from the trenchward postseismic crustal movement, caused by afterslip and viscoelastic relaxation, and are used for further analyses. In (b) and (c), the green arrows show interseismic landward movements of GNSS stations before and after the 2011 Tohoku-oki earthquake relative to the Okhotsk Plate (Table 1 summarizes the periods used to estimate these velocities). The red arrow represents the Pacific Plate movement relative to the Okhotsk Plate (Argus et al., 2011). Error ellipses show 2σ errors. (d) shows the time series of the 0112 station, the dark green arrow in (b), (c). See Figure 2.13 for the meaning of red (trench-normal, N30.1W here) and blue (trench-parallel, N59.9E here) components. The top

803 panel of (d) shows the de-trended time series.
804
805 Figure 3.2a shows the difference of the velocities before and after the 2011
806 Tohoku-oki earthquake. There, the start time of the period to estimate postseismic
807 velocity is shifted to 2012.0 to avoid the strong non-linear behavior of the early part
808 of the postseismic time series. The movements of the stations are reasonably linear
809 in this period, but possible influences of non-linear movements are discussed later
810 in Chapter 4.3. We can see that trenchward postseismic movements prevail in the
811 Tohoku District and the western half of Hokkaido. The eastern Hokkaido shows, on
812 the other hand, the typical enhanced interplate coupling signature, i.e. the velocity
813 changes are northwestward. In drawing velocities in Figure 3.2, I converted the
814 velocity in ITRF to the frame fixed to the Okhotsk plate using the nnr-MORVEL56
815 model (Argus et al., 2011).
816 Figure 3.2b, c shows crustal movements before and after the 2011 Tohoku-oki
817 earthquake at six stations 0519, 0512, 0009, 0125, 0531, 0010, 0112, 0138, 0015,
818 and 0532 (from northeast to southwest). Because the postseismic trenchward
819 movements of the 2003 Tokachi-oki earthquake still continued in 2011, their
820 velocity vectors deviate significantly in azimuth from the subduction direction of
821 the Pacific Plate. Nevertheless, as seen in Figure 3.2a, the velocity changes at
822 2011.19 is clearly in the direction of the subduction, i.e. the pre-earthquake
823 landward movement of the GNSS stations has increased after the 2011 Tohoku-oki
824 earthquake.
825 In Figure 3.2d, I show the diagram similar to Figure 2.13 for the station 0112,
826 where the landward velocity increase of 8.8±0.1 mm/yr is seen. Such an error for
827 the increase represents 2σ. It is scaled with post-fit residuals but may underestimate

the real uncertainty. For the cases with data available from multiple stations, I use the scatters of their increase to express their uncertainties for later discussions of the model. One large difference from the typical case (Figure 2.13) is that even the component perpendicular to the subduction direction (trench-parallel, blue component in Figure 3.2d) has significant slopes. This component simply reflects the continuation of the postseismic movement of the 2003 Tokachi-oki earthquake, and these slopes do not show any change by the 2011 Tohoku-oki earthquake. Similar time series from two additional stations are given in Figure 3.3. Change in seismicity in the region showing enhanced landward movements are discussed in Chapter 4.2. We also demonstrate that the postseismic movements of the 2003 Tokachi-oki earthquake are linear enough in 2008-2011 and its curvature does not influence the postseismic velocity change of the 2011 earthquake as discussed later in Chapter 4.3.

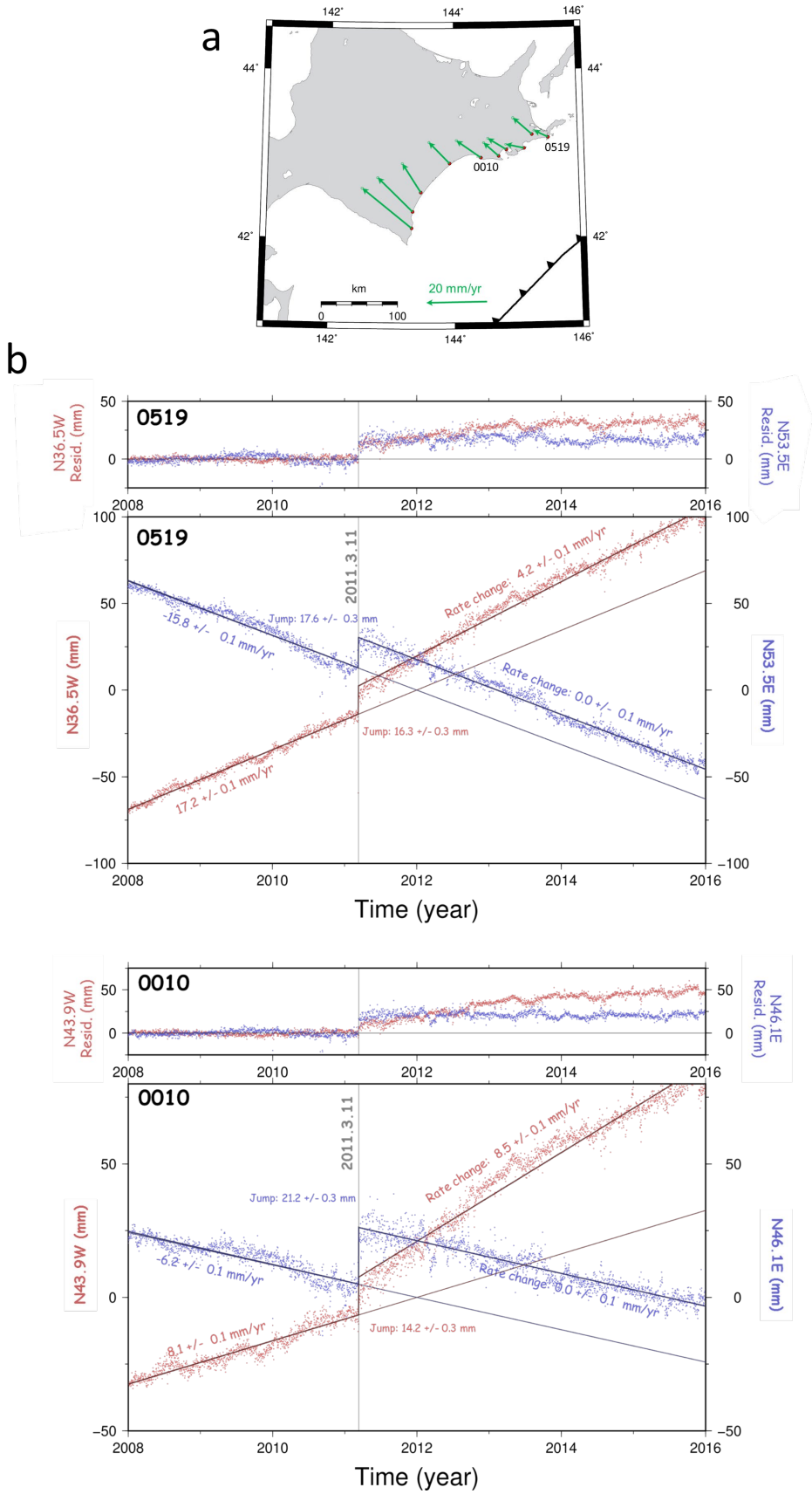

841

842 **Figure 3.3.** (a) Horizontal velocity changes associated with the 2011 Tohoku-

oki earthquake in Hokkaido (same as stations with green arrows in Figure 3.2a). Time series of the two labeled stations (0010, 0519) are shown in (b). The components shown in blue colors are determined as the direction perpendicular to the velocity changes by the earthquake. The components in red are taken perpendicular to them.

3.1.3 The 2003 Tokachi-oki Earthquake (M_w 8.3)

On September 25, 2003, a large interplate earthquake occurred near Hokkaido, Japan, as the result of shallow thrust faulting on or near the plate interface between the overriding Okhotsk Plate (or North American Plate) and the subducting Pacific Plate. The epicenter was in the same location as the 1952 Tokachi-oki earthquake and could be considered as the recurrence of the 1952 event, although their slip distributions are a little different. Based on the analysis of the aftershock distribution by Takahashi and Kasahara (2004), the source region of the 2003 event is slightly smaller than that of the 1952 event.

In this region, the Pacific Plate is moving west-northwest at a velocity of about 91 mm/yr relative to the Okhostk Plate (Argus et al., 2011), subducting beneath Japan at the Japan Trench. This earthquake generated tsunami with the largest height of ~4 m (Tanioka et al., 2004). The coseismic slip distribution of the 2003 earthquake by USGS (Figure 3.4) indicates thrust faulting with a shallow dip angle (strike= 240.0°, dip = 17.0°) of a fault plane with the length 272 and width 227 km.

Before the 2003 Tokachi-oki earthquake, eastern Hokkaido experienced many large interplate earthquakes. Earthquakes with M_w 8.2 and M_w 7.7 occurred in 1968 and 1994, respectively, to the southwest of the 2003 earthquake rupture area. The 1994 earthquake ruptured the southern half of the 1968 rupture area. On the other

hand, the M_w 7.8 Nemuro-Oki earthquake in 1973 ruptured a fault to the east of the 2003 earthquake. The aftershocks of the 2003 earthquake occurred in the segment between the 1968 and the 1973 ruptures. This suggests that the 2003 earthquake filled the seismic gap left between the 1968 and 1973 earthquakes. In addition to such interplate earthquakes, eastern Hokkaido also suffers from large earthquakes within the subducting Pacific Plate slab such as the Kushiro-oki earthquake on January 15, 1993.

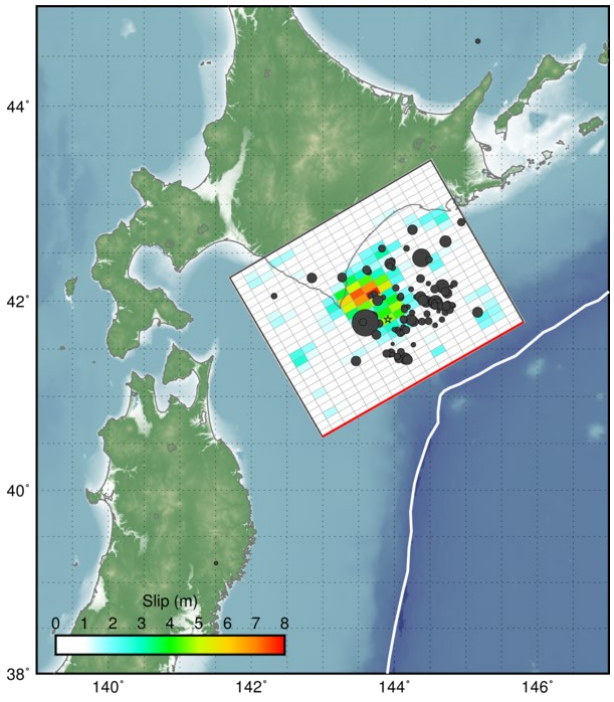

Figure 3.4. Surface projection of the slip distribution of the 2011 Tohoku-oki earthquake (M_w 8.3). Thick white lines indicate major plate boundaries. Dark gray circles are aftershock locations, sized by magnitude (Source: USGS https://earthquake.usgs.gov/earthquakes/eventpage/usp000c8kv/finite-fault).

Postseismic deformation signatures observed using the GEONET data are well documented (e.g. Miyazaki et al., 2004; Itoh and Nishimura, 2016). It is this earthquake that Heki and Mitsui (2013) found postseismic enhanced interplate

coupling, for the first time, at the segments adjacent northeastward and southwestward to the ruptured segment.

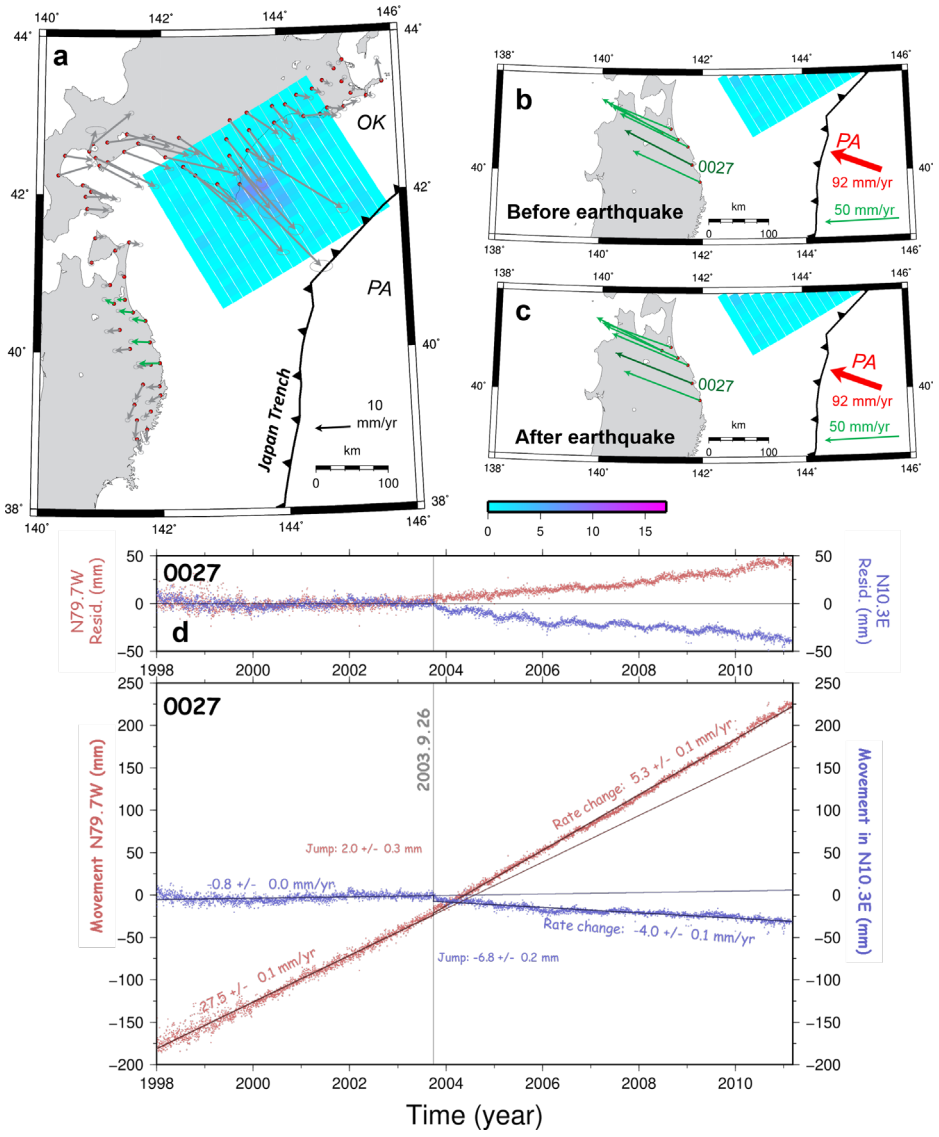

Figure 3.5 Maps and diagram demonstrating the postseismic landward velocity changes for the 2003 Tokachi-oki earthquake. Meaning of symbols are the same as those in Figure 3.2. (a) Differences of the velocities in 2008.7-2010.0 relative to the pre-2003.00 velocities (I removed data before 1998.0 to avoid influences from postseismic movements of the 1994 Sanriku earthquake, see Chapter 4.3), reproduction of a part of Figure 2a of Heki and Mitsui (2013). In (b) and (c), I compare the velocities before and after the 2003 earthquake for stations showing postseismic enhanced coupling in (a). Red arrow represents the Pacific Plate movement relative to the Okhotsk Plate (Argus et al., 2011). The time series of the 0027 station (dark green arrow in b, c) is shown in (d) for the trench-normal (red) or trench-parallel (blue) components.

902 Figure 3.5 shows the maps and diagram similar to Figure 3.2 for the 2003
903 Tokachi-oki earthquake. I selected the GNSS stations with landward velocity
904 changes located along the Pacific coast of the northernmost Honshu (stations with
905 green vectors in Figure 3.5a, 0153, 0156, 0158, 0162, 0027, 0539 from north to
906 south). Figure 3.5b, c shows interseismic velocities before and after the earthquake.
907 Here I used the F3 solution and followed the procedures in Heki and Mitsui (2013),
908 i.e., I fixed the Kamitsushima station, Kyushu, Japan, which is not much different
909 from the frame fixed to the Okhotsk Plate used for the 2011 earthquake (Figure 3.2).
910 In Figure 3.5d, I show time series of the trench-normal (red) and trench-parallel
911 (blue) components for the 0027 station. There I can see the increased landward
912 movement of 5.3 mm/yr. Similar time series from two additional stations are given
913 in Figure 3.6.

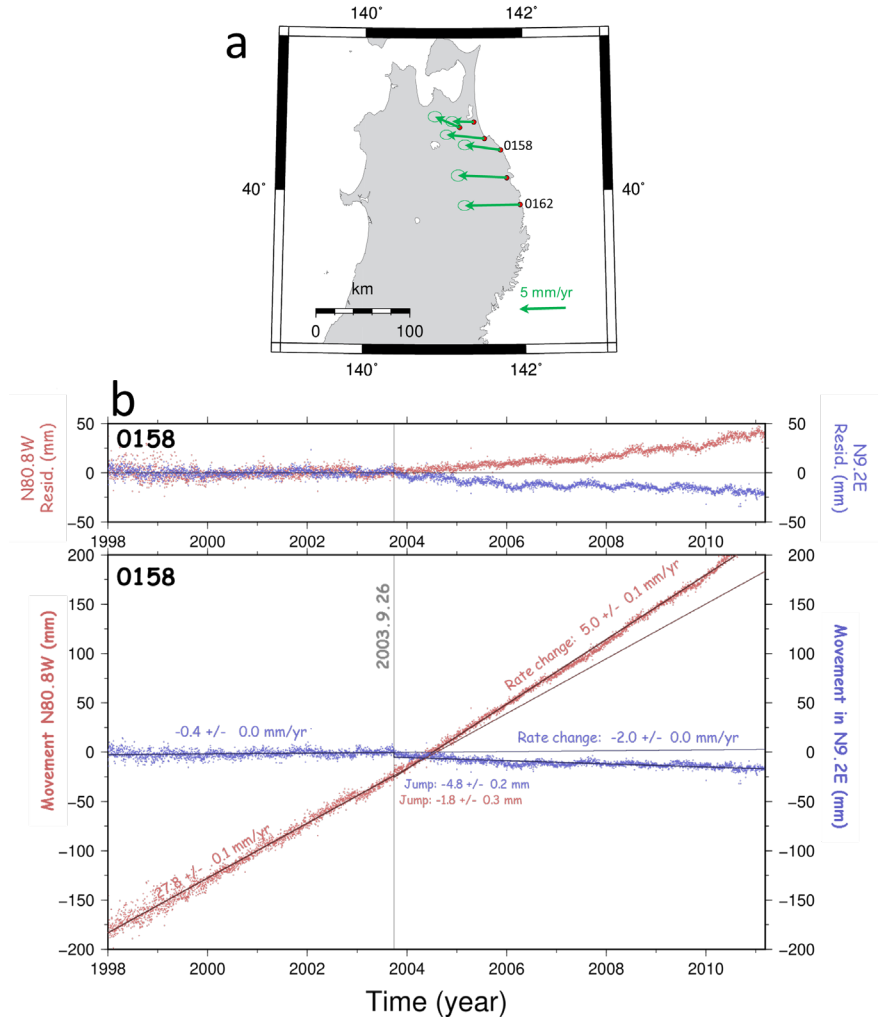

Figure 3.6. (a) Horizontal velocity changes associated with the 2003 Tokachi-

oki earthquake (same as stations with green arrows in Figure 3.5a). In (b), we show time series of horizontal positions of the two stations 0158 and 0162 before and after the earthquake.

As reported in Heki and Mitsui (2013), I also found that the velocity in the trench-parallel direction (N9.0E) has also changed the rate by -4.0±0.1 mm/yr. This reflects the slight counterclockwise rotation of the velocity as recognized by comparing Figures 3.5b and 3.5c. This might be due to postseismic viscous relaxation occurring as a slow movement away from the fault (together with the trenchward movement), which is visible in the numerical simulation results given in Figure 1.7b. Melnick et al. (2017), in their Figure 4, also shows that similar outward movements are reproduced as a result of vertical axis crustal rotation.

As described earlier, Mavromatis et al. (2014) suggested that this landward velocity change indicates the termination of the postseismic trenchward movement caused by the 1994 M_w 7.6 Sanriku-oki earthquake (Heki et al., 1997). However, this cannot be a significant factor partly because their model does not explain the landward velocity change on the other side (easternmost Hokkaido) after the 2003 earthquake (Figure 3.5a).

Additional evidence comes from the velocity of 0027 prior to the 2003 earthquake (Figure 3.7). In order to confirm the influence of the postseismic movement of the 1994 Sanriku-oki earthquake on the coseismic velocity changes of the 2003 Tokachi-oki earthquake at stations in NE Honshu, I plot the baseline length (distance) between the 0027 station (Figure 3.5) on the Pacific coast and the 0184 station on the Japan Sea coast.

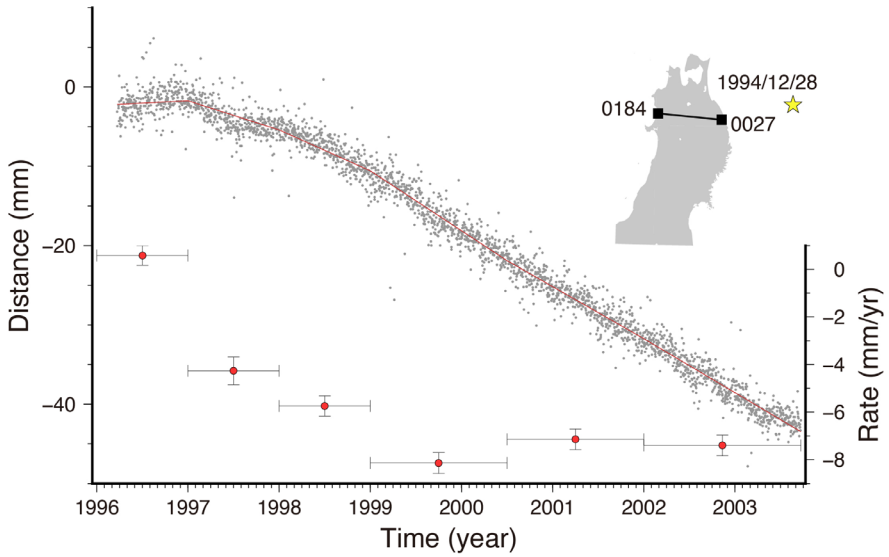

Figure 3.7. The change of the baseline length connecting the 0027 and 0184 stations between the 1994 Sanriku-oki and 2003 Tokachi-oki earthquakes (the F3 solution not available before 1996 March). Slopes are estimated in different time windows of 1-1.5 years. The vertical error bars indicate 2σ uncertainties. This demonstrates that significant influence of the postseismic crustal movement extends only until ~1998.

In Figure 3.7, the time series are modeled with lines with breaks at 1997.0, 1998.0, 1999.0, 2000.5, 2002.0. In 1996-1998, the distance does not show significant changes due possibly to the balance of the landward (interseismic strain) and oceanward (postseismic movement of the 1994 event) velocities of 0027. As the latter decay, the slope becomes stationary. In fact, the effect of postseismic transient of the 1994 Sanriku-oki earthquake remains dominant only until 1997-1998. I excluded data before 1998.0 in deriving the pre-2003 velocity (Figure 3.5d). Therefore, the postseismic transient of the 1994 earthquake would not significantly affect the estimated velocity increases in 2003 September.

3.2 The cases in Chile

3.2.1 Tectonic setting in Central and Northern Chile

Chile is a country located along the west coast of South America and situated

963 in one of the world's most active tectonic regions. This long but narrow country lies
964 on or is close to four tectonic plates: The South American Plate, the Nazca Plate,
965 the Scotia Plate, and the Antarctic Plate. The Chile subduction zone, stretching more
966 than 3500 km, is segmented by the subduction of the Chile Rise and by the Juan
967 Férnandez Ridge.

968 The Chile Rise is an active spreading center that indicates the margin between
969 the Nazca Plate to the north and the Antarctic Plate to the south. The Chile Rise first
970 collided with the continent south of 48° S, in the Tierra del Fuego, at ~14 Ma and
971 then migrated northward to the current location of triple junction. Consequently, the
972 span of the Antarctic–South America subduction zone has increased during this
973 period (Cande and Leslie 1986).

974 The Juan Férnandez Ridge is a gentle topographic swell created by a series of
975 disconnected, large seamounts. The most notable seamounts on the oceanic plate
976 near the central Chile trench are the O'Higgins guyot and O'Higgins seamount,
977 located in the easternmost portion of Juan Férnandez Ridge before subduction. The
978 Juan Férnandez Ridge has been colliding with the Chilean margin in the north (at
979 ~20°S) since ~22 Ma, and the collision front migrated southward to the current
980 collision zone offshore Valparaíso (~32.5°S) (Yáñez et al., 2001).

981 The eastern side of the Nazca Plate forms the Peru-Chile Trench, the
982 convergent margin with the overriding South American Plate, and the Andean
983 Mountain Range is the continental arc made by this plate convergence. The Nazca
984 Plate currently moves eastward relative to the South American Plate with a velocity
985 of ~74 mm/year (Argus et al. 2011). The direction of the movement is almost
986 perpendicular to the trench. The age of the Nazca Plate in North and Central Chile

ranges from ~37 Ma to ~48 Ma (Müller et al.1997).

Tomographic model of the seismic wave velocity structure of the mantle in the area of the 2010 M8.8 Maule earthquake and surrounding regions (Pesicek et al., 2012) shows that the length of the slab is ~1,100 km. On the other hand, the length of the Nazca slab under South America from 6°S to 32°S is also ~1,100 km from tomographic studies (Scire et al., 2017).

3.2.2 The 2010 Maule Earthquake (M_w 8.8)

Fast convergence between the Nazca and the South American Plates causes recurrent megathrust earthquakes along the Peru-Chile Trench off the Pacific coast of South America. The 2010 February Maule earthquake, one such event in central Chile, filled the seismic gap lasting since the 1835 Conception earthquake. In addition to the co- and postseismic crustal deformation of this earthquake reported in Vigny et al. (2011), Moreno et al. (2012), and Klein et al. (2016), Melnick et al. (2017) reported postseismic increase of the landward velocities of stations located to the north of the rupture. They further suggested that such enhanced coupling may have triggered the occurrence of the 2015 Illapel earthquake (M_w 8.3) to the north of the 2010 rupture.

Klein et al. (2016) reported large-scale postseismic oceanward movements of GNSS stations around the ruptured segment, and it can be seen in velocity changes by the 2010 earthquake in Figure 3.8a. We also can see that stations located to the north of the 2010 rupture show clear signatures of enhanced interplate coupling (green vectors in Figure 3.8a). The velocities of these GNSS stations before and after the earthquake are shown in Figure 3.8b and c, respectively. Figure 3.8d shows

the horizontal movement in the direction parallel with (red) and perpendicular to (blue) the before-earthquake interseismic velocity of the CNBA station.

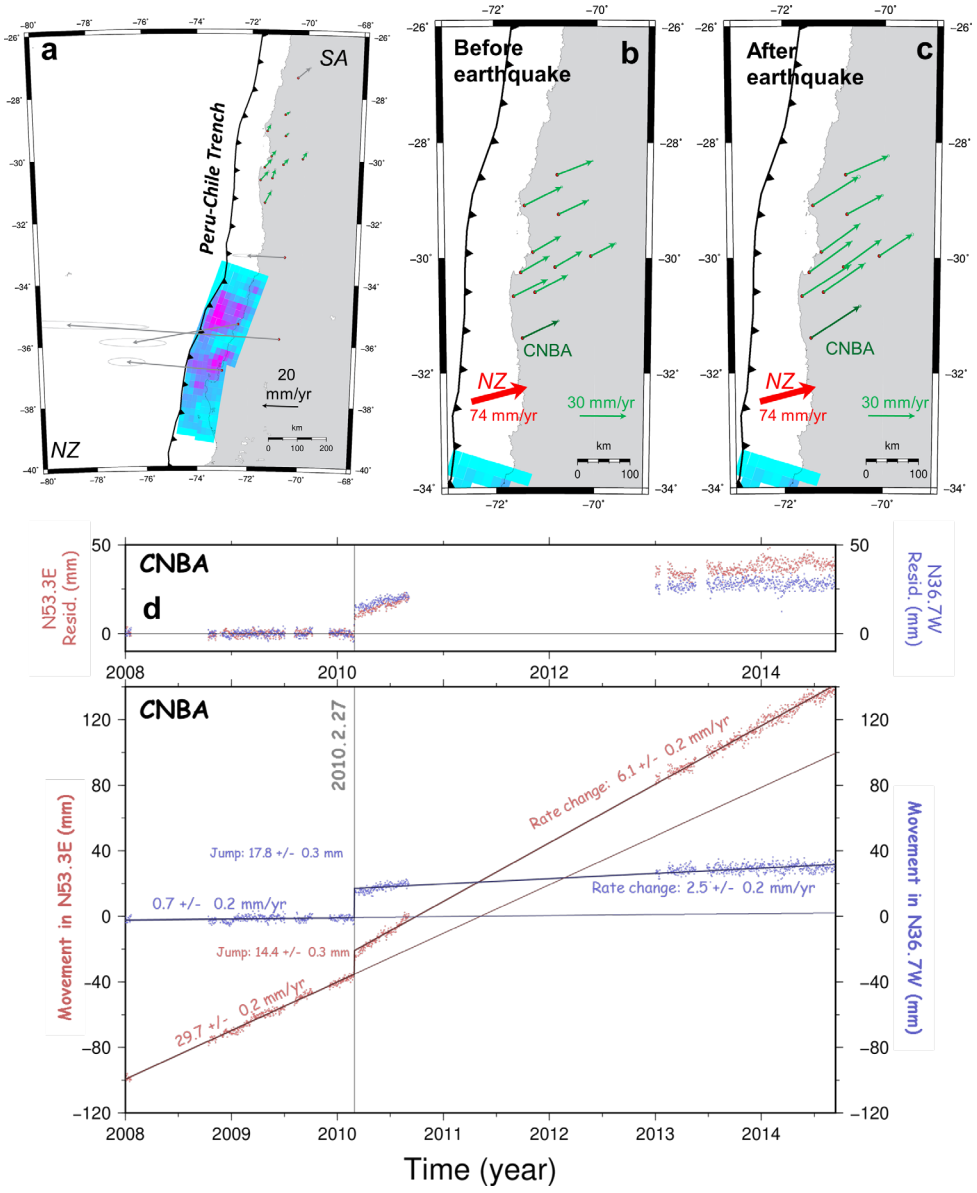

Figure 3.8. Maps and diagram demonstrating the postseismic landward velocity change for the 2010 Maule earthquake. (a) Differences of the postseismic velocities from those before the earthquake. In (b) and (c), I compare the velocities before and after the earthquake for stations showing enhanced coupling. The red arrow represents the Nazca Plate velocity. These velocities are all relative to the South American Plate. The time series of the CNBA station (dark green arrow in b, c) is shown in (d) using the horizontal directions parallel with (red) or perpendicular to (blue) the velocity before the earthquake. If I exclude data from 2010.17-2011.00, the rate change is reduced to 5.0±0.2 mm/yr.

The red component shows velocity increase of 6.1±0.2 mm/yr. There is some misfit of the data to the straight line in the 2010 data. This suggests that the postseismic landward velocity increase is somewhat larger immediately after the earthquake than that after a few years. However, such a non-linear movement cannot be seen in the two Japanese cases discussed in sections 3.1.2 and 3.1.3.

It is also interesting to see that the blue component shows the postseismic slow movement away from the fault, a feature also observed after the 2003 Tokachi-oki earthquake (Figure 3.5d). The stations in Figure 3.8b and 3.8c showing enhanced landward velocities, including CNBA, suffer from data gaps up to two years (Figure 2.6). Additional time series of two stations are given in Figures 3.9. Change in seismicity in the region showing enhanced landward movements are discussed later in Chapter 5.2.

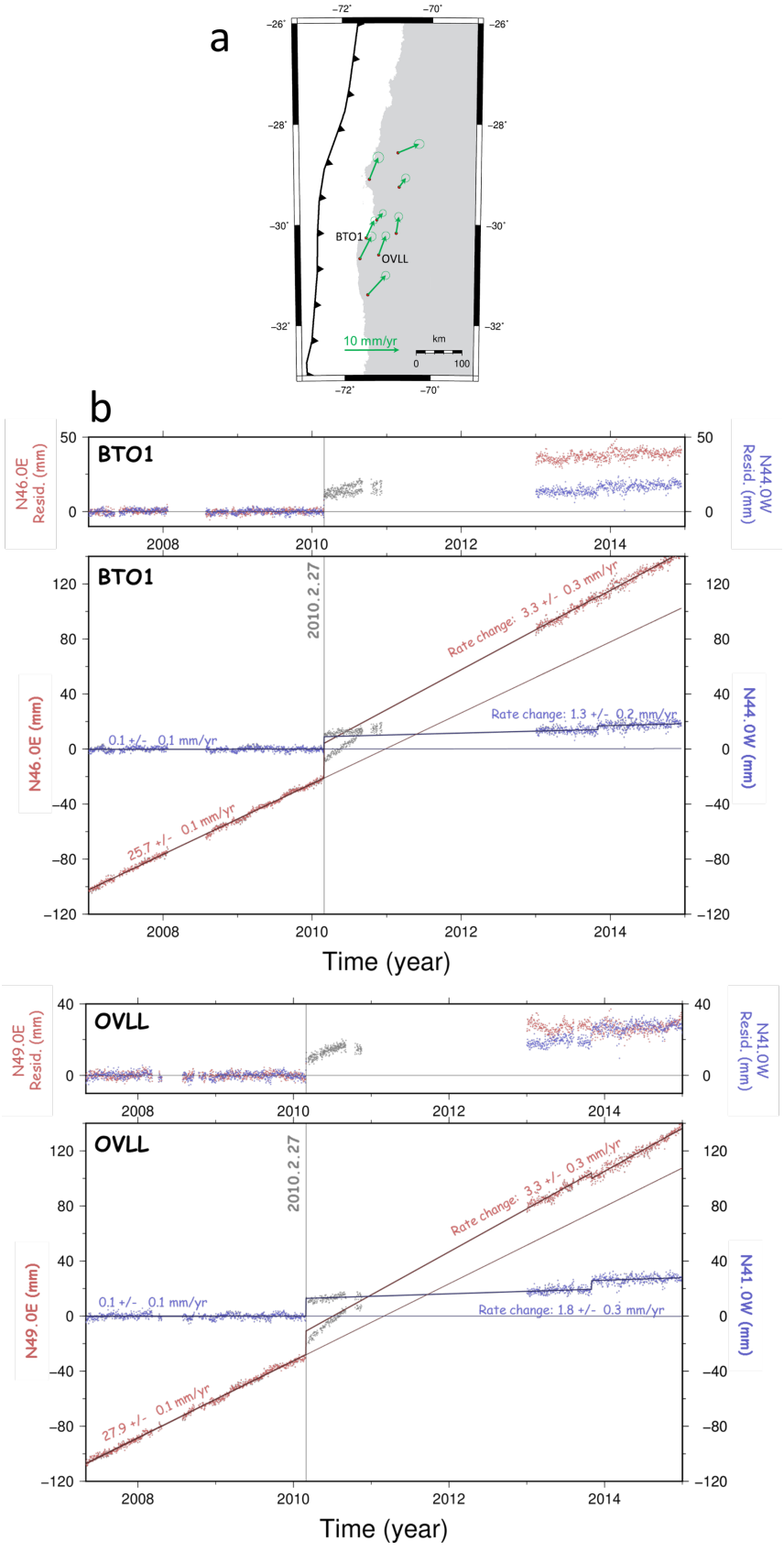

Figure 3.9. (a) Horizontal velocity changes by the 2010 Maule earthquake

(same as stations with green arrows in Figure 3.8a). In (b) we show time series of horizontal components at the two stations BTO1 and JUNT. These stations suffer from data gaps lasting for ~2 years.

3.2.3 The 2014 Iquique Earthquake (M_w 8.2)

The 2014 April Iquique earthquake occurred at a segment near the Peru-Chile border. This segment has been known as the north Chilean seismic gap with the last rupture by the 1877 Iquique earthquake (M_w 8.6) (Kelleher, 1972). Postseismic trenchward movements occur near the ruptured fault as the combined effect of the afterslip and the viscoelastic relaxation (Hoffmann et al., 2018). Figure 3.10a suggests that the stations located to the south of 21 S, as well as one station AREQ to the north, are not affected by such postseismic trenchward movements.

Figure 3.10d shows the SRGD station to the south of the rupture, showing small landward velocity increase of 2.8 mm/yr by the 2014 earthquake. On the northern side, AREQ shows the increase of 2.9 mm/yr. Both SRGD and AREQ stations are located at distances comparable to the fault length from the SE and NW edges of the fault. The time series of AREQ and an additional station to the south of the rupture are given in Figure 3.11.

Large interplate earthquakes occurred recently around the 2014 Iquique earthquake. To the north, the southern Peru earthquake (M_w 8.4) occurred near Arequipa in 2001, being followed by postseismic deformation continuing for at least two years (Perfettini et al., 2005). The rupture area of the 2001 earthquake seems to be coupled again a decade after the earthquake (Villegas-Lanza et al., 2016). I expect that the increasing of landward velocity at AREQ station after 2014 was not much influenced by the decay of the postseismic movement of the 2001 event.

To the south, the 2007 Tecopilla earthquake (M_w 7.7) (Schurr et al., 2012) and the 1995 Antofagasta earthquake (M_w 8.1) (Pritchard et al., 2002) did not significantly change the slip deficit in the studied region. Strong interplate coupling is confirmed in the 2014 Iquique earthquake focal region prior to the earthquake (Métois et al., 2013; Li et al., 2015). Hence, I think the influences from the postseismic movements of these earthquakes to the landward velocity change following the 2014 Iquique earthquake are small.

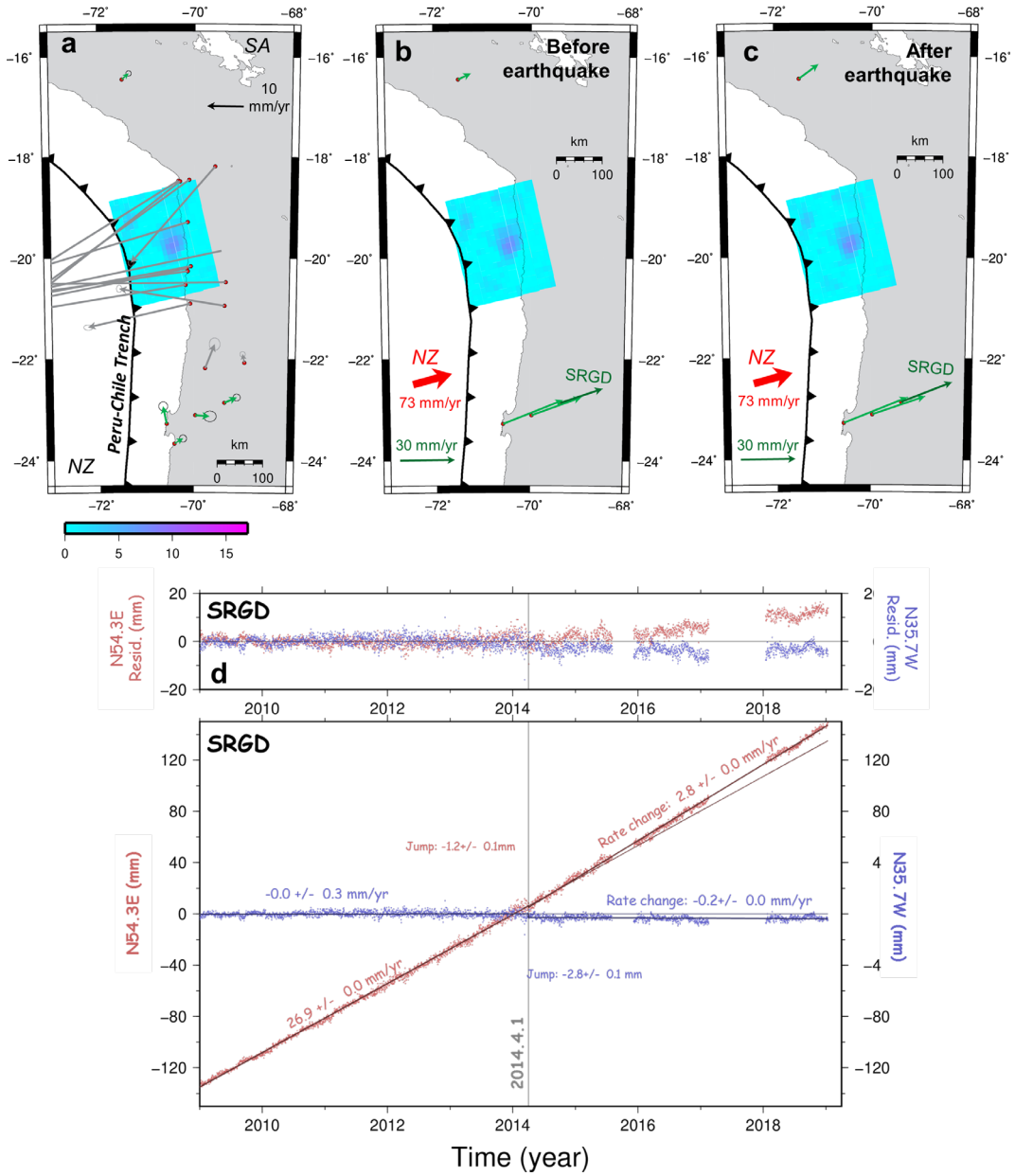

Figure 3.10. Maps and diagram demonstrating the postseismic landward velocity changes to the north and south of the 2014 Iquique earthquake rupture. (a) indicates the differences of the velocities before and after the earthquake shown in (b) and (c), respectively. The red arrow represents the Nazca Plate movement relative to the South American Plate. The time series of the SRGD station (dark green arrow in b, c) are shown in (d) in the trench-normal (red) or trench-parallel (blue) components.

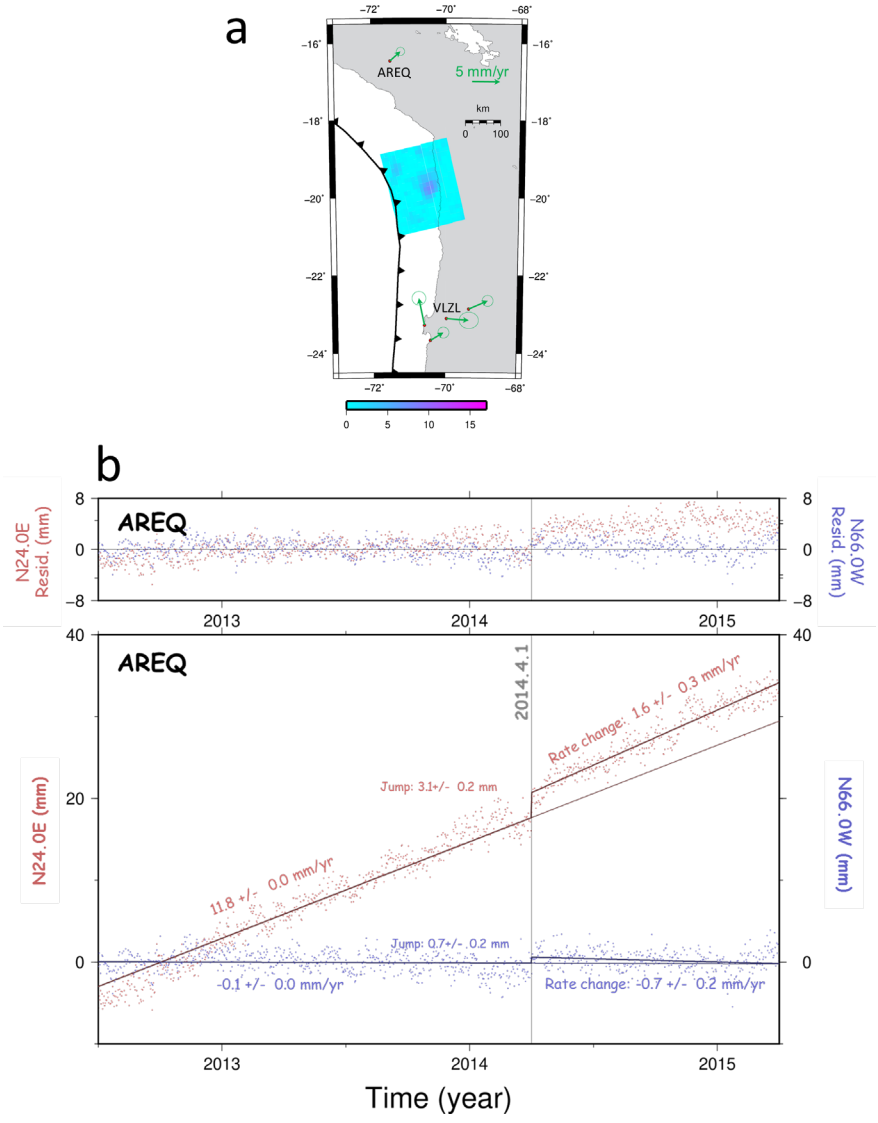
a
AREQ
5 mm/yr
km
0 100
VLZL
−72° −70° −68°
−16° −18° −20° −22° −24°
0 5 10 15
b
AREQ
N24.0E Resid. (mm)
N66.0W Resid. (mm)
2013 2014 2015
AREQ
2014.4.1
Rate change: 1.6 +/- 0.3 mm/yr
Jump: 3.1+/- 0.2 mm
11.8 +/- 0.0 mm/yr
Jump: 0.7+/- 0.2 mm
-0.1 +/- 0.0 mm/yr
Rate change: -0.7 +/- 0.2 mm/yr
N24.0E (mm)
N66.0W (mm)
Time (year)

1084

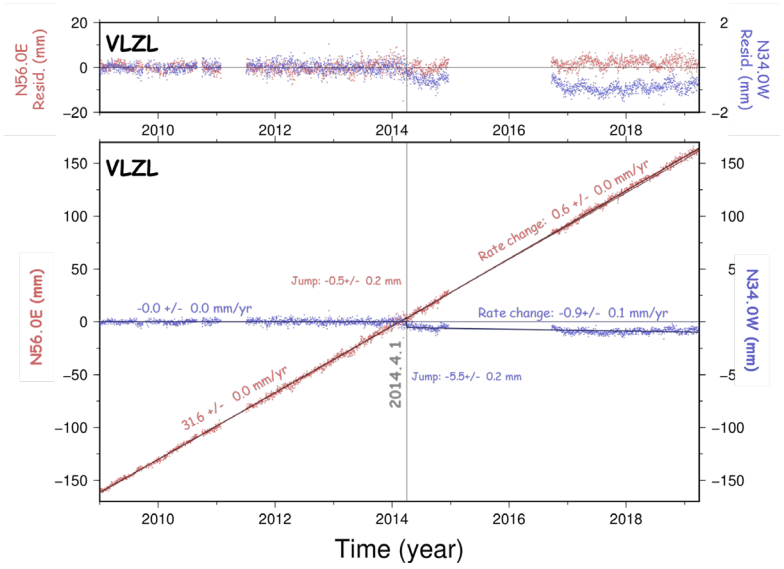
VLZL
N56.0E Resid. (mm)
N34.0W Resid. (mm)
2010 2012 2014 2016 2018
VLZL
Rate change: 0.6 +/- 0.0 mm/yr
Jump: -0.5+/- 0.2 mm
-0.0 +/- 0.0 mm/yr
Rate change: -0.9+/- 0.1 mm/yr
2014.4.1
Jump: -5.5+/- 0.2 mm
31.6 +/- 0.0 mm/yr
N56.0E (mm)
N34.0W (mm)
Time (year)

1085

Figure 3.11. (a) Horizontal velocity changes by the2014 Iquique earthquake (same as stations with green arrows in Figure 3.10a). In (b) we show time series of the two stations AREQ and VLZL.

3.3 The case in Sumatra

3.3.1 Tectonic setting in Southwest Sumatra

The Sunda Arc, which extends more than 4000 km, is formed by the subduction of the Indo-Australian Plate (or the Australian Plate) beneath the Eurasian Plate (or the Sundaland Plate). This arc ranges from the Andaman Sea in the northwest to the Banda Sea in the east. The region west of the Sumatra Island is one of the most seismically active and tectonically complex regions on the Earth. There are some debates regarding whether the Sundaland Plate is moving as a distinct lithospheric block or can be regarded as a stable continuation of its northward-neighboring Eurasian Plate (Simons et al., 2007).

The Sunda Arc is characterized by a high degree of volcanic activity of mostly andesitic composition (Curray, 1989). In the Sumatra subduction zone, which is a part of the Sunda Arc, the oceanic plate subducts beneath the landward plate obliquely (~40° at 2°N) with a convergence rate that varies along the trench from ~60 mm/yr at 6°S to ~52 mm/yr at 2°N (Prawirodirdjo et al., 2000). The subduction system has been active since at least the Oligocene and is much influenced by the late Eocene collision of the Indian subcontinent with Eurasia (Hamilton 1988). The age of the subducting plate varies from 40 Ma to 80 Ma (Muller et al., 2008), with the youngest oceanic crust subducting to the east of the Nias Island in northern Sumatra. To the west of the Sumatra Island, the forearc ridge emerges and forms an island chain, extending from the Simelue Islands in the northwest to the Enggano

Island in the southeast. To the south of the Java Island, this forearc ridge submerges below the sea level (Susilo Hadi et al., 2009). Tomographic model of the mantle in the area of the 2007 M_w 8.4 Bengkulu earthquake and surrounding regions by suggests that the length of the slab is ~700 km (Hafkenscheid et al., 2001).

3.3.2 The 2007 Bengkulu Earthquake (M_w 8.4)

The 2007 September Bengkulu earthquake occurred within the southern Sumatra subduction zone as a result of the oblique convergence of the two plates. In this region, the Australian Plate moves northeastward with respect to the Sundaland Plate at a velocity of about ~60 mm/yr (Argus et al. 2011). USGS Finite fault modelling indicates that the fault of this earthquake slipped over an area approximately 300 km long (along strike) by 110 km wide (in the down-dip direction, Figure 3.12).

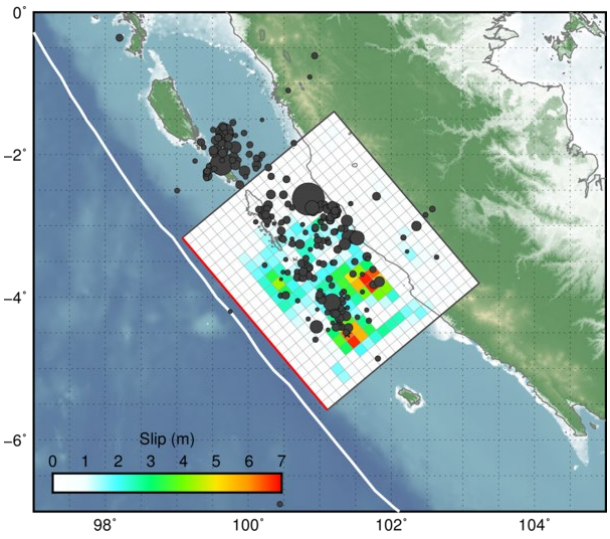

Figure 3.12. Surface projection of the slip distribution of the 2007 Bengkulu Earthquake (M_w 8.4) (Source: USGS https://earthquake.usgs.gov/ earthquakes/ eventpage/ official20070912111026830_34/finite-fault).

This region has been suffering from recurrent large earthquakes for a long time, with a series of large interplate earthquakes occurring since the 2004 December Sumatra-Andaman earthquake (M_w 9.2). Such earthquakes include the 2005 March Nias earthquake (M_w 8.5), the 2007 Bengkulu earthquake (M_w 8.4), and the 2010 Mentawai tsunami earthquake (M_w 7.9). In the past, similar megathrust earthquakes may have hit this area in 1797 and 1833 as inferred from studies of coral microatolls (Natawidjaja et al., 2006). I use the GNSS data of the MLKN station, one of the SuGAR (Sumatra GPS Array) station in the Enggano Island, to compare the velocity before and after the 2007 earthquake.

As seen in Figure 3.13a, stations on the rupture and on the northwestern segment show large trenchward postseismic movements. On the other hand, MLKN shows northeastward velocity change by the 2007 earthquake. An unusual situation for this station is that its interseismic velocity is not in the direction of the subduction. As seen in Figures 3.13b and 3.13c, which compare velocities before and after the 2007 earthquake, the station moves northwestward. This reflects the continuation of the postseismic movement of the 2000 Enggano earthquake (M_w 7.9), whose fault plane is indicated with a red rectangle (Abercrombie et al., 2003). In spite of this situation, the velocity change of MLKN in 2007 coincides with the plate subduction direction. Hence, I think it an example of the postseismic landward velocity changes studied here. The end of the postseismic period is taken at 2010.81, the occurrence time of the Mentawai earthquake, a M_w 7.9 typical tsunami earthquake that occurred close to the 2007 rupture (Satake et al., 2012). MLKN clearly shows the increase of the landward velocity at this segment.

I found the velocity change in the trench-normal component of 5.1 mm/yr

following the 2007 Bengkulu earthquake (Figure 3.13d). Unlike other cases, MLKN is located quite close to the southeastern edge of the fault of the 2007 earthquake. In this earthquake, the afterslip occurred mainly in the northwest part of the fault, which made the postseismic signals weak at MLKN. Lubis et al. (2012) calculated postseismic crustal movements of the 2007 earthquake by the viscoelastic relaxation, and the results showed insignificant movement around the MLKN station, and this support our interpretation that the velocity change of MLKN comes from the landward increased velocity of the 2007 earthquake.

This region is thought to be a part of the Sunda Strait seismic gap. Mignan et al. (2006) suggested that this area has remarkable accelerated seismic moment release similar to the area where maximum slip occurred during the 2004 Sumatra-Andaman earthquake. Hanifa et al. (2014) pointed out that the region off the southwestern coast of Java is a seismic gap with a high probability of future earthquakes. The enhanced coupling after the 2007 Bengkulu earthquake might contribute to accelerated strain accumulation in those segments.

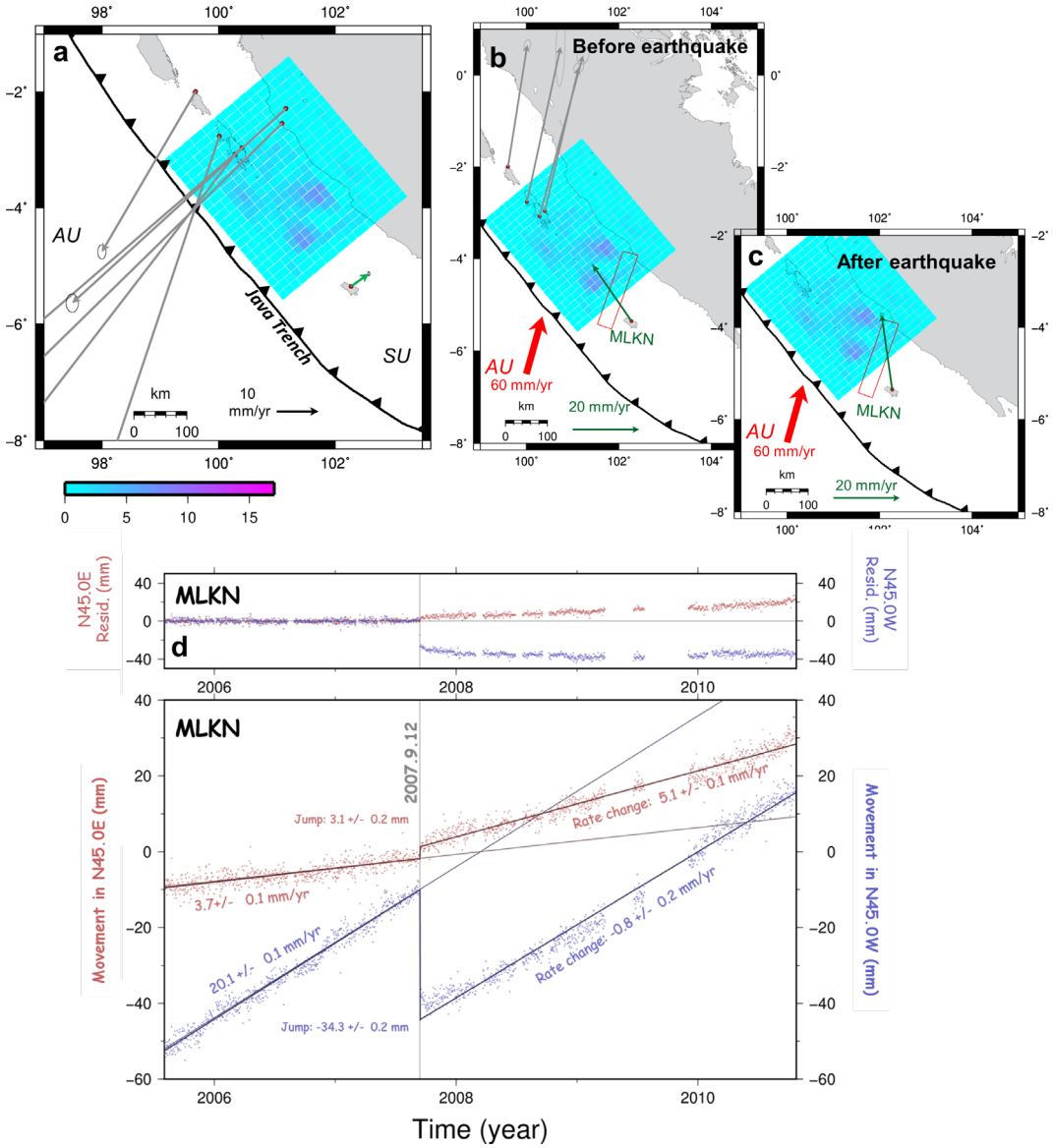

Figure 3.13. Maps and diagram showing the increased landward velocity after the 2007 Bengkulu earthquake. (a) Differences of the velocities (relative to the Sunda Plate) between periods before and after the earthquake shown in (b) and (c), respectively. The red arrow represents the Australian Plate subduction relative to the Sunda Plate. The red rectangle indicates the fault plane of the 2000 Enggano earthquake (M_w 7.9). The time series of the MLKN station is shown in (d) using the horizontal directions parallel with (red) or perpendicular to (blue) the subduction direction.

3.4 The case in Mexico

3.4.1 Tectonic Setting of Mexico

Mexico is located on The Middle America subduction zone, where the Rivera and

The Cocos Plates subduct beneath the North American and Caribbean Plates along the Middle America Trench. Around 30–28 Ma, a larger tectonic plate called the Farallon Plate, gradually split into several fragments, including the Rivera and Cocos Plate. This split began when the East Pacific Rise to interact with the North American Plate (Atwater and Stock, 1998). Cocos Plate is a relatively young oceanic plate (10–25 Ma) which subducts along the Middle America Trench at variable convergence rates 50 to 90 mm/yr (Manea et al., 2013).

3.4.2 The 2012 Oaxaca Earthquake (M_w 7.4)

Several significant earthquakes occurred in the region near the 2012 March Oaxaca earthquake, e.g. the 1932 M_w 7.9 earthquake, the 1995 M_w 8.0 earthquake, and the 1985 M_w 8.1 earthquake (Kanamori et al., 1993; Courboulex et al., 1997). For this earthquake, I could find only one station suitable for the present study, the OXPE station (Figures 3.14a, b), with meaningful time span before and after the earthquake and with position near the 2012 rupture. Our result showed a small increase of the landward component of the horizontal velocity of ~4.1 mm/yr (Figure 3.14c). This station is located at a distance comparable to the fault length from the SE edge of the fault.

It is difficult to know if earthquakes before the 2012 Oaxaca earthquake influence landward velocity change because of the lack of enough GNSS data. The last major earthquake that occurred near the OXPE station, is a M7.5 earthquake in 1999 (Segou and Parsons, 2018). Considering the time between the two earthquakes, the decay of its postseismic crustal deformation would not significantly influence the results shown in Figure 3.14.

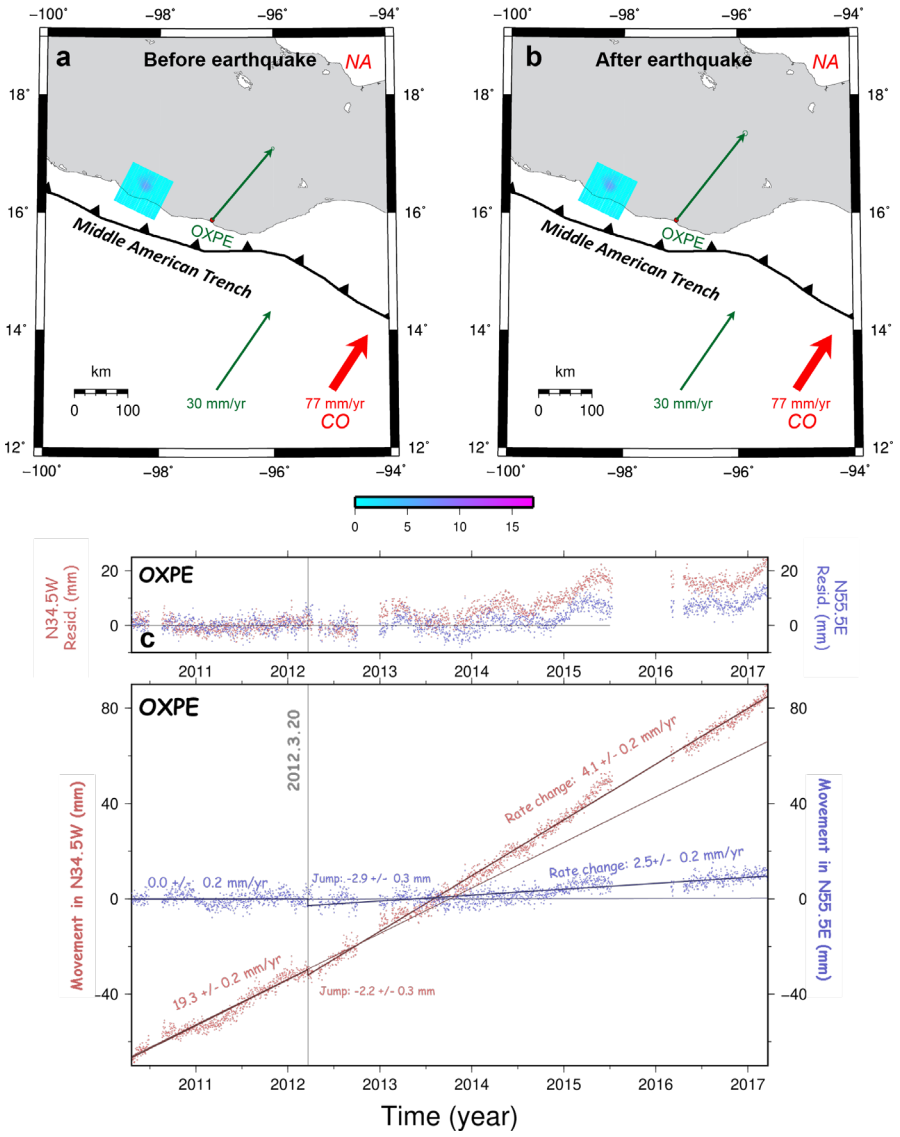

Figure 3.14. Maps and diagram demonstrating the postseismic landward velocity increase for the 2012 Oaxaca earthquake. In (a) and (b), I compare the velocity before and after the 2012 earthquake for the station OXPE showing possible postseismic enhanced coupling. The red arrow represents the Cocos Plate movement. The velocity vectors are all relative to the North American Plate. The time series of the horizontal coordinates of the OXPE station (dark green arrow in a, b) is shown in (c) using the components parallel with (red) or perpendicular to (blue) the subduction direction.

Chapter 4: Discussion

4.1 Overview of the six cases

I reported six cases in four different subduction zones suggesting the post-megathrust occurrence of landward increase of forearc velocity on the segments adjacent along-strike to the ruptured segment. They are not easily explained by conventional interpretations with postseismic processes such as afterslip and local scale viscous relaxation. I first revisited the 2003 Tokachi-oki and the 2011 Tohoku-oki earthquakes in NE Japan reported by Heki and Mitsui (2013). I then studied the 2010 Maule earthquake, Chile, for which Melnick et al. (2017) reported increased landward movements north of the rupture. I also studied the velocity changes associated with the 2014 Iquique earthquake in northern Chile, originally found by Hoffmann et al. (2018). I newly found the signatures for the 2007 Bengkulu earthquake (Southwestern Sumatra), and the 2012 Oaxaca earthquake (Mexico).

The six examples include the two cases, 2011 Tohoku-oki and 2007 Bengkulu earthquakes, where interseismic velocities deviate largely from relative plate subduction directions. Such deviations are due to long-lasting postseismic crustal movements of past earthquake, i.e. 2003 Tokachi-oki and the 2000 Enggano earthquakes, respectively. Even in these cases, the velocity changes nearly align with the plate subduction directions. I also carefully evaluated the leakage of the decaying trenchward postseismic crustal movements of past large nearby

earthquakes into the inferred landward velocity increases.

In addition to landward velocity increase, a trench-parallel velocity change was found after the 2003 Tokachi-oki earthquake (Heki and Mitsui, 2013). Also, in the 2010 Maule earthquake, the changes of the velocities are somewhat deviated counterclockwise from the plate subduction direction (Figure 3.8a). Such changes could be driven by postseismic viscous relaxation.

Vertical velocities may also have changed at stations showing enhanced landward velocities. Because of the larger noises in vertical component, I cannot draw decisive conclusions for them (Figure 2.14). We should revisit the problem after data with enough time span become available in the future.

In addition to the six cases studied here, I looked for similar increase signatures for other megathrusts in various subduction zones. They include the 2004 December Sumatra-Andaman earthquake (M_w 9.2) and the 2005 March Nias earthquake (M_w 8.6) (Figure 1.5). The search was not successful in these cases simply due to the lack of enough time span of pre- and postseismic data from GNSS stations in appropriate places. The movements of the SuGAR stations are well documented by e.g., Feng et al. (2015). Below I summarize the situation in Sumatra.

The three SuGAR stations (PSMK, PTLO, PBAI) in islands to the northwest of Sumatra started working well before the 2004 Sumatra-Andaman earthquake and may have recorded enhanced landward velocities following that event. However, the 2005 March Nias earthquake occurred before we can confirm its signature, and their velocity changed trenchward due to the postseismic movements by the 2005 event. Three SuGAR stations (MSAI, PSKI, BSAT) off the middle Sumatra started operation before 2004, but they were not close enough to the 2005 rupture and did

not show significant post-2005 landward velocity change. It is a pity because it is likely that these two earthquakes caused landward velocity increases in the Sumatra subduction zone. In fact, a series of M_w>7 earthquakes occurred in the segments to the southwest of these two earthquakes (Haridhi et al., 2018) suggesting accelerated interplate strain buildup there.

A similar situation applies for the 2015 Illapel earthquake (M_w 8.3), in central Chile (Figure 1.5). For example, the COPO station is in the region suitable to study increased coupling by the 2015 earthquake, but its observation data are not available after 2015.

4.2 Spatial decay of the enhanced coupling

The enhanced coupling may encourage future failures in the neighboring segments. For example, earthquakes such as the 2015 Illapel earthquake (M_w 8.3) and the 2016 Chiloé earthquake (M_w 7.6), occurred to the north and south of the 2010 Maule earthquake, respectively, may have been triggered by the enhanced coupling caused by the 2010 Maule event (M_w 8.8) (Melnick et al., 2017; Ruiz et al., 2017). To further discuss this issue, it is important to know the spatial and temporal decay of the enhanced coupling.

In Chapter 3, I did not pay much attention to the relationship between amounts of the velocity changes and distances from the ruptured faults. In Figure 4.1, I plot the landward velocity increases as a function of the distance from the center of the fault for the 2003 Tokachi-oki, 2011 Tohoku-oki, and the 2010 Maule earthquakes. For the Tohoku-oki case, postseismic trenchward movements seem to prevail from the rupture area as far to the northeast as ~100 km from the fault edge. According

to the slab acceleration model (Chapter 2.3), this does not mean the absence of slab acceleration there. The acceleration is the largest just beneath the ruptured fault, but it is "hidden" by the oceanward movement of the forearc caused by the afterslip and viscoelastic relaxation.

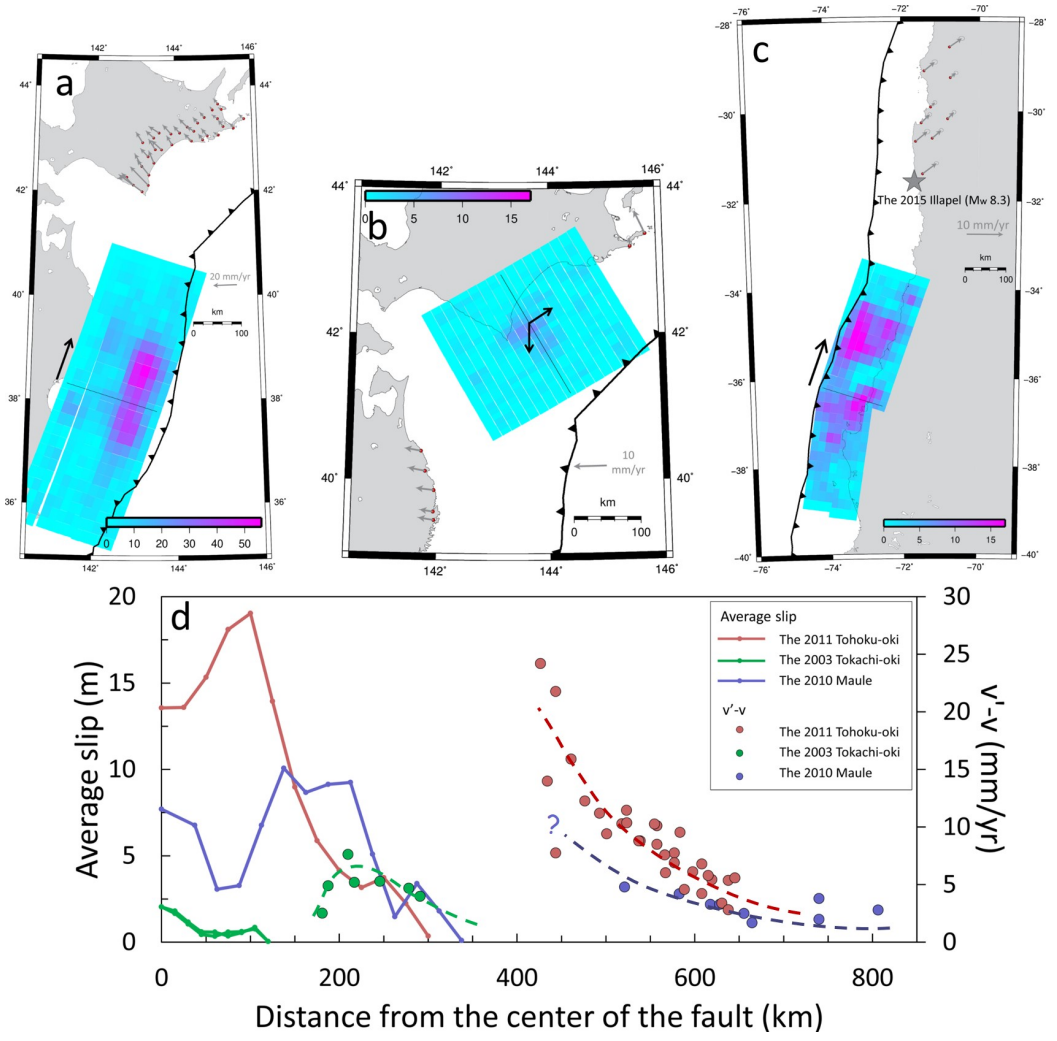

Figure 4.1. Dependence of the increase of landward velocities (v'-v) of forearc stations on the distance from the center of the fault for the 2011 Tohoku-oki, the 2010 Maule, and the 2003 Tokachi-oki earthquakes. The distance was calculated in the direction of fault strike (black arrows), except for the south of the 2003 Tokachi-oki case due to the bending of the trench (d). I included data from ~30 GNSS stations near the Pacific coast of Hokkaido (a), 7 stations near the Pacific coast of NE Japan and Hokkaido (b), and 9 stations near the pacific

coast of central Chile (c). The average slips in both along-strike directions from the fault centers are obtained from the slip models from USGS. Broken curves are hypothetical smooth models.

For the 2011 Tohoku-oki case, the landward velocity changes prevail for stations farther than ~100 km from the fault edge. Such an increase is confirmed to continue as far as ~650 km from the fault center, but it is not clear if it extends beyond that point due to the lack of data. For the 2010 Maule case, I have data only beyond 500 km from the fault center. Probably, the true maximum landward velocity increase for this event would exist somewhere with distance < 500 km. For this earthquake, the data are available as far as 800 km, and the velocity increases seem to decay gradually for distance range 500-800 km. For the 2003 Tokachi-oki case, landward increase appears in the stations closer to the fault, and its maximum occurs only ~100 km from the fault edge. From these three cases, the landward velocity increase seems to extend at least as far as ~1/2 the fault lengths beyond the fault edges.

If such a landward velocity increase causes increased interplate coupling, large earthquakes may be encouraged in future in "affected segments", e.g. the southern Kuril Islands and in central Chile. It would be reasonable to consider that the enhanced interplate coupling to the north of the Maule rupture has triggered the 2015 M_w 8.3 Illapel earthquake (see Figure 4.1c for position).

D'acquisto et al. (2020) used the velocity-driven 3D mechanical finite element models to quantify and analyze the deformation that produces landward motion by the viscous relaxation of the mantle wedge and the deep afterslip. Their results show increased postseismic landward motion of up to ~6.1 mm/yr at (trench-parallel) distances >450 km from the middle of the ruptured asperity. They conclude that enhanced landward motion is generated by in-plane elastic bending of the

overriding plate and mantle wedge in response to oceanward motion of lithosphere around the rupture zones. Their results are also consistent with the observations in Central Chile. Melnick et al. (2017) used a large-scale three-dimensional thermomechanical model to simulate viscoelastic relaxation of the mantle to explain continental-scale velocity changes. Their model also reproduces the observed landward velocity increase.

4.3 Temporal decay of the enhanced coupling

Another important aspect is the temporal decay. According to the slab acceleration model (Chapter 2.3), The enhanced coupling decays as the interplate coupling *F*c returns to the pre-earthquake state. Such a recovery time may depend on the earthquake magnitude, i.e. the larger the magnitude, the longer the period for the recovery of interplate coupling. In the time series of trench-normal movements (Figures in Chapter 3), temporal decays are not very evident, i.e. landward movements show simple increased linear trends without notable curvatures. For the 2010 Maule, the time series has a curvature immediately after the earthquake, but we do not see a curvature after the data gap (Figure 3.8). Here I confirm this numerically.

I set up the moving 1-year time period for the linear regression to see possible temporal change in slope (Figure 4.2). This analysis shows that velocity changes are either higher or lower in the first few years due to postseismic transients. Gray arrows in Figure 4.2 indicate rough length of significant postseismic transients given in past literatures. After these years, the velocity changes seem to remain stable.

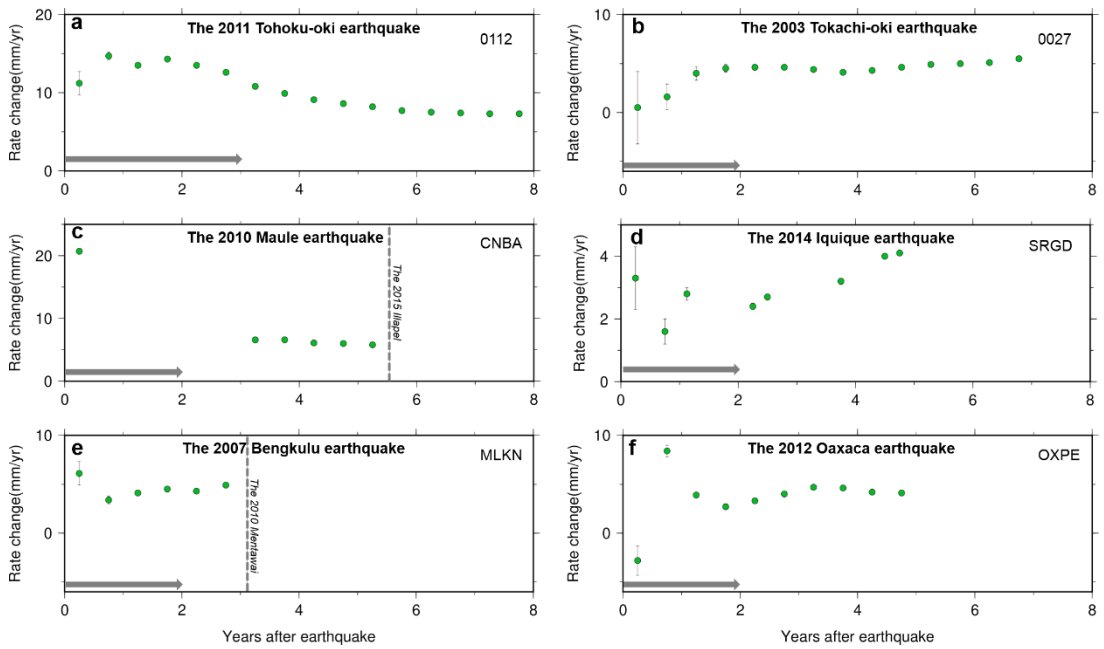

Figure 4.2 Interseismic landward velocity change estimated within moving 1-year time windows (a-f). Horizontal coordinates of the green circles show the centers of the time windows. Gray arrows represent the duration of postseismic decay based on previous studies. In (c) and (e), I exclude data after significant earthquakes occurred nearby (black dashed line). After periods of instability, the rate becomes stationary for subsequent years. In the two Chilean cases (c, d), data gaps make the rate change unstable.

Figure 4.3 presents an example of a long-time continuous distance changes of a baseline in Hokkaido, connecting the 0010 and 0102 stations. This baseline is approximately in the direction of the Pacific Plate subduction and the data covers from 1996 to 2020. The distance gets shorter as the interseismic compressive strain accumulates. This is disrupted by two interplate earthquakes in 2003 Tokachi-oki (M_w 8.3) earthquake and the 2004 Kushiro-oki (M_w 7.0) earthquake (Tanioka and Katsumata, 2007). After a few years of oceanward movement of 0010 (increase of the distance), distance resumed to decrease. The rate before and after these two earthquakes are 29.3 mm/yr and 27.5 mm/yr, respectively. After the 2011 Tohoku-oki earthquake, this rate increased to 32.9 mm/yr due to the enhanced landward movement of 0010.

An important feature in Figure 4.3 is that the increased landward velocity does not seem to decay in time up to now. It shows temporary enhanced shortening for two years just like the case in the 2010 Maule earthquake (Figure 3.8). After that, the baseline continues to contract at a steady increased rate up to now. Yamagiwa et al. (2015) showed that afterslip has mostly decayed in 2.5 years, while viscous relaxation continues over a longer time with a time constant of ~10 years. The increased landward velocity as seen in Figure 4.3 would have a longer time constant. As mentioned in Heki and Mitsui (2013), such an apparent lack of decay is a striking feature of this phenomenon, and we need observations over longer time windows to understand the process.

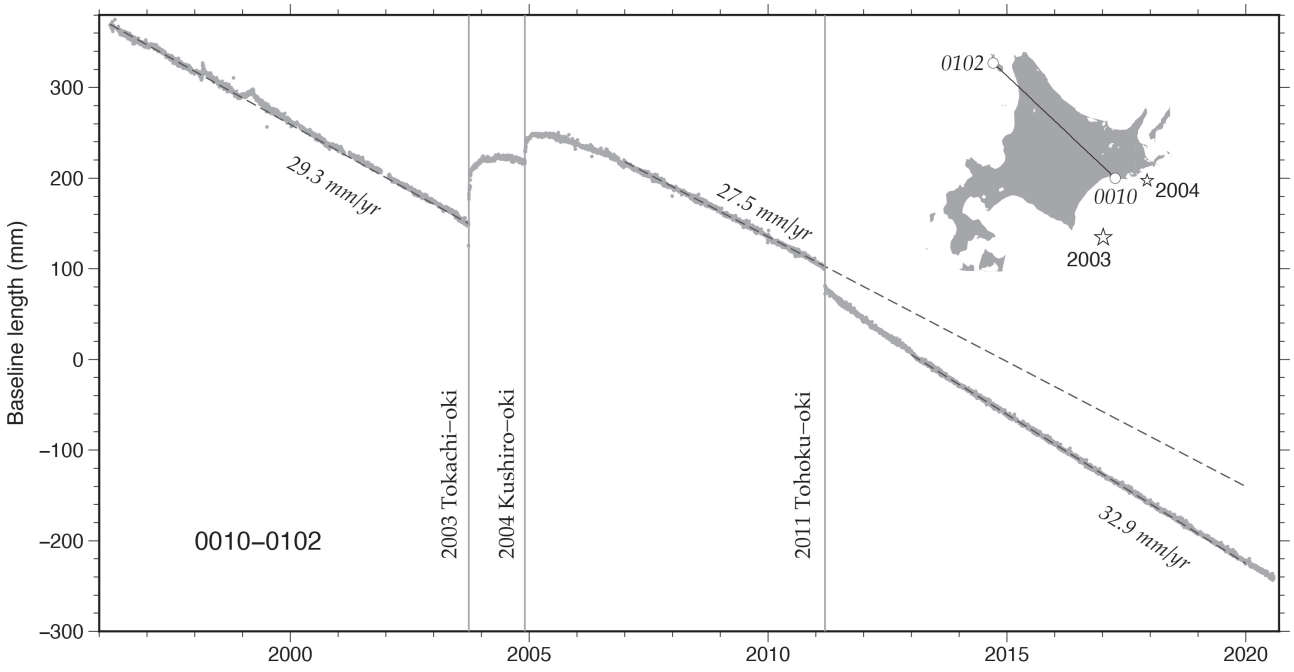

Figure 4.3. Time series of the distance between two GNSS stations in Hokkaido, Japan, showing little temporal decay of the landward increased velocity started after the 2011 Tohoku-oki earthquake. The inset map shows the position of the two GNSS stations, and the epicenters of the two earthquakes, 2003 Tokachi-oki (M_w 8.3) and 2004 Kushiro-oki (M_w 7.0) earthquakes. The three rates attached to the dashed lines are average rate for periods 1996.0-2003.74 (29.3 mm/yr), 2007.0-2011.19 (27.5 mm/yr), and 2013.0-now (32.9 mm/yr).

4.4 Forearc station velocities and slab velocities

Heki and Mitsui (2013) hypothesized that postseismic enhancements of the interplate coupling may reflect the accelerated rate of the slab subduction u'-u in response to the modified balance of forces acting on the subducting slab (Figure 2.15). Actually, what is observed is the change in velocity of forearc GNSS stations v'-v, and it is necessary to convert v'-v to u'-u. Generally, v becomes larger if interplate coupling is stronger, but v never exceeds u. I here inferred the ratio v/u ($0 \leq v/u < 1$) by comparing the observed interseismic velocity of the GNSS station and the subduction speed calculated by the MORVEL model (Argus et al., 2011).

For example, in the Maule earthquake, the velocity of the CNBA station observed before (v_{CNBA}) and after (v'_{CNBA}) the earthquake, might be related to the hypothetical slab acceleration u'_{Nazca}-u_{Nazca}. This relationship can be formulated using the subduction speed of the Nazca Plate v_{Nazca} relative to the South American Plate at the Chile Trench, as follows,

$$u'_{Nazca}-u_{Nazca} = (v_{Nazca} / v_{CNBA}) \times (v'_{CNBA} - v_{CNBA}) \quad (6)$$

This conversion is applied to all cases except the Tohoku-oki and the Bengkulu earthquakes. In these two cases, postseismic movements of nearby earthquakes in recent past still influenced v and v' (Figures 3.2 and 3.13), i.e. the 2003 Tokachi-oki and the 2000 Enggano earthquakes, respectively. In Japan, I used the interseismic velocities before the earlier earthquake (i.e. before 2003). For the MLKN station, the data are not available before 2000, and so I used the average of interseismic velocities in 2000-2007 of the five stations above the 2007 rupture (Figure 3.13a) to infer v_{MLKN}.

By such calculations, the acceleration of the slab subduction for the six cases became, 22.0 mm/yr (2011 Tohoku-oki), 8.4 mm/yr (2003 Tokachi-oki), 10.4 mm/yr (2010 Maule), 6.6 mm/yr (2014 Iquique), 8.5 mm/yr (2007 Bengkulu), and 10.1 mm/yr (2012 Oaxaca). For the first four cases, I have data from multiple stations and calculated the uncertainties in such velocity changes.

4.5 Comparison of the data with the slab acceleration model (Heki and Mitsui, 2013)

Here I examine the slab acceleration model by Heki and Mitsui (2013) by comparing the acceleration of the subduction speed inferred in the previous section with the model predictions. The equation (2) suggests that the decrease in the coupling F_c'-F_c determines the slab acceleration u'-u. The acceleration would hence depend on M_w, because a larger earthquake would cause larger F_c'-F_c. Figure 4.4 compares de-trended time series of trench-normal movements of the forearc stations for the six cases studied here, using a unified vertical axis. The figure shows that the acceleration is larger for a case with a larger M_w, and the most significant velocity increase appeared following the M_w 9.0 2011 Tohoku-oki earthquake.

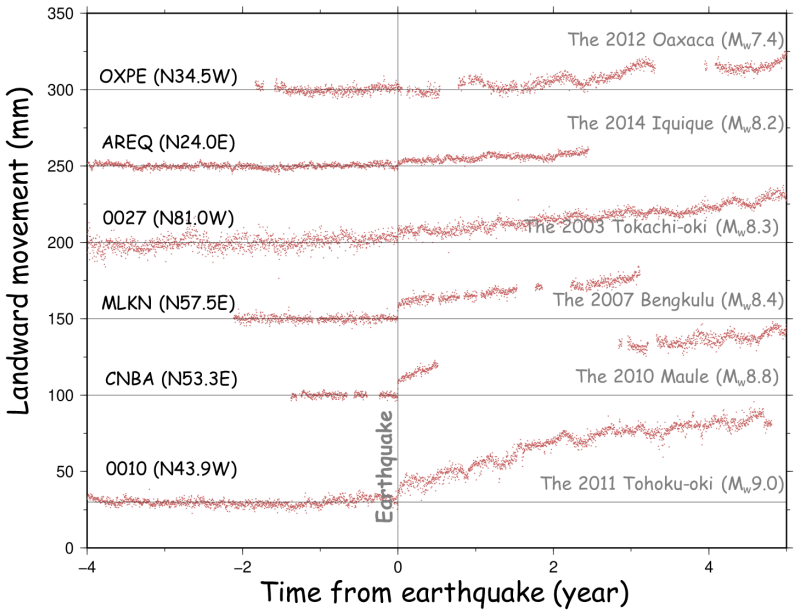

Figure 4.4. Comparison of the increased landward velocities of GNSS stations following six megathrust earthquakes studied here. I removed linear trends before the earthquakes to facilitate the comparison of postseismic velocity increases for the six cases. The vertical grey line, used as the origin, indicates the earthquake occurrence times. The station names and the azimuths of the displayed movements are given to the left, and the earthquake names and their M_w are given to the right.

The surface velocity changes v'-v in Figure 4.4 are converted to slab velocity changes u'-u, as discussed in the previous section. Figure 4.5a compares u'-u in addition to v'-v as a function of M_w. There, smaller symbols show v'-v and u'-u at individual stations for earthquakes where multiple stations are available. We can see that a larger earthquake brings a larger change, both forearc (v) and slab (u) velocities.

As discussed in Section 3, the loss of coupling $Fc'-Fc$ would be proportional to the coseismic slip averaged over the fault s_{av} if we fix other parameters. Figure 4.5b

compares the slab acceleration with the average slip s_{av}, calculated using the slip data of USGS as shown in Figures 3.2, 3.5, 3.8, 3.10, 3.13, and 3.14. The acceleration seems to show good correlation with s_{av} considering that the value for the 2010 Maule earthquake is probably an underestimate (Figure 4.1d). However, it is not very clear if the two quantities are proportional considering the four earthquakes with $M_w \leq 8.5$ are clustered at a down-left corner of the figure and do not contribute to the evaluation of the linearity.

Table 4.1. Slab length for individual earthquake.

No	Earthquake	Slab length (km)	W (km)	Source
1	The 2011 Tohoku-oki (M_w 9.0)	1,075	2,150	Deal and Nolet (1999)
2	The 2010 Maule (M_w 8.8)	1,100	2,200	Pesicek, et al. (2012)
3	The 2003 Tokachi-oki (M_w 8.3)	1,075	2,150	Deal and Nolet (1999)
4	The 2007 Bengkulu (M_w 8.4)	700	1,400	Hafkenscheid, et al. (2001)
5	The 2014 Iquique (M_w 8.2)	1,100	2,200	Scire, et al. (2017)
6	The 2012 Oaxaca (M_w 7.4)	900	1,800	Husker and Davis (2009)

1461 **Table 4.1.** Average slip for individual earthquake.

No.	Earthquake	Average slip (m)	Source
1	The 2011 Tohoku-oki (M_w 9.0)	7.97	https://earthquake.usgs.gov/earthquakes/eventpage/official20110311054624120_30/finite-fault
2	The 2010 Maule (M_w 8.8)	5.14	https://earthquake.usgs.gov/earthquakes/eventpage/usp000c8kv/finite-fault
3	The 2003 Tokachi-oki (M_w 8.3)	0.80	https://earthquake.usgs.gov/earthquakes/eventpage/official20100227063411530_30/finite-fault
4	The 2007 Bengkulu (M_w 8.4)	0.80	https://earthquake.usgs.gov/earthquakes/eventpage/usc000nzvd/finite-fault
5	The 2014 Iquique (M_w 8.2)	0.77	https://earthquake.usgs.gov/earthquakes/eventpage/official20070912111026830_34/finite-fault
6	The 2012 Oaxaca (M_w 7.4)	0.63	https://earthquake.usgs.gov/earthquakes/eventpage/usp000jghj/finite-fault

1462

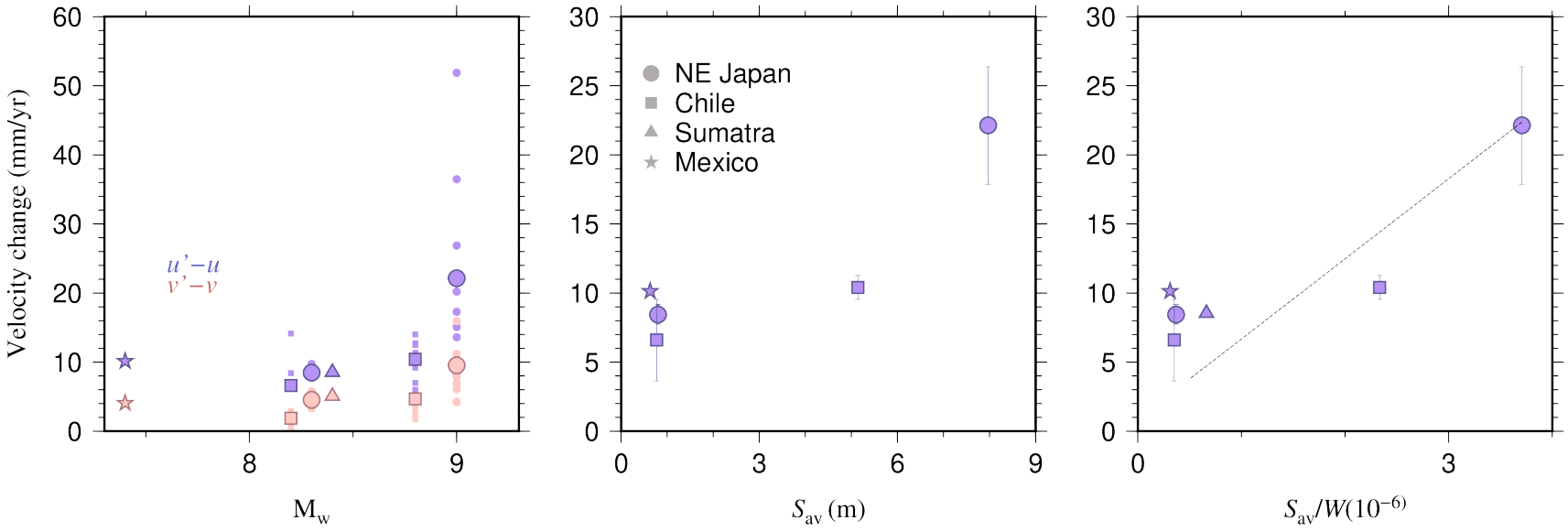

Figure 4.5. (a) Comparison of the forearc acceleration, *v'-v*, and the slab acceleration, *u'-u*, for six different megathrust earthquakes with M_w7.4-9.0. Different symbols indicate different subduction zones. Smaller symbols show values at individual stations for the cases with multiple available stations. (b) M_w is replaced with the slips averaged over the faults (s_{av}) in (b) and with s_{av}/W, where W corresponds to the length of the slab surface (see eq. 5). Error bars show the standard deviation of the averages of these velocity changes.

Equation (5) also suggests that the slab acceleration is inversely proportional to W, the length the slab surface. Here I assumed that W is twice as long as the slab lengths inferred from seismic tomography studies and compare u'-u and s_{av}/W in Figure 4.5c. Here I use the information on the lengths W, twice as long as the slab length, i.e. 1,075 km for NE Japan (Deal and Nolet, 1999), 1,100 km for Chile (Scire et al., 2017), 700 km for Sumatra (Hafkenscheid et al., 2001), and 900 km for Mexico (Husker and Davis, 2009). Considering that the value for the Maule event is underestimated, data in Figure 4.5c may suggest linearity. Nevertheless, they are not enough to provide a firm support to the slab acceleration model by Heki and Mitsui (2013), considering that 4 smaller earthquakes are clustered and do not fully contribute to the evaluation of the linearity. After all, the data obtained in this study support the model, but they are not strong enough to rule out other possibilities.

The dashed line in Figure 4.5c has the slope of 6.1×10^3 m yr^{-1}, which corresponds to 1.93×10^{-4} m sec^{-1}. This slope is equivalent to $\nu d/\mu$ in equation (5) as the average of the four subduction zones studied here (although the 2011 Tohoku-oki and the 2010 Maule data mainly contribute to the determination of this slope). If I put 50 GPa and 10^{17} Pa·s into ν and μ, I get 380 meters for d, the thickness of the low-viscosity layer at the slab surface.

Chapter 5: Change in Seismicity

5.1 Previous Studies

Early studies indicated that various properties, including the occurrence of megathrust earthquakes, of subduction zones are governed by the velocity and the age of the subducting oceanic plates (Uyeda and Kanamori, 1979; Ruff and Kanamori, 1980). Subsequent studies also showed that the orientation of the stress fields and the degree of development of accretionary prisms may play a role in determining the magnitudes of the interplate earthquakes (Heuret et al., 2012). The relationship between the seismicity rate and the plate convergence velocities has been investigated by several previous studies, such as Bird et al. (2009) and Singh et al. (1992).

Peng et al. (2012) claimed that a major earthquake can increase seismicity based on seismicity data in Southwestern China following the 2004 Sumatra Earthquake. There, the increase of seismic activity was mostly coming from shallow events. This case reflects a change in stress rather than increased interplate velocity. In Japan, the occurrence rates of small repeating earthquakes increased following the 2011 Tohoku-oki earthquake (Uchida et al., 2016), which provides a clear evidence of the accelerated slab subduction beneath the Kanto District.

Ide (2013) compared seismicity in worldwide subduction zones and confirmed that relative plate velocity correlates positively with the seismicity rate. In this study, I expect that the increase of landward velocity in the regions of

enhanced coupling may correlate positively with the background seismicity rate. In this chapter, I show the results of the studies on the seismicity changes in such regions.

5.2 Seismicity data

Generally speaking, earthquakes can hit any region on earth at any time. However, very large earthquakes tend to occur along convergent plate margins, earthquakes and tsunami constitute distinctive hazards for those living in such regions. About 81% of the worldwide massive earthquakes occur along the rim of the Pacific Ocean, the region well known as the circum-Pacific seismic belt. Seismic activity in this region indicates significant heterogeneity, such as giant earthquakes, medium and small-scale earthquakes, tsunami earthquakes, and slow/silent earthquakes, aside from microearthquake activities. The 40,000-kilometer horseshoe-shaped belt extends from New Zealand, northward through the Southwest Pacific island group, New Guinea, Eastern Indonesia, the Philippine Islands, the Japanese Islands, the Kuril Islands, Aleutian Islands, Southern Alaska, Cascadia, the West Coast of United States, southward through Mexico, Central America, along West Coast of South America, and ends in southern Chile.

About 17 % of the world's massive earthquakes occur in the Alpine belt, the second prominent belt. This belt emerges from the Atlantic, the Mediterranean, the Himalayas, Sumatra, and ends in Java, Indonesia. The third important belt is located along the submerged convergent plate margins, such as the Mid-Atlantic Ridge and the East Pacific Rise. Outside these three belts, a small number of earthquakes are spread in many regions around the world (Figure 8.1).

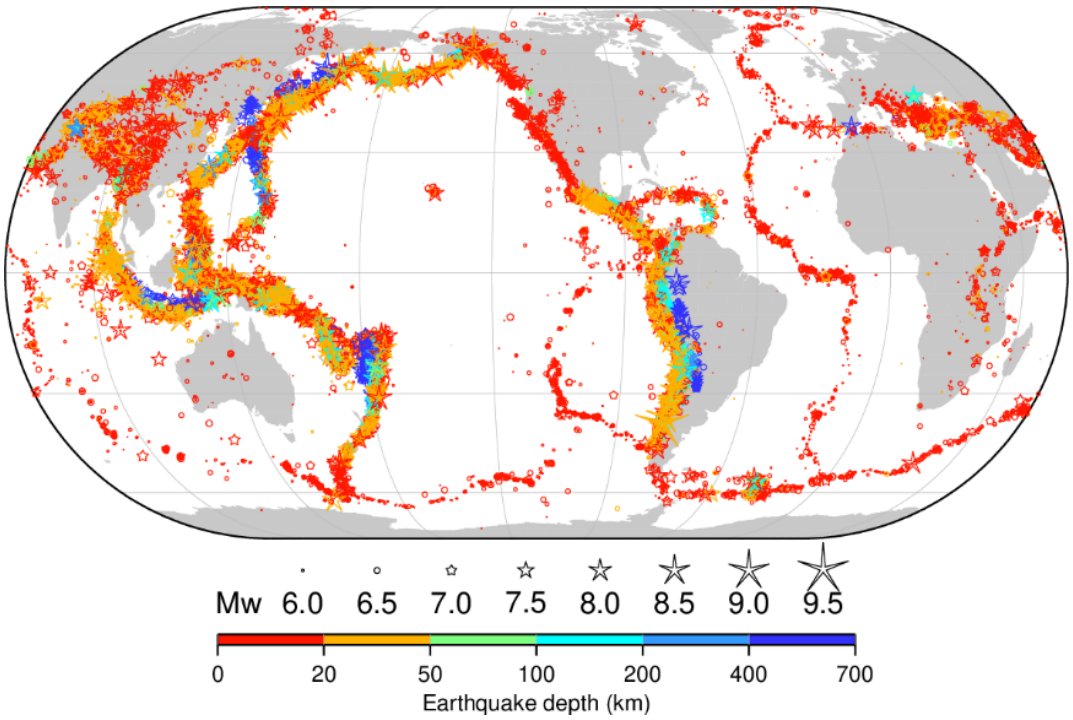

Figure 8.1. Distribution of earthquake around the globe (http://ftp.isc.ac.uk/iscgem/overview.php). They occur mostly within narrow zones of plate boundaries.

To investigate the mechanism of landward velocity change, seismicity change would provide important information. Uchida et al. (2016) found the accelerated interplate creep rates observed as the cumulative slip of small repeating earthquakes and inferred that the subducting slab beneath the Kanto area accelerated following the 2011 Tohoku-oki earthquake. This would serve as a direct evidence for the accelerated stab subduction.

The waveform data are indispensable to study such small repeating earthquakes. They are not always available in the regions studied here. In Japan, the waveform data are not complete for the period before 1993 because of insufficient dynamic range of the observations and unstable recording systems. Moreover, the waveform data are not available for the period within three days following the 2011 Tohoku-oki earthquake because of the system problems, e.g. electric power and telemetry link failures by the earthquake (Uchida and Matsuzawa, 2013).

In this study I do not analyze the repeating earthquake but only studied the increase of seismicity in two regions, Japan and Chile, where both GNSS and seismometer stations were available. Here, I consider the earthquakes that occurred in the same area indicates the rate in shear stress buildup in the plate boundary region. The increased seismicity would possibly reflect the enhanced interplate coupling.

I analyzed an earthquake catalog created by International Seismological Center (ISC). The ISC Bulletin is a complete source of earthquake locations and magnitude at the global scale, which accommodates raw data, hypocenter solutions, and other earthquake data compiled by ~150 agencies worldwide. Until 2019, the ISC Bulletin has included more than 7.6 million seismic events from any sources including natural earthquakes, chemical and nuclear explosions, mine blasts, and other kinds of events generating seismic waves.

It requires tremendous efforts to ensure seismic events at stations from various agencies are generated from actual seismic events. Therefore, when the ISC received data from stations recording a seismic event, several measures are taken. At the beginning, the ISC collects and groups all parametric data into specific seismic events. Once the event created, it can be accessed by anyone through the online ISC bulletin. After that, the station readings and hypocenter solutions with magnitude of more than 3.5 will be examined manually by ISC data analysis staffs. If all conditions are met, the ISC will integrate all the existing phase arrival times and amplitude measurements to recompute location and magnitude (currently only surface wave magnitude M_S and body wave magnitude m_b).

Currently, 65 agencies in the ISC bulletin have reported in the past or are still reporting the source mechanism solution to the ISC. Here, the word of “source

mechanism" means a moment tensor solution of a pure double couple mechanism at a point source. Besides, the ISC also has started to compute its focal mechanism by using first motion polarities both from reports from various agencies and from the data picked up automatically from waveform data. However, due to different methods adopted by individual agencies, heterogeneity in the solutions of the source mechanisms is inevitable.

In this study, I ignored the surface wave magnitude and the moment magnitude. Instead, I used the earthquake list with the body wave magnitude m_b because ISC has been determining and reporting them since 1964 continuously. It was possible to obtain necessary data for regions and times I analyzed the GNSS data in this research.

5.3 Seismicity declustering

I compare the seismicity in the segment showing enhanced coupling before and after the earthquakes. Here, I used data from the International Seismological Centre catalog (www.isc.ac.uk) with focal depths ≤ 60 km. Comparing seismicity in different periods is quite challenging because the occurrences of major earthquakes and their aftershocks often impact the seismicity pattern. I used the target events with body wave magnitude (m_b) larger than a threshold in the period from 2000/01/01 to 2017/12/1 and in the region 41.5° to 45°N, 143° to 149°E for the Tohoku-oki case and 2000/01/01 to 2017/12/1 and in the region 33° to 27°S, 74° to 70°W for the Maule case (Figure 8.2 and 8.3).

Before doing further analysis, it is important to check the magnitude completeness (M_c) of the earthquake catalog. By applying the method by Wiemer and Wyss (2000), I plot the cumulative number of earthquakes versus magnitude to

estimate M_c using ZMAP (https://github.com/CelsoReyes/zmap7). After applying the method to the ISC catalog, I found M_c are 3.8 and 4.2 for the ISC catalog in the Tohoku-oki and the Maule cases, respectively. Therefore, I used earthquakes with $m_b \geq 3.8$, and ≥ 4.2 for declustering process for the two cases. I used 1813 and 2066 events for the two cases, respectively (Figure 8.2 and 8.3).

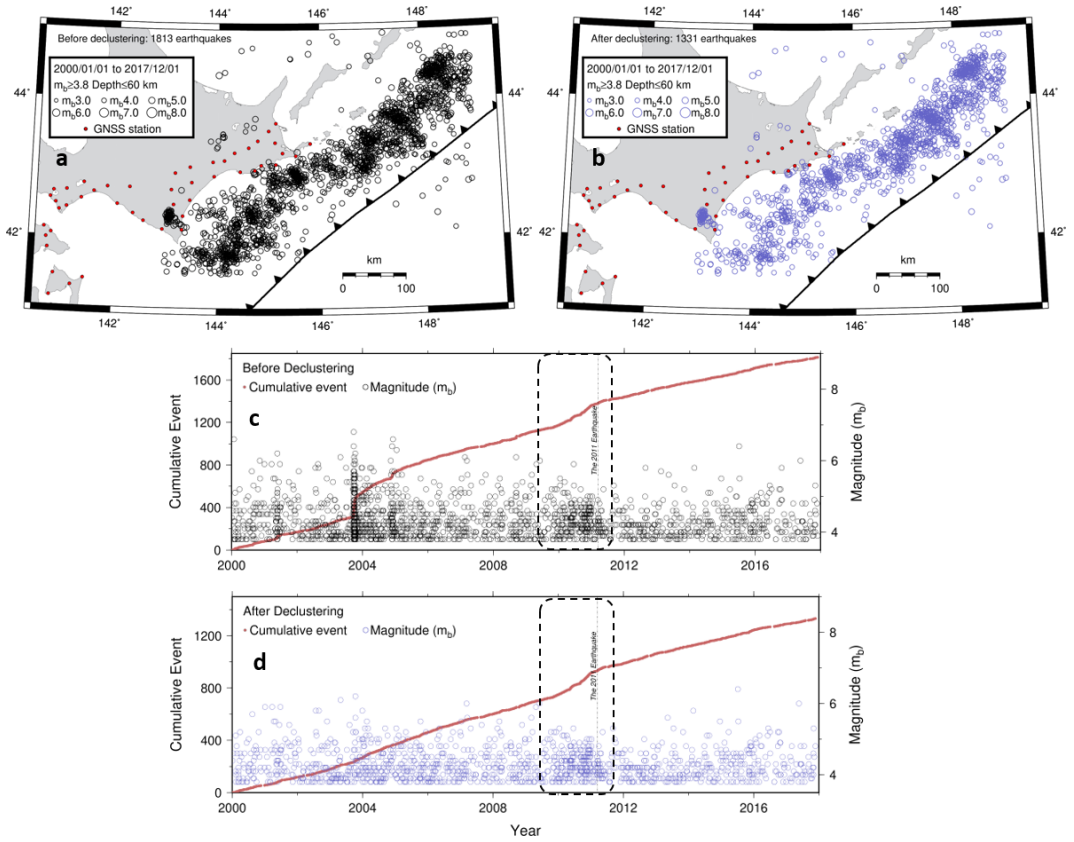

Figure 8.2. Seismicity in the near the Pacific coast region in the eastern Hokkaido before (a, c) and after (b, d) applying the ETAS declustering. The original 1,813 events decreased to 1,331 events by the declustering. The dashed area indicates the period of the increase of background seismicity due to unknown mechanisms. I excluded this period in the discussion.

To compare seismicity changes by large earthquakes, I removed clustered earthquakes such as swarms and aftershocks from the ISC catalog using a stochastic declustering method developed by Zhuang et al. (2004). This method discriminates seismicity into the background events and the triggered events based on an

Epidemic-Type Aftershock Sequence (ETAS) model (Ogata, 1988). I used a computer code for the space-time ETAS model and stochastic declustering from http://bemlar.ism.ac.jp/zhuang/software. Parameters estimated from fitting the ETAS models to the ISC catalog are listed in Table 8.1. After declustering process, 1,331 and 761 events remained as background events in the near east coast Hokkaido and near the Pacific coast of central Chile (Figure 8.2 and 8.3), respectively. I used these background events for further analyses.

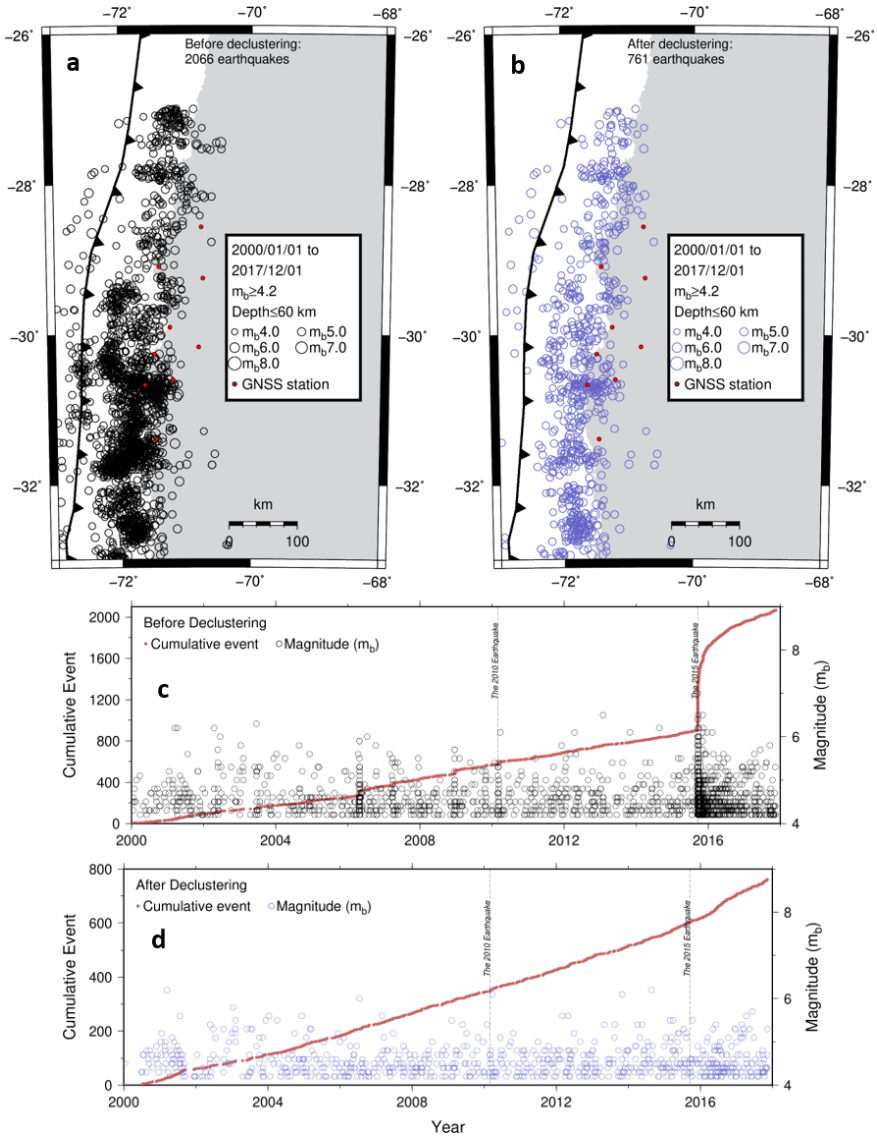

Figure 8.3. Seismicity in the near Pacific coast of central Chile before (a, c) and after (b, d) the application of the ETAS declustering. There are 2,066 events

before declustering, and 761 events remained after declustering.

Such a landward velocity change may increase the trench-normal shortening rate and accelerate shear stress buildup at the plate boundary in the neighboring segments of the megathrust ruptures. To confirm this, I compared seismicity before and after the megathrust earthquakes in those segments (Figures 8.2, 8.3, 8.4).

Increased seismicity right after the 2011 Tohoku-oki in the Pacific coast of eastern Hokkaido was difficult to confirm. This is due to the temporary increase of seismicity that started a few years before the 2011 earthquake (region within dashed square in Figure 8.2c, d). This increase is not due to aftershocks because significant earthquakes did not occur in this period (Figure 8.2). This increase is considered an artifact (K. Katsumata personal comm. on 2020/9/11) with possible origins including the change in detection capability (Habermann, 1991), natural change in background seismicity (background fluctuation), and the ETAS problem itself (Lombardi et al., 2010). Here I shifted the periods before and after the 2011 earthquake to exclude this period in Figure 8.4c (shown as the grey region). This let us see the increase in seismicity possibly caused by the enhanced coupling associated with the 2011 Tohoku-oki earthquake (Figure 8.4c).

Table 8.1. List of parameters for applying the ETAS models to the ISC catalog.

Area	**Event**	**μ** events/day	**A** events/day	**C** day	**α** $\mathbf{M^{-1}}$	**p**	**γ**
41.5-45N, 143-149E	The 2011 Tohoku-oki	0.97	0.14	0.02	1.77	1.07	0.85

33-27S, 74-70W	The 2010 Maule	0.96	0.50	0.02	1.31	1.11	0.70

Figure 8.4d shows the increase of seismicity from the two- and four-year periods before and after the 2010 Maule earthquake, respectively, within the rectangles shown in Figure 8.4b. There I show the number of earthquakes, and we can see an increase in seismicity of ~10%, which is smaller than the rate of increase in the landward velocity (~20% in CNBA, see Figure 3.8). In both the Japanese and Chilean cases, the rates of the seismicity increases are not so high as those in the rates of the increased landward velocities.

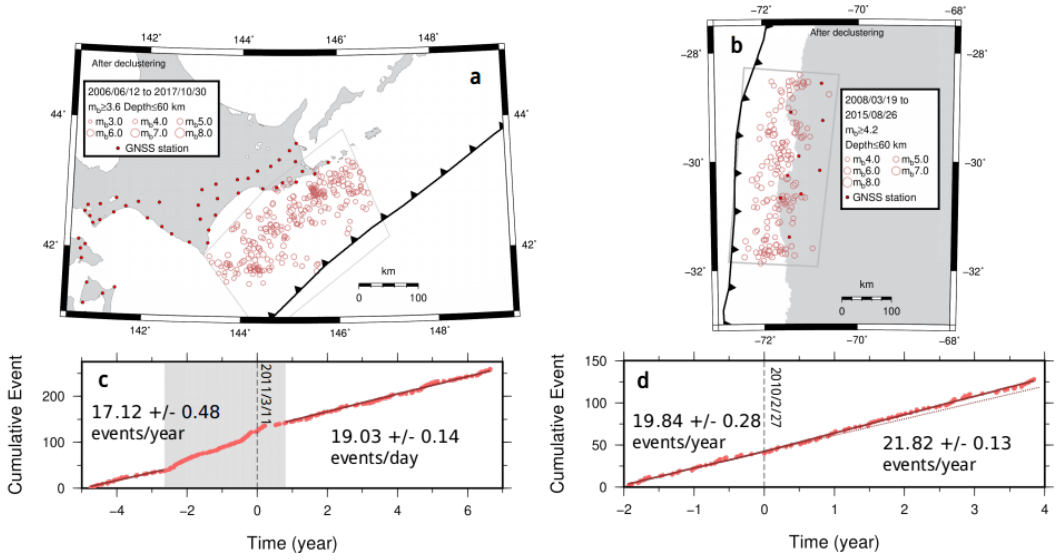

Figure 8.4. The change of seismicity in the Pacific coast of eastern Hokkaido (a, c) and near the Pacific coast of central Chile (b, d) associated with the 2011 Tohoku-oki and the 2010 Maule earthquakes, respectively. The vertical dashed lines (c, d) indicate the earthquake occurrence times. I used the target in the period from 2006/06/12 to 2017/10/30 for the Tohoku-oki case and 2008/03/26 to 2015/08/26 for the Maule case. Gray zone (c) shows the period of the increase of background seismicity due to unknown mechanisms. The red lines in (c) and (d) indicates the best-fit lines for the seismicity rates before and after these earthquakes.

Chapter 6: Conclusion

The concept of the seismic cycle develops quite dynamically through time. It began as a simple model with a constant strain accumulation and regular recurrences of interplate earthquakes. Subsequently, space geodetic observations revealed the existence of transient postseismic processes such as afterslip and viscous relaxation as an additional component in this cycle. Past researches further added a brand-new stage following a massive earthquake in a subduction zone. This new stage is characterized by the accelerated interseismic stain buildup in segment adjacent along-strike to the ruptured segments.

I compiled GNSS data showing increased landward velocities that occurred in segments adjacent along-strike to six recent megathrust earthquakes in four different subduction zones (Figure 1.5). The results presented here confirmed previous studies for the 2003 Tokachi-oki (Heki and Mitsui, 2013), the 2010 Maule (Melnick et al., 2017), and the 2014 Iquique (Hoffmann et al., 2018) earthquakes. I also updated the case of the 2011 Tohoku-oki earthquake, studied briefly in Heki and Mitsui (2013), using GNSS data over a longer time span. I found similar landward increase of velocity signatures for three more earthquakes in Sumatra, Chile, and Mexico subduction zones.

From the three cases, i.e. the 2003 Tokachi-oki, the 2011 Tohoku-oki and the 2010 Maule earthquakes, where multiple GNSS stations were available from various distances from the faults, I studied spatial extents of the phenomenon. There I found that the landward velocity change extends along-strike to distances comparable to the ruptured fault length (400-500 km) from the fault center (i.e.

extending by a half of the fault length beyond the fault edge) (Figure 4.1d). Temporal decay was not clear suggesting much longer time constants of the phenomenon than known postseismic processes such as afterslip and viscous relaxation.

The velocity change showed a positive correlation with M_w and seems to scale with the average slip. This is consistent with the hypothetical slab acceleration model by Heki and Mitsui (2013) but does not rule out other possibilities. Such increased landward velocity would enhance stress accumulation rate in adjacent segments, encouraging future earthquakes in such segments, e.g. the eastern Hokkaido.

In Chapter 5, I investigated the seismicity rate changes following the two largest earthquakes showing the increased landward velocities. I used data from the ISC bulletin and applied the ETAS declustering method to discriminate seismicity into the background events and the triggered events. The background seismicity after the 2011 Tohoku-oki in the Pacific coast of eastern Hokkaido increased from 17.1 ± 0.5 events/year to 19.0 ± 0.1 events/year. In Chile, the background seismicity rate increased from 19.8 ± 0.3 events/year to 21.8 ± 0.1 events/year after the 2010 Maule earthquake. These results show a moderate increase in seismic activities. However, the ratio of the increase to the original rate is not so high as those of the landward velocity increases.

The contents of this thesis have been published in Tectonophysics:

Yuzariyadi, M., and Heki, K., 2021. Enhancement of interplate coupling in adjacent segments after recent megathrust earthquakes. Tectonophysics, 801, 228719. https://doi.org/10.1016/j.tecto.2021.228719.

References

Abercrombie, R.E., Antolik, M. and G. Ekström., 2003. The June 2000 Mw7.9 earthquakes south of Sumatra: Deformation in the India-Australia Plate. J. Geophys. Res. Solid Earth 108, ESE 6-1-ESE 6-16, doi:10.1029/2001JB000674.

Abidin, H.Z., Susilo, S., Meilano, I., Subarya, C., Prijatna, K., Syafi'I, M.A., Hendrayana., Effendi, J., Sukmayadi, D., 2016. On the development and implementation of a semi-dynamic datum for Indonesia. C. Rizos, P. Willis (eds), *IAG 150 Years*, International Association of Geodesy Symposea 143, doi: 10.1007/1345_2015_83.

Anderson, D.L., 1975. Accelerated plate tectonics. Science, 187, 1077-1079

Ardika, M., Meilano, I., and Gunawan, E., 2015. Postseismic Deformation Parameters of the 2010 M7.8 Mentawai, Indonesia, Earthquake Inferred from Continous GPS observations. Asian J. earth Sci., 8(4): 127-133, doi: 10.3923/ajes.2015.127.133.

Argus, D.F., Gordon, R.G. and DeMets, C., 2011. Geologically current motion of 56 plates relative to the no-net-rotation reference frame, Geochem. Geophys. Geosyst. 12, doi:10.1029/2011GC003751.

Atwater, T., and Stock, J.M., 1998. Pacific–North America plate tectonics of the Neogene Southwestern United States: an update. International Geology Review, 40 (5), 375–402.

Bird, P., Kagan, Y. Y., Jackson, D. D., Schoenberg, F. P. and Werner, M. J., 2009. Linear and nonlinear relations between relative plate velocity and seismicity. Bull. Seismol. Soc. Am. 99, 3097–3113, doi: 10.1785/0120090082.

Blewitt, G., Hammond, W. C., and Kreemer, C., 2018. Harnessing the GPS data explosion for interdisciplinary science. EOS, 99, doi: 10.1029/2018EO104623.

Broerse, T. (2012): Megathrust Earthquakes: Study of Fault Slip and Stress Relaxation Using Satellite Gravity Observations. PhD Thesis, Delft University of Technology, ISBN 9789461862822

Bürgmann, R., Segall, P., Lisowski, M., and Svarc, J., 1997. Postseismic strain following the 1989 Loma Prieta earthquake from GPS and Leveling measurements. J. Geophys. Res., 102, B3, 4933-4955.

Cande, S.C., and Leslie, R.B., 1989. Late Cenozoic Tectonics of the Southern Chile Trench. Journal of Geophysical Research Atmospheres, 91, B1, doi: 10.1029/JB091iB01p00471.

Choe, H., and Dyment, J., 2020. Fading magnetic anomalies, thermal structure and earthquakes in the Japan Trench. Geology, 48, 278–282, doi: 10.1130/G46842.1.

Courboulex, F., Singh, S.K., Pacheco, J.F., and Ammon, C.J., 1997. The 1995 Colima-Jalisco, Mexico, earthquake (Mw 8): A study of rupture process. Geophys. Res. Lett. 24(8): 1019-1022 doi:10.1029/97GL00945.

Curray, J. R., 1989. The Sunda Arc: A Model for Oblique Plate Convergence. Netherlands Journal of Sea Research, 24 (2/3), 131-140.

Deal, M.M., and Nolet, G., 1999. Slab temperature and thickness from seismic tomography2. Izu-Bonin, Japan, and Kuril subduction zones. J. Geophys. Res. 104(12) 28803-28812.

D'Acquisto, M., Herman, M., and Govers, R., 2020. On the cause of enhanced landward motion of the overriding plate after a major subduction earthquake. paper presented at the European Geophysical Union General Assembly, May. 4, 2020.

Einarsson, I., Hoechner, A., Wang, R., and Kusche, J., 2010. Gravity Changes Due to the Sumatra-Andaman and Nias Earthquakes as Detected by the GRACE Satellites: A Reexamination. Geophys. J. Int., 183, 733–747 doi: 10.1111/j.1365-246X.2010.04756.x.

Feng, L., Hill, E.M., Banerjee, P., Hermawan, I., Tsang, L.L.H., Natawidjaja, D.H., Suwargadi, B.W., and Sieh, K., 2015. A unified GPS-based earthquake catalog for the Sumatran plate boundary between 2002 and 2013. J. Geophys. Res., 120, 3566-3598, doi:10.1002/2014JB011661.

Fukahata, Y., and Matsu'ura, M., 2005. General expressions for internal deformation fields due to a dislocation source in a multilayered elastic half-space. Geophys. J. Int., 161, 507–521, doi: 10.1111/j.1365-246X.2005.02594.x.

Fukahata, Y., and Matsu'ura, M., 2006. Quasi-static internal deformation due to a dislocation source in a multilayered elastic/viscoelastic half-space and an equivalence theorem. Geophys. J. Int., 166, 418–434, doi: 10.1111/j.1365-246X.2006.02921.x.

Fukao, Y., Obayashi, M., Nakakuki, T., et al., 2009. Stagnant Slab: A Review Annu. Rev. Earth Planet. Sci., 37, 10.1–10.28, doi: 0.1146/annurev.earth.36.031207. 124224.

Gunawan, E., 2014. Comprehensive postseismic deformation model of the 2004 Sumatra-Andaman earthquake constrained by GPS data in northern Sumatra. A dissertation for the degree of Doctor of Science Department of Earth and Environmental Sciences, Graduate School of Environmental Studies, Nagoya University.

Habermann, R.E., 1991.Seismicity rate variations and systematic changes in magnitudes in teleseismic catalogs. Tectonophysics, 193, 4, 277-289, doi: 10.1016/0040-1951(91)90337-R.

Hafkenscheid, E., Buiter, S.J.H., Wortel, M.J.R., Spakman, W., and Bijwaard, H., 2001. Modelling the seismic velocity structure beneath Indonesia: a comparison with tomography. Tectonophysics 333, 35-46

Hamilton W., 1988. Plate tectonics and island arcs, Geol. Soc. Am. Bull., 100, 1503–1527.

Han, S.C., Sauber, J., Luthcke, S. B., Ji, C., and Pollitz, F. F., 2008. Implications of postseismic gravity change following the great 2004 Sumatra-Andaman earthquake from the regional harmonic analysis of GRACE intersatellite tracking data. J. Geophys. Res., 113, B11413.

Hanifa, N.R., Sagiya, T., Kimata, F., Efendi, J., Abidin, H.Z., and Meilano, I., 2014. Interplate coupling model off the southwestern coast of Java, Indonesia, based on continuous GPS data in 2008-2010. Earth Planet. Sci. Lett. 401, 159-171, doi: 10.1016/j.epsl.2014.06.010.

1815 Haridhi, H.A., Huang, B.S., Wen, K.L., Denzema, D., Prasetyo, R.A., and Lee, C.S.,
1816 2018. A study of large earthquake sequences in the Sumatra subduction zone
1817 and its possible implications. Terr. Atmos. Ocean. Sci., 29(6), 635-652, doi:
1818 10.3319/TAO.2018.08.22.01.
1819 Heki, K., and Mitsui, Y., 2013. Accelerated pacific plate subduction following
1820 interplate thrust earthquakes at the Japan trench. Earth Planet. Sci. Lett., 363,
1821 44–49, doi: 10.1016/j.epsl.2012.12.031.
1822 Heki, K., Miyazaki, S. and Tsuji, H., 1997. Silent fault slip following an interplate
1823 thrust earthquake at the Japan Trench. Nature, 386, 595-597.
1824 Herring, T. A., King, R. W., Floyd, M. A., and McClusky S. C., 2018. Introduction
1825 to GAMIT/GLOBK, Release 10.7. geoweb.mit.edu/gg/intro_GG.pdf.
1826 Heuret, A., Conrad, C. P., Funiciello, F., Lallemand, S., and Sandri, L., 2012.
1827 Relation between subduction megathrust earthquakes, trench sediment
1828 thickness and upper plate strain. Geophys. Res. Lett. 39, L05304,
1829 doi:10.1029/2011GL050712.
1830 Hoffmann, F., Metzger, S., Moreno, M., Deng, Z., Sippl, C., Ortega-Culaciati, F.,
1831 and Oncken, O., 2018. Characterizing afterslip and ground displacement rate
1832 increase following the 2014 Iquique Pisagua M_w 8.1 earthquake, Northern
1833 Chile. J. Geophys. Res. Solid Earth, 123, 4171–4192, doi:
1834 org/10.1002/2017JB014970.
1835 Husker. A., and Davis, P.M., 2009. Tomography and thermal state of the Cocos plate
1836 subduction beneath Mexico City. J. Geophys. Res. 114, B04306,
1837 doi:1029/2008JB006039
1838 Ide, S., 2013. The proportionality between relative plate velocity and seismicity in
1839 subduction zones. Nature Geosci. 6, 780-785, doi: 10.1038/NGEO1901.
1840 Itoh, Y., and Nishimura, T., 2016. Characteristics of postseismic deformation
1841 following the 2003 Tokachi-oki earthquake and estimation of the viscoelastic
1842 structure in Hokkaido, northern Japan. Earth, Planets Space 68, 156, doi:
1843 10.1186/s40623-016-0533-y.
1844 Jónsson, S., Segall, P., Pedersen, R., and Björnsson, G., 2003. Post-earthquake
1845 ground movements correlated to pore-pressure transients. Nature, 434, 179-183.
1846 Kanamori, H., 1978. Quantification of earthquakes, Nature, 271, 411-414.
1847 Kanamori, H., Jennings, P.C., Singh, S.K., and Astiz, L., 1993. Estimation of strong
1848 ground motion in Mexico City expected for large earthquakes in the Guerrero
1849 Seismic Gap. Bull. Seismol. Soc. Am. 83(3), 811-829.
1850 Kelleher, J. A., 1972. Rupture zones of large South American earthquakes and some
1851 predictions. J. Geophys. Res. 77(11), 2087–2103.
1852 King, G. C. P., Stein, R.S., and Lin, J., 1994. Static stress changes and the triggering
1853 of earthquakes, Bull. Seismol. Soc. Am., 84, 935-953.
1854 Kiser, E., and Ishii, M., 2012. The March 11, 2011 Tohoku-oki earthquake and
1855 cascading failure of the plate interface. Geophys. Res. Lett., 39, L00G25,
1856 doi:10.1029/2012GL051170.
1857 Klein, E., Fleitout,L., Vigny, C., and Garaud, J.D., 2016. Afterslip and viscoelastic
1858 relaxation model inferred from the large-scale post-seismic deformation
1859 following the 2010 M_w 8.8 Maule earthquake (Chile). Geophys. J. Int., 205,
1860 1455–1472, doi: 10.1093/gji/ggw086.
1861 Kodaira, S., Nakamura, Y., Yamamoto, Y., Obana, K., Fujie, G., No, T., Kaiho, Y.,
1862 Sato, T., and Miura, S., 2017. Depth-varying structural characters in the rupture

zone of the 2011 Tohoku-oki earthquake. Geosphere; 13, 5, doi:10.1130/GES01489.1.

Larsen, S., Reilinger, R., Neugebauer, H., and Strange, W., 1992. Global Positioning System measurements of deformation associated with the 1987 Superstition Hills earthquake: evidence for conjugate faulting. J. Geophys. Res., 97, B4, 4885-4902.

Li, S., Moreno, M., Bedford, J., Rosenau, M., and Oncken, O., 2015. Revisiting viscoelastic effects on interseismic deformation and locking degree: A case study of the Peru-North Chile subduction zone. J. Geophys. Res. 120, 4522–4538, doi:10.1002/2015JB011903.

Lisowski, M., Prescott, W.H., Savage, J.C., and Johnston, M.J., 1990. Geodetic estimate of coseismic slip during the 1989 Loma Prieta, California, earthquake. Geophys. Res. Lett., 17(9) 1437-1440.

Lombardi, A.M., Cocco, M., and Marzocchi, W., 2010. On the increase of background seismicity rate during the 1997-1998 Umbria-Marche, central Italy, sequence: Apparent variation or fluid-driven triggering?. Bull. Seismol. Soc. Am., 100, 3, 1138-1152, doi:10.1785/0120090077.

Loveless, J.P., 2017. Super-interseismic periods: Redifining earthquake recurrence. Geophys. Res. Lett., 44, doi: 10.1002/2017GL072525.

Lubis, A.M., Hashima, A., and Sato, T., 2012. Analysis of afterslip distribution following the 2007 September 12 southern Sumatra earthquake using poroelastic and viscoelastic media. Geophys. J. Int., doi: 10.1093/gji/ggs020.

Manea, V.C., Manea, M., and Ferrari, L., 2013. Geodynamical perspective on the subduction of Cocos and Rivera plates beneath Mexico and Central America. Tectonophysics, doi: 10.1016/j.tecto.2012.12.039.

Marsan, D., and Enescu, B., 2012. Modeling the foreshock sequence prior to the 2011, MW9.0 Tohoku, Japan, earthquake. J. Geophys. Res., 117, B06316, doi:10.1029/2011JB009039.

Materna, K., Bartlow, N., Wech, A., Williams, C., and Burgmann, R., 2019. Dynamically Triggered Changes of Plate Interface Coupling in Southern Cascadia. Geophys. Res. Lett. 46, 12890-12899, doi:10.1029/2019GL084395.

Mavrommatis, A., Segall, P., and Johnson, K.M., 2014. A decadal-scale deformation transient prior to the 2011 Mw 9.0 Tohoku-oki earthquake. Geophys. Res. Lett., 41, 4486–4494, doi:10.1002/2014GL060139.

Melnick, D., Moreno, M., Quinteros, J., Baez, J.C., Deng, Z., Li, S., and Oncken, O., 2017. The super-interseismic phase of the megathrust earthquake cycle in Chile. Geophys. Res. Lett., 44, doi:10.1002/2016GL071845.

Metois, M., Socquet, A., Vigny, C., Carrizo, D., Peyrat, S., Delorme, A., Maureira, E., Valderas-Bermejo M.-C., and Ortega I., 2013. Revisiting the North Chile seismic gap segmentation using GPS-derived interseismic coupling. Geophys. J. Int. doi: 10.1093/gji/ggt183.

Mignan, A., King, G., Bowman, D., Lacassin, R., and Dmowska, R., 2006. Seismic activity in the Sumatra-Java region prior to the December 26, 2004. (Mw=9.0-9.3) and March 28, 2005 (Mw=8.7) earthquake. Earth Planet. Sci. Lett. 244, 639-654, doi: 10.1016/j.epsl.2006.01.058.

Miyazaki, S., Segall, P., Fukuda, J., and Kato T., 2004. Space time distribution of afterslip following the 2003 Tokachi-oki earthquake: Implications for

variations in fault zone frictional properties. Geophys. Res. Lett., 31, L06623, doi:10.1029/2003GL019410.
Moreno, M., Melnick, D., Rosenau, M., Bolte, J., Klotz, J., Echtler, H., Baez, J., Bataille, K., Chen, J., Bevis, M., Hase, H., and Oncken, O., 2011. Heterogeneous plate locking in the South–Central Chile subduction zone: building up the next great earthquake. *Earth Planet. Sci. Lett*. 305, 413–424. doi: 10.1016/j.epsl.2011.03.025.
Moreno, M., Melnick, D., Rosenau, M., Baez, J., Klotz, J., Oncken, O., Tassara, A., Chen, J., Bataille, K., Bevis, M., Socquet, A., Bolte, J., Vigny, C., Brooks, B., Ryder, I., Grund, V., Smalley, B., Carrizo, D., Bartsch, M., Hase, H., 2012. Toward understanding tectonic control on the Mw 8.8 2010 Maule Chile earthquake. Earth Planet. Sci. Lett. 321-322, 152-165, doi: 10.1016/j.espl.2012.01.006.
Muller, R. D., Sdrolias, M., Gaina, C., and Roest, W. R., 2008. Age, spreading rates, and spreading asymmetry of the world's ocean crust. Geochemistry, Geophysics, Geosystems, 9, Q04006., doi: 10.1029/2007GC001743.
Müller, R.D., Roest, W.R., Royer, J.Y., Gahagan, L.M., and Sclater, J.G., 1997. Digital isochrons of the worlds ocean floor. J. geophys. Res., 102, B2, 3211-3214. doi: 10.1029/96JB01781.
Nakagawa, H., Toyofuku, T., Kotani, K., Miyahara, B., Iwashita, C., Kawamoto, S., Hatanaka, Y., Munekane, H., Ishimoto, M., Yutsudo, T., Ishikura, N., Sugawara, Y., 2009. Development and validation of GEONET new analysis strategy (Version 4). J. Geogr. Surv. Inst. 118, 1−8, in Japanese.
Natawidjaja, D. H., Sieh, K., Chlieh, M., Galetzka, J., Suwargadi, B.W., Cheng, H., Edwards, R. L., Avouac, J‐P., and Ward, S. N., 2006. Source parameters of the great Sumatran megathrust earthquakes of 1797 and 1833 inferred from coral microatolls, J. Geophys. Res. 111, B06403, doi:10.1029/2005JB004025.
Niitsuma, N., 2004. Japan Trench and tectonics of the Japanese Island Arcs. The Island Arc 13, 306–317.
Nur, A., Mavko, G., 1974. Postseismic viscoelastic rebound. *Science* 183, 204–206.
Ogata, Y., 1988. Statistical Models for Earthquake Occurrences and Residual Analysis for Point Processes. Journal of the American Statistical Association, 83, 401. (Mar., 1988), pp. 9-27
Ozawa, S., Kaidzu, M., Murakami, M., Imakiire, T., Hanataka, Y., 2004. Coseismic and postseismic crustal deformation after the Mw 8 Tokachi-oki earthquake in Japan. Earth Planet Space, 56, 675-680.
Panet, I., Pollitz, F., Mikhailov, V., Diament, M., Banerjee, P., and Grijalva, K., 2010. Upper mantle rheology from GRACE and GPS postseismic deformation after the 2004 Sumatra–Andaman earthquake. Geochemical, Geophysics. Geosystem. Vol 11, doi:10.1029/2009GC002905.
Peltzer, G., P. Rosen, F. Rogez, dan K. Hudnut., (1998): Poroelastic rebound along the Landers 1992 earthquake surface rupture. Journal of Geophysics Research., 103 (B12), 30131-30146.
Peng, Y., Zhou, S., Zhuang, J., and Shi, J., 2012. An approach to detect the abnormal seismicity increase in Southwestern China triggered co-seismically by 2004 Sumatra M_w 9.2 earthquake. Geophys. J. Int., 189, 1734–1740, doi: 10.1111/j.1365-246X.2012.05456.x.
Perfettini, H., Avouac, J.-P., Ruegg, J.C., 2005. Geodetic displacements and

aftershocks following the 2001 Mw=8.4 Peru earthquake: Implications for the mechanics of the earthquake cycle along subduction zones. J. Geophys. Res. 110, B09404, doi:10.1029/2004JB003522.

Pesicek, J.D., Engdahl,E. R., Thurber, C. H., DeShon, H. R., and Lange D., 2012. Mantle subducting slab structure in the region of the 2010 M8.8 Maule earthquake (30–40◦S), Chile. Geophys. J. Int., doi: 10.1111/j.1365-246X.2012.05624.x.

Pollitz, F. F., Bürgmann, R., and Banerjee, P., 2006. Post-seismic relaxation following the great 2004 Sumatra-Andaman earthquake on a compressible self-gravitating Earth. Geophys. J. Int., 167(1), 397-420.

Prawirodirdjo, L., Bock, Y., McCaffrey, R., Genrich, J., Calais, E., Stevens, C., Puntodewo, S.S.O., Subarya, C., Rais, J., Zwick, P., and Fauzi., 1997. Geodetic observations of interseismic strain segmentation at the Sumatra subduction zone. Geophys. Res. Lett., 24, 21, 2601-2604.

Prawirodirdjo, L., Bock, Y., Genrich, J. F., Puntodewo, S. S. O., Rais, J., Subarya, C., and Sutisna, S., 2000. One century of tectonic deformation along the Sumatran fault from triangulation and Global Positioning System surveys, J. Geophys. Res., 105(28), 28, 343–28,361, doi:10.1029/ 2000JB900150.

Pritchard, M.E., Simons, M., Rosen P. A., Hensley, S., and Webb, F. H., 2002. Co-seismic slip from the 1995 July 30 Mw = 8.1 Antofagasta, Chile, earthquake as constrained by InSAR and GPS observations. Geophys. J. Int. 150, 362–376, doi: 10.1046/j.1365-246X.2002.01661.x.

Ritsema, J., Lay, T., and Kanamori, H., 2012. The 2011 Tohoku Earthquake. Elements, 8, 183–188, doi: 10.2113/gselements.8.3.183.

Ruff, L., and Kanamori, H., 1980. Seismicity and the subduction process. Phys. Earth Planet. Inter. 23, 240–252.

Ryder, I., 2006. Elastic and Viscoelastic Modelling of Postseismic Motion and Fault Structures. Doctoral Thesis. *Departement of Earth Sciences, University of Oxford.*

Sagiya, T., 2004. A decade of GEONET: 1994-2003 –The continuous GPS observation in Japan and its impact on earthquake studies–. Earth Planet and Space, 56, xxix-xli.

Satake, K., Nishimura, Y., Putra, S.P., Gusman, A. R., Sunendar, H., Fujii, Y., Tanioka, Y., Latief, H., and Yulianto, E., 2012. Tsunami source of the 2010 Mentawai, Indonesia earthquake inferred from tsunami field survey and waveform modeling. PAGEOPH 170, 1567-1582.

Sato, M., Ishikawa, T., Ujihara, N., Yoshida, S., Fujita, M., Mochizuki, M. and Asada, A., 2011. Displacement above the hypocenter of the 2011 Tohoku-oki earthquake, Science, 332, 1395.

Segou, M. And Parsons, M., 2018. Testing earthquake links in Mexico from 1978 to the 2017 M = 8.1 Chiapas and M = 7.1 Puebla shocks. Geophys. Res. Lett., 45, 708–714, doi: 10.1002/2017GL076237.

Savage, J.C., Lisowski, M., Svarc, J.L., 1994. Postseismic deformation following the 1989 (M = 7.1) Loma Prieta, California, earthquake. J. Geophys. Res., 99, B7, 13757-17765.

Savage, J.C., and Svarc, J.L., 1997. Postseismic deformation associated with the 1992 Mω = 7.3 Landers earthquake, southern California. J. Geophys. Res., 102, B4, 7565-7577.

Schurr, B., Asch, G., Rosenau, M., Wang, R., Oncken, O., Barrientos, S., Salazar, P., and Vilotte, J. P., 2012. The 2007 M7.7 Tocopilla northern Chile earthquake sequence: Implications for along-strike and downdip rupture segmentation and megathrust frictional behavior. J. Geophys. Res. 117, B05305, doi:10.1029/2011JB009030.

Scire. A., Zandt, G., Beck, S., Long, M., and Wagner, L., 2017. The deforming Nazca slab in the mantle transition zone and lower mantle: Constraints from teleseismic tomography on the deeply subducted slab between 6°S and 32°S. Geosphere, 13, 3, 665-680, doi:10.1130/GES01436.1.

Schubert, G., Turcotte, D. L., Olson, P., 2001. Mantle Convection in the Earth and Planets. Cambridge University Press.

Shao, Z., Zhan, W., Zhang, L., and Xu, J., 2016. Analysis of the far field Co-seismic and Post-seismic responses caused by the 2011 Mw 9.0 Tohoku-Oki earthquake. Pure Appl. Geophys., 173, 411-424, doi: 10.1007/s00024-015-1131-9.

Shen, Z. K., Jackson, D.D., Feng, Y., Cline, M., Kim, M., Fang, P., and Bock, Y., 1994. Postseismic deformation following the Landers earthquake, California, 28 June 1992. Bull. Seismol. Soc. Am., 84, 3, 780-791.

Shinohara, M., et al.,2012. Precise aftershock distribution of the 2011 off the Pacific coast of Tohoku Earthquake revealed by an ocean-bottom seismometer network. Earth Planets Space, 64, 1137–1148, doi:10.5047/eps.2012.09.003.

Simons, W. J. F. et al., 2007. A decade of GPS in Southeast Asia: Resolving Sundaland motion and boundaries. J. Geophys. Res. 112, B06420, doi:10.1029/2005JB003868.

Singh, S. K., Comte, D., and Pardo, M. 1992. Background seismicity and strength of coupling in the subduction zones. Bull. Seismol. Soc. Am. 82, 2114–2125.

Stern, R. J., 2002. Subduction zones. Rev. Geophys., 40(4), 1012, doi:10.1029/2001RG000108.

Suito, H., and Freymueller, J. T., 2009. A viscoelastic and afterslip postseismic deformation model for the 1964 Alaska earthquake. J. Geophys. Res.,Vol 114, B11404, doi:10.1029/2008JB005954.

Sun, T., Wang, K., Iinuma, T., Hino, R., He, J., Fujimoto, H., Kido., M., Osada, Y., Miura, S., Ohta, Y., and Hu, Y., 2014. Prevalence of viscoelastic relaxation after the 2011 Tohoku-oki earthquake. Nature, 514, doi:10.1038/nature13778.

Susilohadi, S., Gaedicke, C., and Djajadihardja, Y., 2009. Structures and sedimentary deposition in the Sunda Strait, Indonesia. Tectonophys, 467(1), 55-71., doi: 10.1016/j.tecto.2008.12.015.

Tajima, F., Mori, J., and Kennet, B.L.N., 2013. A review of the 2011 Tohoku-oki earthquake (Mw 9.0): Large-scale rupture across heterogeneous plate coupling. Tectonophysics 586, 15-34, doi: 10.1016/j.tecto.2012.09.014.

Takahashi, H., and Kasahara, M., 2004. The 2003 Tokachi-oki earthquake, off Southeastern Hokkaido, Japan. Journal of the Seismological Society of Japan, 57, 2, 115-130, doi: 10.4294/zisin1948.57.2_115.

Takano, T., 2011. Overview of the 2011 East Japan Earthquake and Tsunami Disaster. The 2011 East Japan Earthquake Bulletin of the Tohoku Geographical Association.

Tanioka, Y., et al., 2004. Tsunami run-up heights of the 2003 Tokachi-oki earthquake. Earth Planets Space, 56, 359–365.

Tanioka, Y. and Katsumata, K., 2007. Tsunami generated by the 2004 Kushiro-oki earthquake. Earth Planets Space, 59, e1-e3.

Thatcher, W., and Rundle, J. B., 1984. A viscoelastic coupling model for the cyclic deformation due to periodically repeated earthquakes at subduction zones. J. Geophys. Res., 89, 7631–7640.

Tsuji, H., Hatanaka, Y., Sagiya, T. And Hashimoto, M., 1995. Coseismic crustal deformation from the 1994 Hokkaido-Toho-Oki earthquake monitored by a nationwide continuous GPS arary in Japan. Geophys. Res. Lett., 22, 1669-1672.

Uchida, N., and Matsuzawa, T., 2013. Pre- and postseismic slow slip surrounding the 2011 Tohoku-oki earthquake rupture. Earth and Planetary Science Letters, 374, 81–91, doi: 10.1016/j.epsl.2013.05.021.

Uchida, N., Asano, Y., and Hasegawa, A., 2016. Acceleration of regional plate subduction beneath Kanto, Japan, after the 2011 Tohoku-oki earthquake. Geophys. Res. Lett., 43, 9002–9008, doi:10.1002/2016GL070298.

Uyeda, S., 1982. Subduction zones: An introduction to comparative subductology. Tectonophys., 81, 133-159.

Uyeda, S., and Kanamori, H., 1979. Back-arc opening and the mode of subduction. J. Geophys. Res. 84, 1049–1061.

Vigny, C., et al., 2011. The 2010 Mw 8.8 Maule megathrust earthquake of Central Chile, monitored by GPS. Science 332, 1417-1421, doi:10.1126/ science.1204132.

Villegas-Lanza, J. C., Chlieh M., Cavalié O., Tavera H., Baby P., Chire-Chira J., and Nocquet J.-M., 2016. Active tectonics of Peru: Heterogeneous interseismic coupling along the Nazca megathrust, rigid motion of the Peruvian Sliver, and Subandean shortening accommodation. J. Geophys. Res., 121, 7371–7394, doi:10.1002/2016JB013080.

Wang, K., 2007. In the Seismogenic Zone of Subduction Thrust Faults (eds Dixon, T. H. & Moore, J. C.) 540–574. *Columbia University Press*.

Wang, K., Y. Hu, and J. He (2012), Deformation cycles of subduction earthquakes in a viscoelastic Earth, Nature. 484, 327-332, doi:10.1038/nature11032.

Wiemer, S. and Wyss, M., 2000. Minimum Magnitude of Completeness in Earthquake Catalogs: Examples from Alaska, the Western United States, and Japan. Bull. Seismol. Soc. Am., 90, 4, 859–869.

Yamagiwa, S., Miyazaki, S., Hirahara, K., and Fukahata, Y., 2015. Afterslip and viscoelastic relaxation following the 2011 Tohoku-oki earthquake (M_w9.0) inferred from inland GPS and seafloor GPS Acoustic data. Geophys. Res. Lett., 42, 66–73, doi:10.1002/2014GL061735.

Yáñez G., Ranero C.R., and Díaz J., 2001. Magnetic Anomaly interpretation across the southern central Andes (32°–34°S): The role of the Juan Fernández Ridge in the late Tertiary evolution of the margin. J. Geophys. Res., 106, 6325-6345.

Zhuang, J. O Ogata, Y., and Vere-Jones, D., 2004. Analyzing earthquake clustering features by using stochastic reconstruction. J. Geophys. Res., 109, B05301. doi:10.1029/2003JB002879.